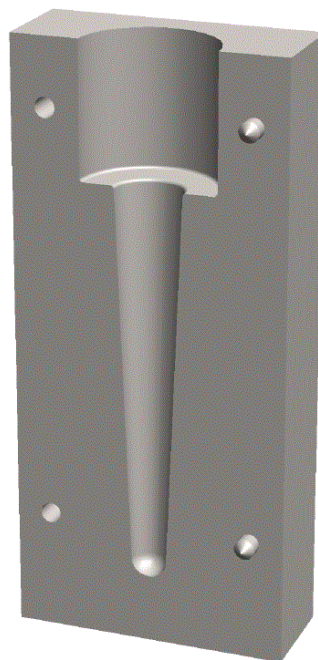


Annbjørg Horgar

# Comparative Study of Mechanical Properties and Microstructure of Components Made by Casting and Wire + Arc Additive Manufacturing of Eutectic Al-12Si Alloy

Master's thesis in Master of Science in Mechanical Engineering  
Supervisor: Odd Magne Akselsen, Geir Langelandsvik  
December 2018



Permanent Mold



Annbjørg Horgar

# **Comparative Study of Mechanical Properties and Microstructure of Components Made by Casting and Wire + Arc Additive Manufacturing of Eutectic Al-12Si Alloy**

Master's thesis in Master of Science in Mechanical Engineering  
Supervisor: Odd Magne Akselsen, Geir Langelandsvik  
December 2018

Norwegian University of Science and Technology  
Faculty of Engineering  
Department of Mechanical and Industrial Engineering



# Abstract

The Master's thesis study evaluates the relationship between the wire and arc additive manufacturing (WAAM) and the casting process for the aluminum-silicon alloys with silicon (Si) content of 12% (Al-12Si). The WAAM deposits layer-by-layer three-dimensional products defined by computer aided design and is profitable for small-series production. By December 2018, there is little literature on WAAM technology, especially regarding to the cooling rate. The aluminum casting technology can fill the gap and help the development of WAAM.

In this study, Al-12Si samples produced by WAAM and casting are compared by their mechanical and microstructural properties. The WAAM sample is of the Aluminum Association (AA) 4047 and was sliced into specimens. For the casting samples, the melted alloy Al-12Si was added strontium and casted into a permanent steel mold and into three sand molds. The permanent steel mold could be reused for serial casting while the sand molds were for one-time casting only. The molds are awl-shaped to correspond to a common weld bead and to obtain a spectrum of cooling rates.

Two fracture mechanisms are observed in the fracture surface of a permanent mold cast tensile specimen after completed the tensile test. The first are the brittle (Si) particles and the second the gas and shrinkage pores. Al-12Si is ductile and fractures when stress concentration takes place in the sharp-edged (Si) particles or pores and grows to intergranular fracture. The observed dendrite traces indicate inclusions between the dendrite lobes.

The secondary dendrite arm spacing (SDAS) are measured for the specimens and then used in calculating the cooling rates. The results are rounded to  $6\ \mu\text{m}$  in the space and  $620\ \text{Ks}^{-1}$  in the rate for the WAAM specimens,  $11\ \mu\text{m}$  and  $100\ \text{Ks}^{-1}$  for the permanent mold castings and  $21\ \mu\text{m}$  and  $15\ \text{Ks}^{-1}$  for the sand mold castings.

For the WAAM, the SDAS are larger in the partially melted zone than in the fusion zone. The dendrites in the heat-affected zone are small and entangled. A potential relationship with respect to the SDAS is found between the fusion zone in the WAAM sample and the middle of the permanent mold castings. The comparison of the mechanical properties can be interpreted as the increased cooling rate in the Al-12Si samples, then higher strength, larger elongation and higher hardness. A permanent mold with even smaller awl diameter might allow achieving SDAS and cooling rates closer to the WAAM sample.

Further study should be carried out to analyze the phases around the precipitated (Si) particles and the dendrites and to map the component elements properties of the WAAM sample and the casting samples.



# Sammendrag

Masteroppgaven vurderer sammenhengen mellom additiv tilvirkning ved lysbuesveising med trådmater (eng. *Wire and Arc Additive Manufacturing*, fork. WAAM) og støping av aluminium leget med silisiuminnhold (Si) på 12% (Al-12Si). WAAM er en teknikk for å sveise lagvis tredimensjonale produkter designet i dataassistert konstruksjon (eng. computer-aided design, fork. CAD), og er lønnsom for småserieproduksjon. Det er per desember 2018 lite litteratur om WAAM-teknologi, særlig kjølehastigheten. Støpeteknologien for aluminium kan fylle tomrommet og akselerere utviklingen av WAAM.

Denne studien sammenligner arbeidsstykker i Al-12Si-legering tilvirket ved WAAM og støping, med hensyn til deres mekaniske og mikrostrukturelle egenskaper. WAAM-arbeidsstykket er av legeringen *Aluminium Association* (AA) 4047 og ble skåret inn i mindre prøver. Støpestykkene er av legeringen Al-12Si med tilsatt strontium og ble støpt i en permanent stålform og i tre sandformer. Permanentformen kan gjenbrukes for flere støpninger, mens sandformene kan brukes kun én gang. Støpeformen er sylformet for å tilsvare en typisk sveisestreng og for å oppnå et spektrum av kjølehastigheter.

To bruddmekanismer er observert i bruddflaten på en permanentstøpt strekkprøve etter gjennomført strekktest. Den ene er sprøe (Si) partikler og den andre gass- og krympeporer. Al-12Si-legeringen er duktil og bryter når spenningskonsentrasjonen finner sted ved de skarpe partiklene eller porene, og vokser til intergranulære brudd. De observerte dendrittsporene indikerer inneslutninger mellom dendrittarmene.

Sekundær dendrittarmsavstand (SDAS) måles for prøvene og brukes deretter i beregning av kjølehastighetene. Resultatene er avrundet til 6  $\mu\text{m}$  i avstanden og 620  $\text{Ks}^{-1}$  i hastigheten for WAAM-prøvene, 11  $\mu\text{m}$  og 100  $\text{Ks}^{-1}$  for permanentstøpningene og 21  $\mu\text{m}$  og 15  $\text{Ks}^{-1}$  for sandstøpningene.

SDAS for WAAM er større i delvis smeltet-sonen enn i smeltesonen. Dendrittene i varmepåvirket-sonen er små og sammenklemt. En mulig sammenheng i SDAS-målingene er funnet for smeltesonen i WAAM-prøven og for midtdelen av permanentstøpningen. Sammenligningen av de mekaniske egenskapene for Al-12Si-prøvene kan tolkes dithen at jo større kjølehastighet, desto høyere styrke, større forlengelse og høyere hardhet. En permanentform med enda mindre diameter kan oppnå SDAS og kjølehastigheter tilsvarende de for WAAM-prøven.

Ytterlig arbeid bør utføres for å analysere fasene rundt de utfelte (Si)-partiklene og dendrittene, og for å kartlegge komponentelementegenskapene til WAAM-prøven og støpningene.





# Preface

This master's thesis is written at the Norwegian University of Science and Technology (NTNU), Faculty of Engineering, Department of Mechanical and Industrial Engineering (MTP) localized in Trondheim City, Norway. This report presents results from a research project in collaboration with NTNU and SINTEF Industry AS and is a feasibility study regarding combining the wire and arc additive manufacturing technology (WAAM) for the aluminum-silicon alloys with a silicon content of 12% (Al-12Si).

I am a Master's student admitted by the master's degree programme Mechanical Engineering at NTNU, MTP, and the Author of the project report. The specialization chosen is Product Development and Materials Engineering and the corresponding course for the thesis is "TMM4960 - Engineering Design and Materials, Master's Thesis".

The supervisors of the project are Odd Magne Akselsen and Geir Langelandsvik. Odd Magne Akselsen works as senior research scientist at SINTEF Industry AS and as adjunct professor at NTNU, MTP. Geir Langelandsvik works as PhD. fellow by SINTEF Industry AS.

Trondheim, December 20<sup>th</sup>, 2018

Annbjørg Horgar



# Acknowledgments

This work was supported by SINTEF Industry and NTNU, department MTP. I would like to thank professor Odd Magne Akselsen and PhD. fellow Geir Langelandsvik for their guidance and consultation in the project work, for the good collaboration and for letting me partake in their work.

I also wish to thank research director Morten Onsøyen, senior researcher Arne Nordmark and technician Kurt Sandaunet for their knowledge and guidance during the casting and thanks to professor Afrooz Barnoush for his consultation in fracture mechanisms.

Finally, thanks to executive officer Andrea Steinert for practical information related to the master's thesis.



# Table of Contents

LIST OF FIGURES .....	XIV
LIST OF TABLES .....	XV
ABBREVIATION .....	XVI
SYMBOLS .....	XVI
<b>1 PROJECT DESCRIPTION .....</b>	<b>19</b>
1.1 BACKGROUND .....	19
1.2 STRUCTURE OF THE PROJECT REPORT .....	20
<b>2 LITERATURE .....</b>	<b>21</b>
2.1 WIRE AND ARC ADDITIVE MANUFACTURING (WAAM) .....	21
2.2 ALUMINUM-SILICON ALLOY (AL-12Si) .....	22
2.3 SECONDARY DENDRITE ARM SPACING (SDAS) .....	23
2.4 COOLING RATES .....	25
2.5 CASTING .....	26
<b>3 MATERIALS, TESTING AND CHARACTERIZATION .....</b>	<b>29</b>
3.1 INTRODUCTION .....	29
3.2 MATERIALS .....	29
3.3 SAMPLE PREPARATION .....	29
3.4 TEST METHODS .....	37
3.5 MICROSTRUCTURAL ANALYSIS .....	39
<b>4 RESULTS .....</b>	<b>41</b>
4.1 MECHANICAL PROPERTIES .....	41
4.2 MICROSTRUCTURAL PROPERTIES .....	45
<b>5 DISCUSSION .....</b>	<b>53</b>
5.1 FRACTURE MECHANISMS .....	53
5.2 POROSITY LEVELS .....	55
5.3 MICROHARDNESS .....	56
5.4 SECONDARY DENDRITE ARM SPACING (SDAS) AND COOLING RATE .....	57
5.5 RELATIONSHIP IN THE RESULTS .....	64
<b>6 CONCLUSION .....</b>	<b>67</b>
<b>7 REFERENCES .....</b>	<b>69</b>
<b>APPENDIX .....</b>	<b>71</b>

# List of Figures

Figure 2.1: Cost analysis for a real-world case produced by the WAAM and the casting process [3].....	22
Figure 2.2: Phase diagram Al-Si [4].....	23
Figure 2.3: Dendrites in steel (SEM, 15x) [6].....	24
Figure 2.4: Interdendritic shrinkage. ....	24
Figure 2.5: Schematic representation of five SDAS measurement methods [5]. ....	25
Figure 2.6: Measuring the length L, edge-to-edge [7].....	26
Figure 2.7: Wedge casting sample.....	26
Figure 3.1: Durville casting process. ....	30
Figure 3.2: Casting identities. ....	30
Figure 3.3: Permanent mold drawing dimensions and 3D-model .....	31
Figure 3.4: Permanent mold coated with anti-sticking film.....	31
Figure 3.5: Temperature log for casting AL-12Si in permanent mold. Sample P1 to P5 were rejected due to uneven casting start temperature.....	32
Figure 3.6: Forming the sand mold, with impression of a permanent mold casting.....	33
Figure 3.7: Part deposited by WAAM.....	34
Figure 3.8: Weld beads from the front view .....	34
Figure 3.9: WAAM specimen identities in approximate positions. ....	35
Figure 3.10: Dimensions of the circular tensile test specimen by WAAM .....	37
Figure 3.11: Dimensions of the circular tensile test specimen by casting process.....	37
Figure 3.12: Diamond Pyramid Hardness [10].....	38
Figure 3.13: Pore analysis in ImageJ, with threshold. Red circles are counted as metallurgical gas porosity.....	39
Figure 3.14: Measuring secondary dendrite arm spacing (SDAS).....	40
Figure 4.1: Average 0.2% offset yield strengths and ultima tensile strengths,.....	41
Figure 4.2: Elongations at break, .....	41
Figure 4.3: Average elastic moduli .....	42
Figure 4.4: Stress-strain curves for the tensile test specimens .....	42
Figure 4.5: Fracture surfaces of the permanent mold cast tensile specimens P11 (left) and P8 (right). ....	43
Figure 4.6: Fractographies of the permanent mold cast tensile specimens. ....	44
Figure 4.7: Microhardness results.....	45
Figure 4.8: Pore analysis results. ....	46
Figure 4.9: Solidification shrinkage in permanent mold casting P14 (SEM, 100 $\mu\text{m}$ ) .....	46
Figure 4.10: Pores and solidification shrinkage in sand mold casting S3 (SEM, 100 $\mu\text{m}$ ).....	46
Figure 4.11: SDAS for the WAAM specimen M calculated with equation (1).....	47
Figure 4.12: SDAS for the WAAM specimen M calculated with equation (2).....	47
Figure 4.13: Dendrite formation in the WAAM specimen M (LOM, 50 $\mu\text{m}$ ) .....	48
Figure 4.14: Eutectic microconstituent in the WAAM sample (SEM, 10 $\mu\text{m}$ ).....	48
Figure 4.15: EBSD images.....	49
Figure 4.16: SDAS for permanent mold casting P13 and sand mold casting S2 calculated with equation (1). ....	50
Figure 4.17: SDAS for permanent mold casting P13 and sand mold casting S2 calculated with equation (2). ....	50
Figure 4.18: Microstructures in permanent mold casting P13 .....	51
Figure 4.19: Microstructures in sand mold casting S2 .....	52
Figure 5.1: Cleavage fracture in permanent mold casting P8.....	53

Figure 5.2: Intergranular fractures in permanent mold casting P11 (SEM, 100 $\mu\text{m}$ ). ....	54
Figure 5.3: Dimples (lower arrow) and intergranular fractures (upper arrow) in permanent mold casting P11 (SEM, 2 $\mu\text{m}$ ).....	54
Figure 5.4: Dendritic traces in permanent mold casting P11 (SEM, 20 $\mu\text{m}$ ) .....	54
Figure 5.5: (Si) particles and pores in permanent mold casting P11.....	55
Figure 5.6: (Si) particles in the permanent mold castings A) P13 and B) P14 .....	55
Figure 5.7: Solidification shrinkage in sand mold casting S3 (SEM, 10 $\mu\text{m}$ ).....	56
Figure 5.8: Microhardness distribution in the WAAM specimen M.....	57
Figure 5.9: SDAS calculated with equation (1) .....	58
Figure 5.10: SDAS calculated with equation (2) .....	58
Figure 5.11: Cooling rates based on equations (1) and (3) .....	58
Figure 5.12: Cooling rates based on equations (2) and (3) .....	58
Figure 5.13: Dendrites in FZ in the WAAM specimen M (SEM, 20 $\mu\text{m}$ ) .....	59
Figure 5.14: Dendrites in PMZ in the WAAM specimen M (SEM, 10 $\mu\text{m}$ ).....	59
Figure 5.15: Dendrites in HAZ in the WAAM specimen M (SEM, 2 $\mu\text{m}$ ).....	59
Figure 5.16: Dendrites in the middle part of the permanent mold casting P14 (SEM, 10 $\mu\text{m}$ ).....	60
Figure 5.17: Dendrites in the middle part of the sand mold casting S3 (SEM, 100 $\mu\text{m}$ ). ..	60
Figure 5.18: Based on SEM images, SDAS calculated with equation (1).....	60
Figure 5.19: Based on SEM images, SDAS calculated with equation (2).....	60
Figure 5.20: Based on SEM images, cooling rate calculated with equations (1) and (3) ..	61
Figure 5.21: Based on SEM images, cooling rate calculated with equations (2) and (3) ..	61
Figure 5.22: HAZ rejected from the SDAS, calculated with equation (1) .....	61
Figure 5.23: HAZ rejected from the SDAS, calculated with equation (2) .....	61
Figure 5.24: HAZ rejected from the cooling rate, calculated with equation (1) .....	62
Figure 5.25: HAZ rejected from the cooling rates, calculated with equation (2) .....	62
Figure 5.26: Plot of the cooling rate equation (3) for SDAS 1 to 100 $\mu\text{m}$ .....	64
Figure 5.27: Relationship between strength, elongation and SDAS .....	65
Figure 5.28: Relationship between microhardness and SDAS .....	65

## List of Tables

Table 2.1: Deposition rate and energy efficiency of the wire-feed processes LENS, EBAM and WAAM .....	21
Table 2.2: Symbol explanation for equation (4) and (5) .....	27
Table 3.1: Input parameters used for depositing AA 4047 by WAAM .....	33
Table 3.2: Dimensions of the WAAM sample AA 4047 .....	34
Table 3.3: List of specimens from both casting and WAAM. P15, P16 and U are saved for eventual further work .....	36
Table 3.4: Tensile test data input .....	38
Table 5.1: Comparing the SDAS [ $\mu\text{m}$ ].....	62
Table 5.2: Comparing the cooling rates [ $\text{Ks}^{-1}$ ] .....	63

# Abbreviation

3D	Three-dimensional
AA	Aluminum Association
Al	Aluminum
AM	Additive Manufacturing
BSE	Back-Scattered Electrons
GBP	Great British Pound
CAD	Computer Aided Design
DPH	Diamond Pyramid Hardness
E	Elastic modulus / Young's modulus
EBSD	Electron Backscatter Diffraction
EBAM	Electron Beam Additive Manufacturing
EL	Elongation
FZ	Fusion Zone
GMAW	Gas Metal Arc Welding
GTAW	Gas Tungsten Arc Welding
HAZ	Heat-Affected Zone
HV	Vickers Pyramid Number
LENS	Laser Engineering Net Shape
LOM	Light Optical Microscopy
min	Minute
MTP	Department of Mechanical and Industrial Engineering
NTNU	Norwegian University of Science and Technology
PMZ	Partially Melted Zone
P	Permanent Mold Casting
SEM	Scanning Electron Microscopy
SDAS	Secondary Dendrite Arm Spacing
S	Sand Mold Casting
s	Second
SE	Secondary Electrons
Si	Silicon
SINTEF	Norwegian: Stiftelsen for Industriell og Teknisk Forskning
Sr	Strontium
WAAM	Wire and Arc Additive Manufacturing

# Symbols

$E_0$	Accelerating voltage
$\alpha$	Alfa
A	Contact surface between the casting and the mold
C	Celsius
$\Delta T/t_s$	Cooling rate
n	Constant fitting
°	Degree
$\Delta$	Delta



$\rho_m$	Density of the metal
$\rho$	Density of the mold
$\emptyset$	Diameter
B	Fitting Factor
$T_0$	Initial temperature of the mold
J	Joule
K	Kelvin
kg	Kilogram
L	Latent heat of fusion
L	Length
$T_m$	Melting temperature of the liquid
$\mu$	Micro
B	Mold constant
N	Number
%	Percent
£	Pound sterling (GBP)
$\lambda$	SDAS
s	Second
s	Solidification time
$c_m$	Specific heat of the metal
c	Specific heat of the mold
$\varepsilon$	Strain
$\sigma$	Stress
$\Delta T_s$	Superheat ( $T_m - T_0$ )
T	Temperature
$T_{pour}$	Temperature of the pour
k	Thermal conductivity of the mold
t	time
$\sigma_{UTS}$	Ultimate Tensile Strength
V	Volume of the casting
W	Watt
$\sigma_Y$	Yield Strength



# 1 Project Description

## 1.1 Background

It is desirable to extend the successful additive manufacturing (AM) technology for polymers to embrace metals. As the mechanical properties of metallic materials are highly dependent of the processing methods chosen, SINTEF Industry has started a research program to explore the additive manufacturing by welding.

Wire and arc additive manufacturing (WAAM) is a modern technique for producing three-dimensional (3D) parts by layer-by-layer deposition of material controlled by computer aided design (CAD). WAAM requires less production time and resources than other AM processes, and is more environmentally friendly due to less waste compared to conventional manufacturing methods e.g. milling. The WAAM technology is discussed in the preliminary study "Additive Manufacture –Materials and Processes", a specialization project by Annbjørg Horgar (2017). A scientific paper with this topic is also published in Journal of Materials Processing Technology [1].

Today there are little literatures on the WAAM field, especially regarding to the cooling rate. The material study of the aluminum alloys processed by WAAM is often limited to the alloys with good weldability. The aluminum casting technology is older, has larger literature resources and collects several studies about the cooling rate and how it affects the material behavior for various metals. The development of WAAM can derive advantage from the casting literature. Hence, it was decided to carry out a comparison study of aluminum samples processed by the WAAM and the casting process to examine the relationship.

The overall objective of the project is to produce aluminum-silicon samples by the WAAM and the casting process and then to compare the samples with respect to the mechanical and the microstructural properties.

## 1.2 Structure of the Project Report

### 1 Project Description

- Introduction to the problem, the background and the report structure
- Theoretical approach to the wire and arc additive manufacturing and the casting process, the aluminum-silicon alloys and methods for calculating the secondary dendrite arm space and the cooling rates

### 2 Literature

- Literatures and methods applied in the report

### 3 Materials, Testing and Characterization

- Explanation of the experimental approach and the methodology
- Materials consumed, production and preparing of the test specimens and the methods of test and analysis

### 4 Results

- Test results, analysis, calculations and images

### 5 Discussion

- Reflection and interpreting of the results

### 6 Conclusion

- Final derivation of the results and the discussion
- Recommendation for further work

### 7 References

- Cited literatures and resources

### Appendix

- Data sheets, images, calculations and data

## 2 Literature

### 2.1 Wire and Arc Additive Manufacturing (WAAM)

Wire arc additive manufacturing (WAAM) is a welding process method using wire-feeding and industry robots. The WAAM is the most promised manufacturing technology with higher deposition rate, energy efficiency, safe operation and lower cost than conventional manufacturing methods i.e. milling. The energy efficiency of gas metal arc welding (GMAW) or gas tungsten arc welding (GTAW) can be as high as 90% compared with the other wire-feed processes Laser Engineering Net Shape (LENS) and Electron Beam Additive Manufacturing (EBAM), see Table 2.1. WAAM using GMAW or GTAW can be profitable for small-series production, complex design or aerospace components of medium to large dimensions.

<b>Wire-feed process</b>	<b>Deposition rate</b>	<b>Energy efficiency</b>
	<i>[g/min]</i>	<i>[%]</i>
LENS	2-10	2-5
EBAM	2-10	15-20
WAAM	50-130	90

**Table 2.1: Deposition rate and energy efficiency of the wire-feed processes LENS, EBAM and WAAM**

The WAAM can deposit single-layer, multi-layers or a combination of both. Accurate models are required for the single bead geometries and the multi-bead overlapping to determine surface quality and dimensional accuracy of the final part. The weld beads have high cooling rate and solidify faster as there are less material and lower heat input. Enough heat input is essential to ensure fusion between the beads and to avoid delamination and must be paid attention to in the models. The edges of the layers are fully or partially melted so that the microstructure becomes more homogeneous [2].

A typical weld bead can be divided into three zones, the first is the fusion zone (FZ) where the beads are completely melted, i.e. the next depositing layer is fully melted with the adjacent beads. The zone next to FZ is not fully melted and is called partially melted zone (PMZ). The heat-affected zone (HAZ) is the underlying layers reheated by the next depositing layer and introduced recrystallization and grain structure alteration. Often, the fusion zone has equiaxed grains, the PMZ columnar grains and the HAZ small and fine grains.

To exemplify the economies, a cost study by Guo [3] of the WAAM and the casting process for a given real-world case is plotted in Figure 2.1. The currency used is Great British Pound (GBP) by the valuate symbol £ for pound sterling. The cost curves illustrate the cost per product, and the point of intersection between the WAAM and the casting process is on 40 products and £30 apiece. For product series with fewer than 40 products, the cost curve escalates for the casting process due to the fixed production cost e.g. producing the mold and the melting process and time. Rapid prototyping is produced in small series and can cost between £200 and 850 apiece when casted, while the WAAM costs between £30 and 100 apiece.

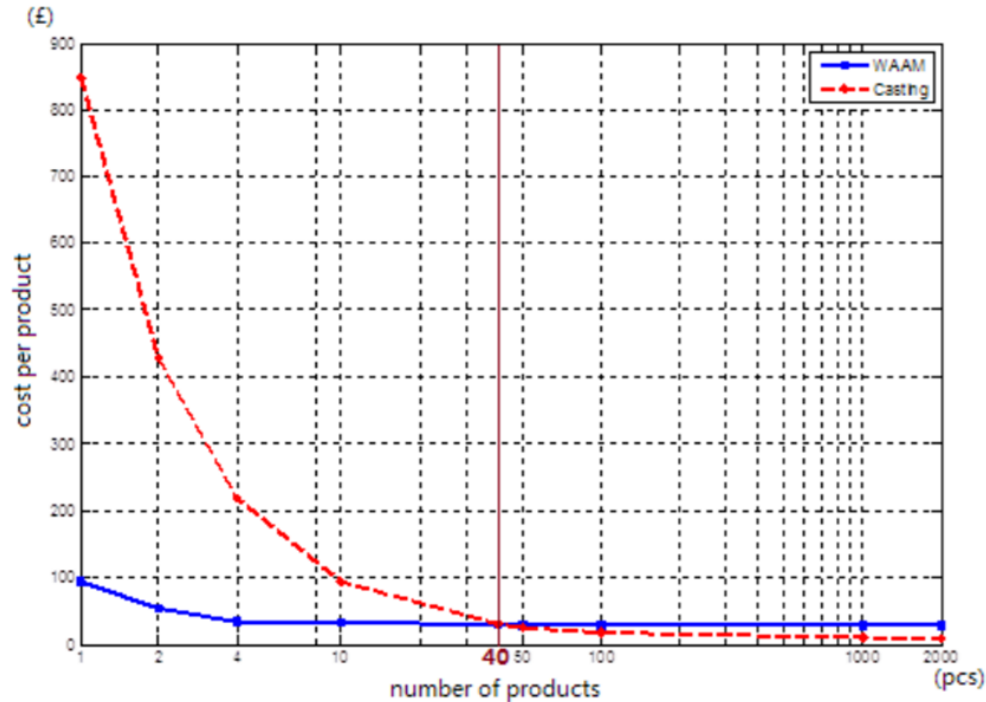


**Figure 2.1: Cost analysis for a real-world case produced by the WAAM and the casting process [3]. The curves are cost per product in pound (£) for number of products in serial production.**

## 2.2 Aluminum-Silicon Alloy (Al-12Si)

Silicon (Si) is one of the principal alloying elements in the aluminum alloys and has great solubility that is easy to control. The equilibrium phase diagram for binary Al-Si alloys is shown in Figure 2.2. The (Al)+(Si) eutectic structure defines many of the properties, among the castability and the weldability [4]. The (Si) concentration is often subdivided into two components, where the first is (Si) concentration below 1.65% and the second above 20%. At equilibrium conditions, <1.65% (Si) exists in solid solution or as precipitates, while >20% is constituent primary (Si) particles or phases [4].

Al-12Si is characterized as an eutectic alloy where eutectic is the principal microconstituent and form by around 577°C [4]. It is the lowest eutectic temperature and the solidification range becomes very small, the Al-12Si alloys can form only small amounts of macro-segregation and are therefore common.

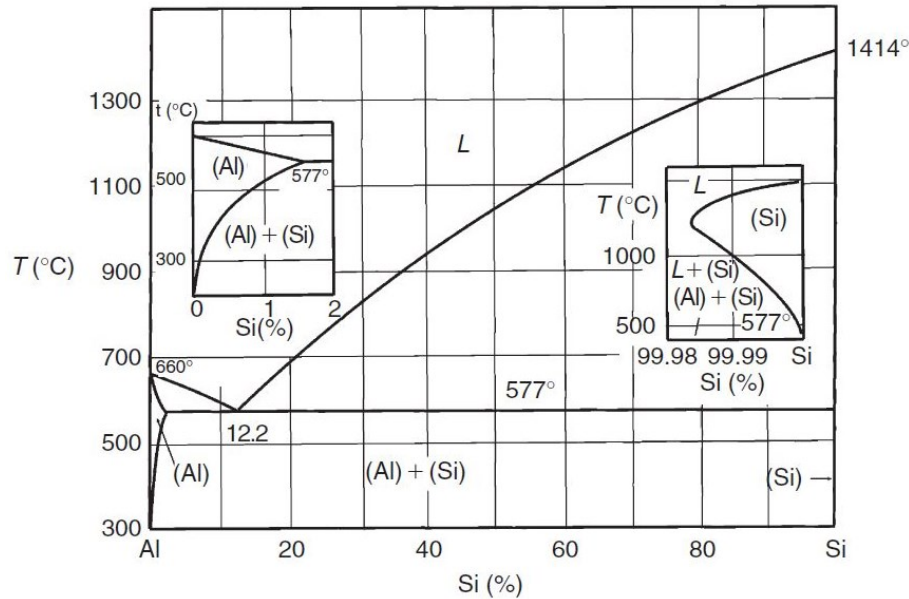


**Figure 2.2: Phase diagram Al-Si [4]**

Strontium (Sr) additions in small amount approximate 0.01 % into Al-Si casting alloys can increase the refined eutectic structure even for the sand mold casting. Modification by Sr additions gives a more dispersion of eutectic colonies and smaller silicon crystallite sizes in the microstructure [4].

Extremely high purity is required in industries like aerospace as the mechanical properties of aluminum alloys can be severe affected by impurities like iron or silicon, e.g. iron from the steel mold during the casting process. Sharp-edged particles can drastic restrict the elongation, the fracture toughness and the fatigue resistance [4].

### 2.3 Secondary Dendrite Arm Spacing (SDAS)

In commercial production of aluminum alloys, the cooling rate usually form a dendritic microstructure which determines the material properties. The crystal dendrites are long and narrow with tree-like arms, see Figure 2.3. The dendrites form when the solute in the pure liquid is exposed to constitutional supercooling during the solidification, where the solute temperature is lower than the liquid temperature. As the lower heat-input in WAAM introduces higher cooling rates in the fusion zone (FZ) and lower in the partially melted zone (PMZ), the dendrites become smaller in the FZ and larger in the PMZ.

The average secondary dendrite arm spacing (SDAS) is a commonly used method for analyzing this dendritic microstructure. The mechanical properties of the material are related to the SDAS, i.e. the strength and the hardness increases with decreasing SDAS [5].

Interdendritic shrinkage can occur between the dendrite arms and is called microshrinkage or shrinkage porosity [6]. The dendrites obstruct the liquid from flowing into the solid interface and shrinkage arises. Smaller dendrites formed at higher cooling rates can reduce the obstacle and allow the liquid flow to solidity in the solid interface see Figure 2.4 [6]. Inclusion can also nucleate between the dendrite arms [6].

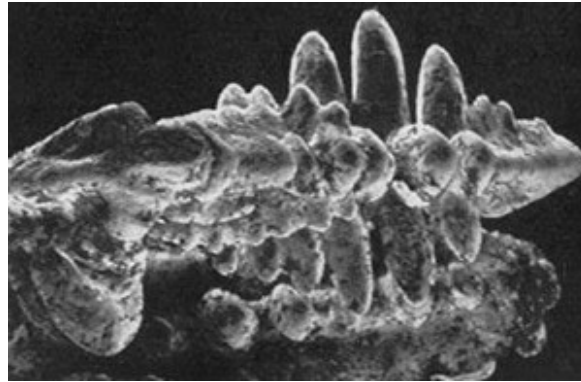


Figure 2.3: Dendrites in steel (SEM, 15x) [6]

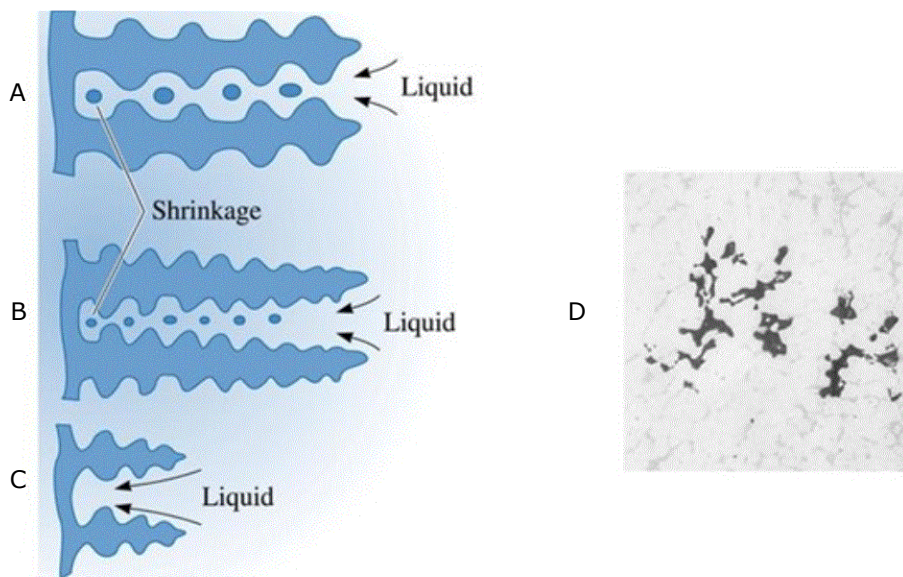
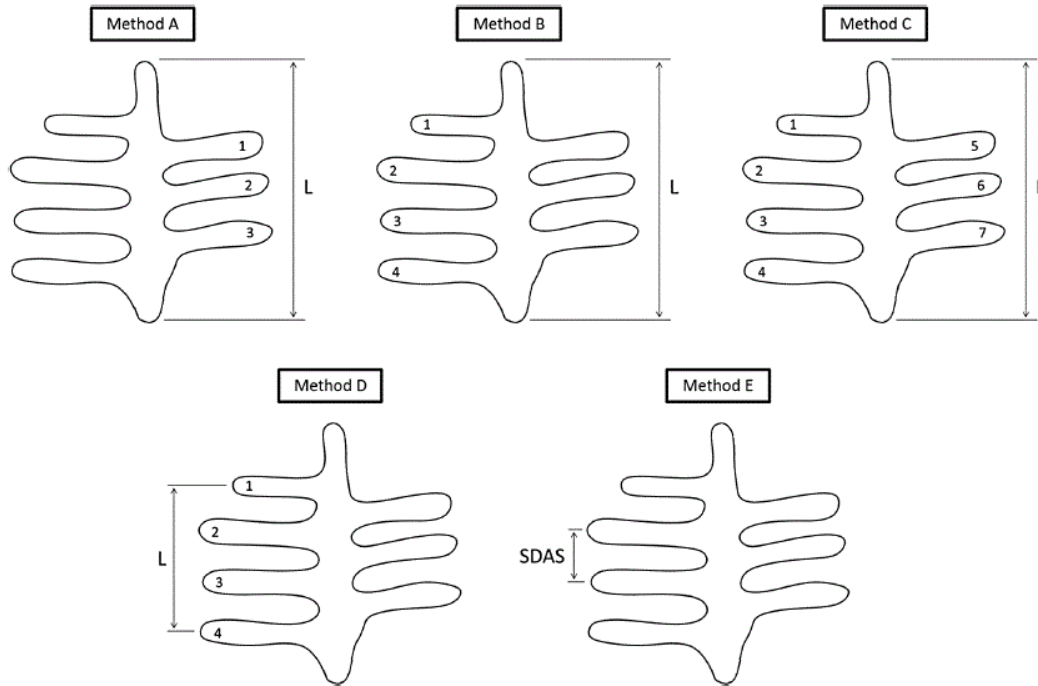


Figure 2.4: Interdendritic shrinkage. A) The liquid flow is obstructed by the dendrite arms. B) Smaller dendrites can distribute equally or C) avoid the shrinkage by letting the liquid flow to the solidifying solid interface. D) Interdendritic shrinkage in an aluminum alloy (80x) [6]

Unfortunately, the literature uses different methods for measuring the SDAS and the results can contain dissimilarity. Vandersluis and Ravindran [5] investigated the most commonly methods in the literature and picked out five methods for the comparison, see Figure 2.5. They recommended in their conclusion to adopt method D with the equation (1) for all SDAS measurements.  $N$  is the number of arms within the length  $L$  measured between two dendrite arms, see method D in Figure 2.5. Method D is also commonly used by SINTEF and NTNU, hence it will be used throughout this thesis.

$$SDAS = \frac{L}{N - 1} \quad (1)$$





**Figure 2.5: Schematic representation of five SDAS measurement methods [5]. Method D is recommended and will be used in this thesis.**

## 2.4 Cooling Rates

The literature results state that the cooling rate can be crucial to the microstructure regarding to the solidification and the formation of dendrites and interdendritic shrinkage:

Alloys with higher silicon contents such as 4047 have fewer primary aluminum dendrites and are less likely to exhibit interdendritic shrinkage and cracks as interdendritic feeding is able to fill the space between dendrite before the metal is fully solidified. Haselhuhn et al. [2].

The microstructural analysis in the same study discovered larger growth of eutectic microconstituent in AA 4047 (Al-12Si wrought alloy) and measured the average SDAS to approximate 8.2  $\mu\text{m}$ . SDAS of 10  $\mu\text{m}$  is common in welding compared to 100  $\mu\text{m}$  in casting [2]. According to [2], we can calculate the characteristic cooling rate using the SDAS through equation (2) and (3). The variables are length  $L$  in  $\mu\text{m}$ , number of secondary dendrite arm spaces  $N$ , fitting factor  $B$  and constant  $n$ . The constants were drawn from AA 4043 (Al-5Si wrought alloy):  $B = 50 \mu\text{m} (\text{Ks}^{-1})^n$  and  $n = 0.33$  [2]. Note that this study has different denominator in the equation (2) for SDAS, where the length  $L$  was measured edge to edge across three or more secondary dendrite arms (Figure 2.6). The variation is discussed in Chapter 5.

$$SDAS = \frac{L}{N} \quad (2)$$

$$Cooling\ rate = \left( \frac{B}{SDAS} \right)^{1/n} \quad (3)$$

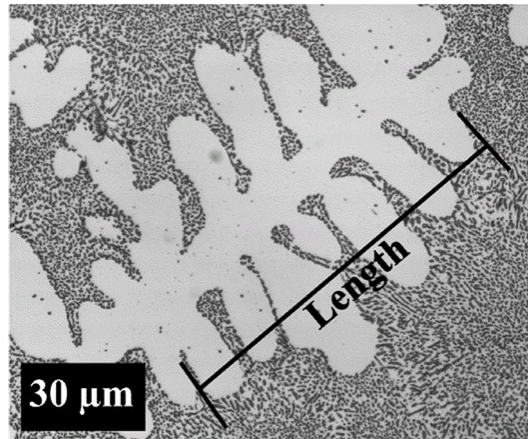


**Figure 2.6: Measuring the length  $L$ , edge-to-edge [7]**

Although the casting solidifies slower, Haselhuhn, Sanders and Pearce [7] obtained in their study corresponding cooling rates between  $210$  and  $270 \text{ Ks}^{-1}$  for AA 4047 by using the wedge-shaped method. The wedge casting sample is narrow at bottom and wide at top, see Figure 2.7. The cooling rate is high by the narrow end and decreases upwards the top. By reproducing the wedge casting sample, we can cast a sample that matches the cooling rates in the WAAM sample.

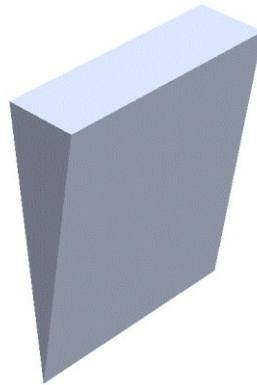


**Figure 2.7: Wedge casting sample**

## 2.5 Casting

According to the wedge-shaped casting study it is found that the casting alloys resembled to the welded alloy and hence, the casting literature could be utilized to characterize the WAAM parts [7]. Characterizing of the microstructure using the casting literature can help us understanding the material behavior of aluminum samples produced by WAAM.

The wedge-shaped method can with some modifications be used to produce several castings for comparing and verification in the experimental approach. An awl-shaped mold design will correspond more to a weld bead and to obtain a symmetric design, less material and shorter solidification time.

The solidification is slower in casting due to larger mass and starts on the outer edges and towards the core. This forms smallest microstructural elements, also known as chill grains, on the edges, columnar grain growth towards the core and large equiaxed grain in the core [2].

A riser is necessary to avoid shrinkage and cavities in the castings and the riser dimensions can be calculated using the Chvorinov's rule in equation (4), where V and A are the volume of the casting and A is the contact surface area between the casting and the mold, see Table 2.2 for the symbol explanation [6]. B is the mold constant and can be calculated by equation (5) [8]. Be aware of that the source for this equation could not be verified as the sources were not available for check on this time. The equation is found in the article about Chvorinov's rule [8] on the web site *Wikipedia* with no available sources, hence the constant B is used for guiding only and must not be used in the dimension design. According the literature the constant B could be determined experimental for a given mold material by casting test specimens, or by using the same material for both the riser and the mold and Chvorinov's rule [9]. The methods are not feasible in this study, hence the equation (5) will be used as an example only.

$$t_s = B \left( \frac{V}{A} \right)^n \quad (4)$$

$$B = \left[ \frac{\rho_m L}{(T_m - T_0)} \right]^2 \left[ \frac{\pi}{4kpc} \right] \left[ 1 + \frac{c_m \Delta T_s}{L} \right]^2 \quad (5)$$

Solidification time	$t_s$	s
Volume of the casting	V	$m^3$
Contact surface between the casting and the mold	A	$m^2$
Mold constant	B	$s/m^2$
Melting temperature of the liquid	$T_m$	K
Initial temperature of the mold	$T_0$	K
Temperature of the pour	$T_{pour}$	K
Superheat ( $T_m - T_0$ )	$\Delta T_s$	K
Density of the metal	$\rho_m$	$kg/m^3$
Specific heat of the metal	$c_m$	J/kgK
Latent heat of fusion	L	J/kgK
Thermal conductivity of the mold	k	W/mK
Density of the mold	$\rho$	$kg/m^3$
Specific heat of the mold	c	J/kgK

**Table 2.2: Symbol explanation for equation (4) and (5)**



## 3 Materials, Testing and Characterization

### 3.1 Introduction

Chapter 3 examines the mechanical and microstructural properties of samples produced by WAAM using gas metal arc welding (GMAW) and by casting process. The materials and the methods are described in the beginning of the chapter, while the test results and the characterization are collected, evaluated and discussed at the end of this chapter.

### 3.2 Materials

The aluminum-silicon alloy Al-12Si is found to be suitable for WAAM processes with almost no cracks and very low porosity levels in the microstructure [2]. The alloy provides good mechanical properties and excellent weldability. The alloy is available both as weld filler wire AA 4047 from Safra SPA and as direct chill casted Al-12Si ingots from Hydro Sunndal Metallverk (data sheets in Appendix). Due to good castability and weldability as presented in Section 2.2, we decided to choose Al-12Si as the AM material for this experiment. 150 ppm strontium is added to melted Al-12Si ingot for the casting to refine the eutectic structure and reduce the silicon crystallite sizes [4], see Section 2.2.

### 3.3 Sample Preparation

#### 3.3.1 Castings

The awl-sharped design was chosen as it can achieve wide range of cooling rates in one and same part [7] and can correspond better to weld bead, see Section 2.5. Total 7.1 kg direct chill casted Al-12Si ingot was heated up to 700-730°C and added 1.1 g strontium, representing 150 ppm of the total melt. The homogeneity in the castings depended on the casting rate by manual operation.

A total number of 19 castings were produced, whereof 16 were cast in permanent mold and three in sand molds. The procedures for producing and casting into the permanent mold and the sand molds are described in Section 3.3.2 and 3.3.3 respectively. We used the tilt feeding method named *Durville casting process* for manual feeding, see Figure 3.1.

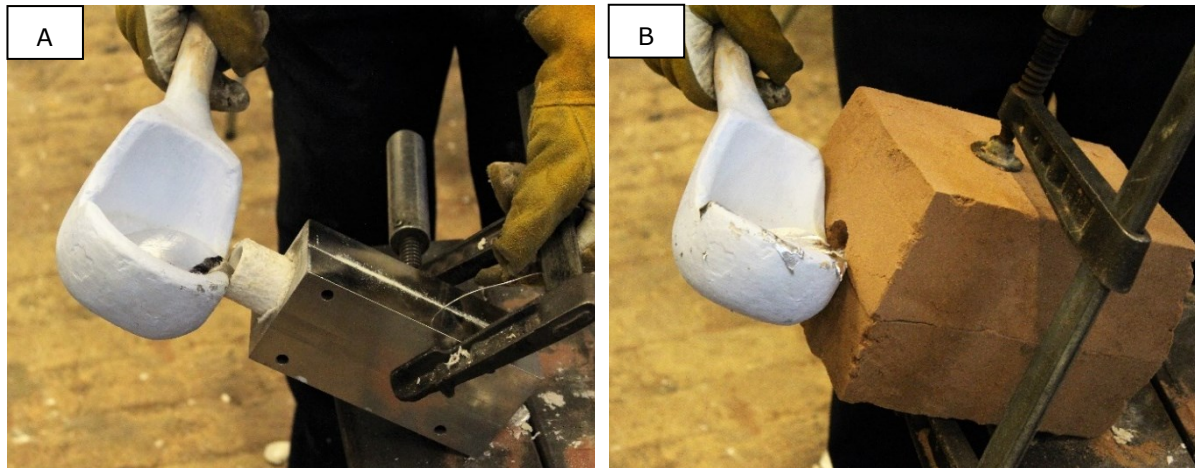


**Figure 3.1: Durville casting process.**

**A) Feeding in the permanent mold through the insulating bush and B) directly in the sand mold**

The castings are marked as shown in Figure 3.2, permanent mold casting numbers P1 to P16 and sand mold casting numbers S1 to S3. The length of the ruler on the left side in each image is 150 mm. The permanent mold castings P1 to P5 were rejected due to low start temperatures (see Section 3.3). The specimens P6 to P11 were sorted out for the tensile testing in a direction longitudinal to the length. The specimens P12, P13, P14, S1, S2 and S3 were used for the microstructural analysis.

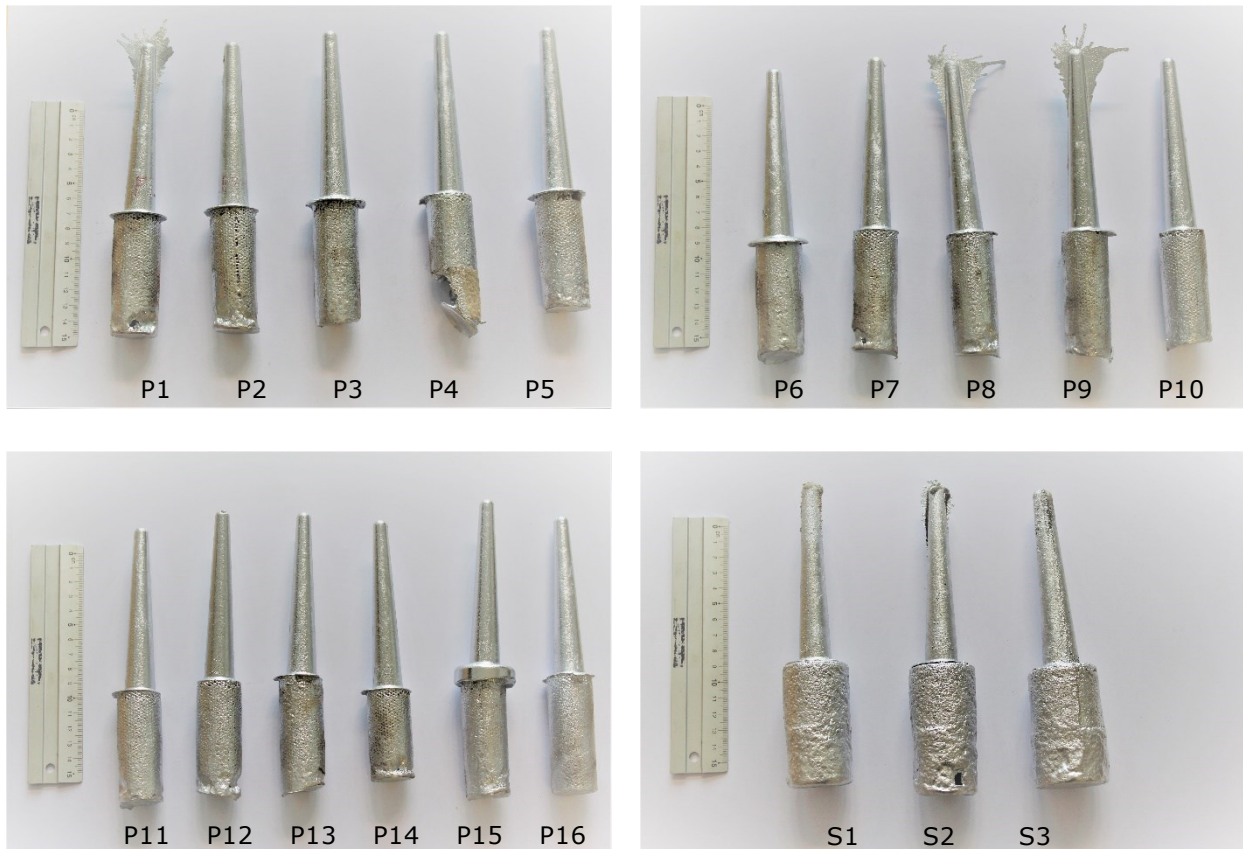


**Figure 3.2: Casting identities. Permanent mold castings P1 to P16 and sand mold castings S1 to S3. The length of the ruler on the left side in each image is 150 mm.**

### 3.3.2 Permanent Mold

The permanent mold was machined from structural steel block with dimensions as described in Figure 3.3. To compensate the shrinkage, an insulating aluminum silicate fiber bush from Internet Products LTD is used as riser and placed in the interface hole  $\text{Ø}40 \times 20$  mm in top of the mold (Figure 3.1 A). The permanent mold is coated with an anti-sticking film *DCA060839* from Cherm-Trend L.S prior to the casting for easy releasing of the samples, see Figure 3.4.

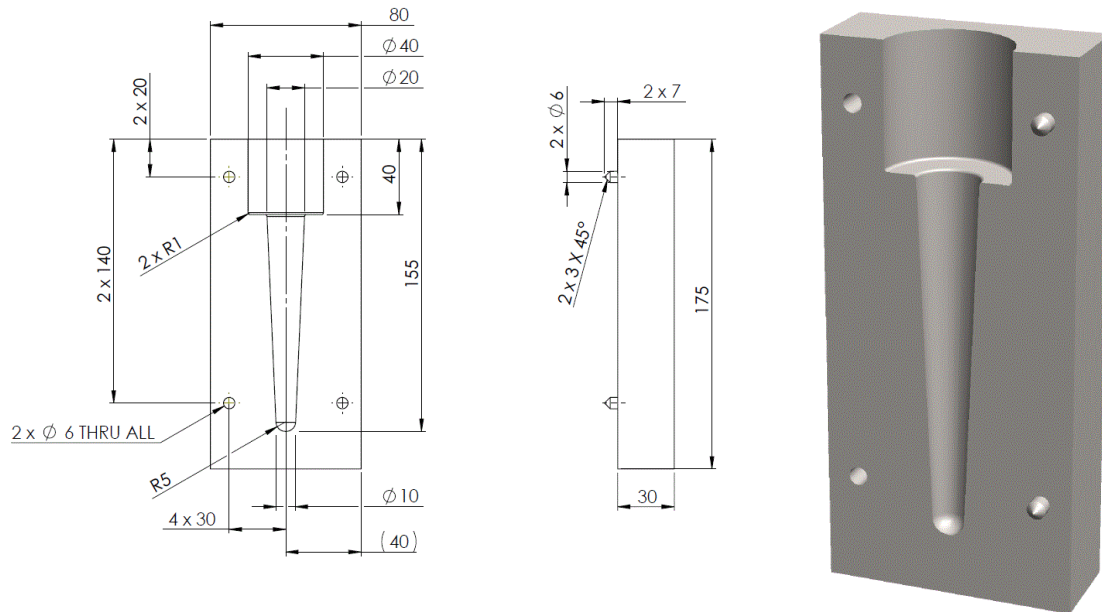


**Figure 3.3: Permanent mold drawing dimensions and 3D-model**

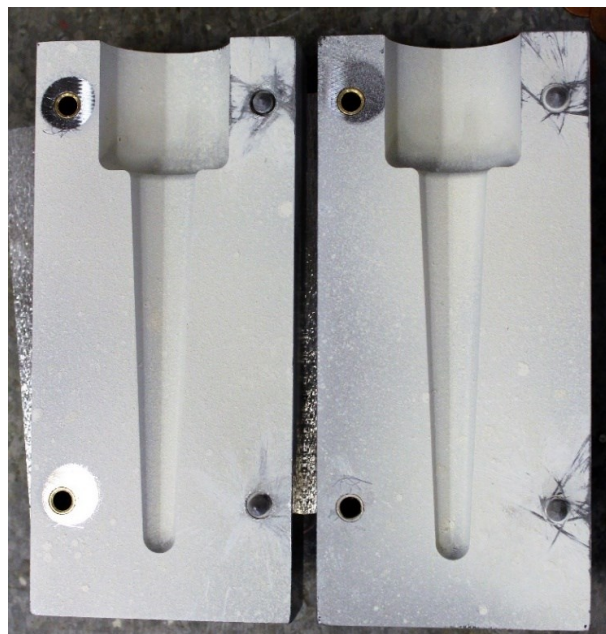


**Figure 3.4: Permanent mold coated with anti-sticking film**

Common start temperature in the permanent mold was on approximal 200°C, measured using a K-type thermocouple with data logging wired to the permanent mold. The temperature log curve for the casting is illustrated in Figure 3.5. As the initial temperature of the permanent mold was the room-temperature 20°C, the permanent mold needed to be heated up to 200°C.

The heating was done by repeating casting the samples until the mold exceeded 200°C for the fifth sample after around 30 minutes, the temperature range is marked "start-up" in Figure 3.5. The feeding started again for the sixth casting sample when the permanent mold had cooled down to roughly 200°C. From this sample, the temperature log clearly indicates a steady-state heating cycle as marked in the Figure 3.5. The procedure repeated for the casting number seven to 16. The dwell time before opening the permanent mold was minimum three minutes.

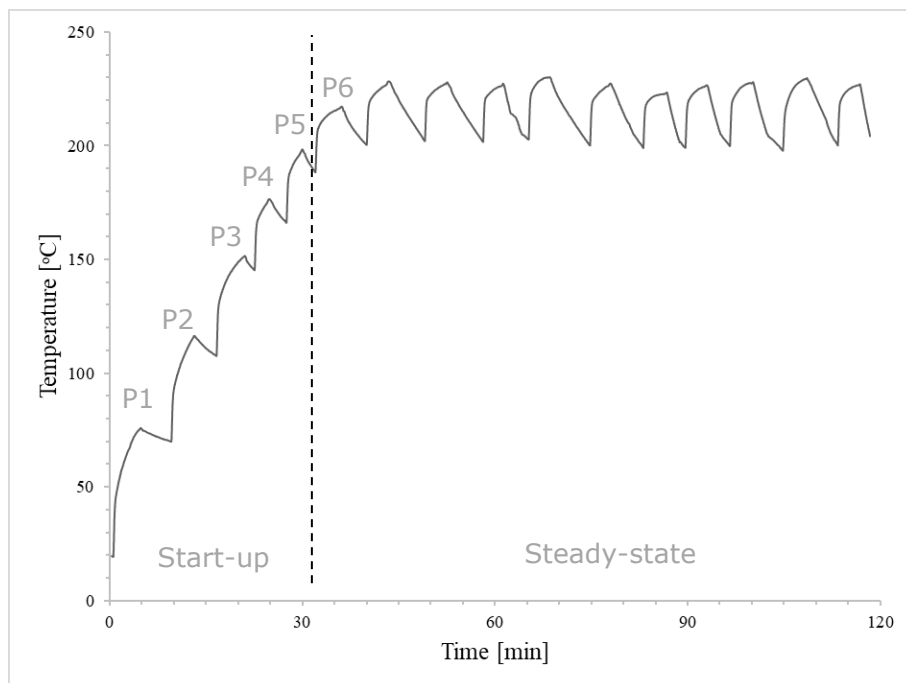


**Figure 3.5: Temperature log for casting AL-12Si in permanent mold. Sample P1 to P5 were rejected due to uneven casting start temperature.**

### 3.3.3 Sand Mold

The sand mold is formed using six filling boxes with sand and the impression of the second permanent mold casting included the insulating bush, see Figure 3.6. First, fresh foundry sand mixed with a bonding agent was packed into a with half of the casting submerged in the top surface. Then the casting was removed after achieving full bonding force and the mold can be assembled with its mirrored pair. A total of three pairs of sand molds are made and can be used only once as the sand will dissolve when releasing the casting after end process.

The three sand molds were uniform and kept at a room temperature of 20°C degree, hence no temperature log was necessary. The dwell time before releasing the samples was minimum 30 minutes for the sand molds.








**Figure 3.6: Forming the sand mold, with impression of a permanent mold casting**

### 3.3.4 WAAM Sample

Filler wire AA 4047 with diameter of  $\varnothing 1.2$  mm and a 15 x 260 x 334 mm AA 6082-T6 plate are used in the production of a WAAM sample. Both filler wire and plate were readily available in stock. We programmed the industrial robot (ABB IRB2400) to weld the filler wire AA 4047 layer-by-layer onto the substrate plate fixed to the work bench. The average welding parameters are registered and listed up in Table 3.1.

<b>I</b>	<b><math>\Omega</math></b>	<b></b>	<b></b>	<b></b>
<b>Current</b>	<b>Voltage</b>	<b>Heat input</b>	<b>Wire feed speed</b>	<b>Travel speed</b>
<i>[A]</i>	<i>[V]</i>	<i>[kJ/mm]</i>	<i>[m/min]</i>	<i>[mm/s]</i>
137.2	21.9	4.4	6.4	9.0

**Table 3.1: Input parameters used for depositing AA 4047 by WAAM**

The WAAM sample has the shape of a typical rectangular casting with larger thickness (Figure 3.7) to analyze how the thickness will affect the cooling rates and subsequently the microstructure and the grain formation.

The bead center spaces were set to 6.0 mm for the two first layers to fuse the deposited material AA 4047 to the substrate plate AA 6068. The heat input was also larger for the two initial layers. Afterwards, the input parameters were adjusted in accordance with Table 3.1 and the bead center spaces to 5.3 mm. The merging required higher heat input and wire feed speed, which results in higher material flow. To compensate it, the bead center was increased to 6.0 mm. Also, the welding process between each layer was paused until the overall temperature of the workpiece had decreased to approximate 200°C. The interpass temperature, or the start temperature, can therefore be set to 200°C as for the castings.

Dimensions, volume and mass of the WAAM sample are listed in Table 3.2. A total number of 657 beads is deposited in a bi-directional zig-zag pattern, see Figure 3.8. Total production time was 18 hours.

Height	Width	Length	Total beads	Total volume	Total mass
[mm]	[mm]	[mm]		[mm <sup>3</sup> ]	[kg]
70	100	180	657	1 424 500	3.79

**Table 3.2: Dimensions of the WAAM sample AA 4047**



**Figure 3.7: Part deposited by WAAM. Rectangular block**



**Figure 3.8: Weld beads from the front view**

The WAAM sample was then machined into test specimens as modelled in Figure 3.9. The specimens for the tensile testing were marked X, Y and Z for tension load in the tensile directions XYZ respectively, where the x-direction goes along the bead, the y-direction abeam and the z-direction layer on layer upwards.

As modelled in Figure 3.9, the remaining material marked M was machined for the microstructural analysis and the material marked U is unused. The specimens are marked X1, X2, X3, X4, X5 and X6, Y1, Y2, Y3, Y4 and Y5, Z1, Z2, Z3, Z4, Z5 and Z6 and M and U.

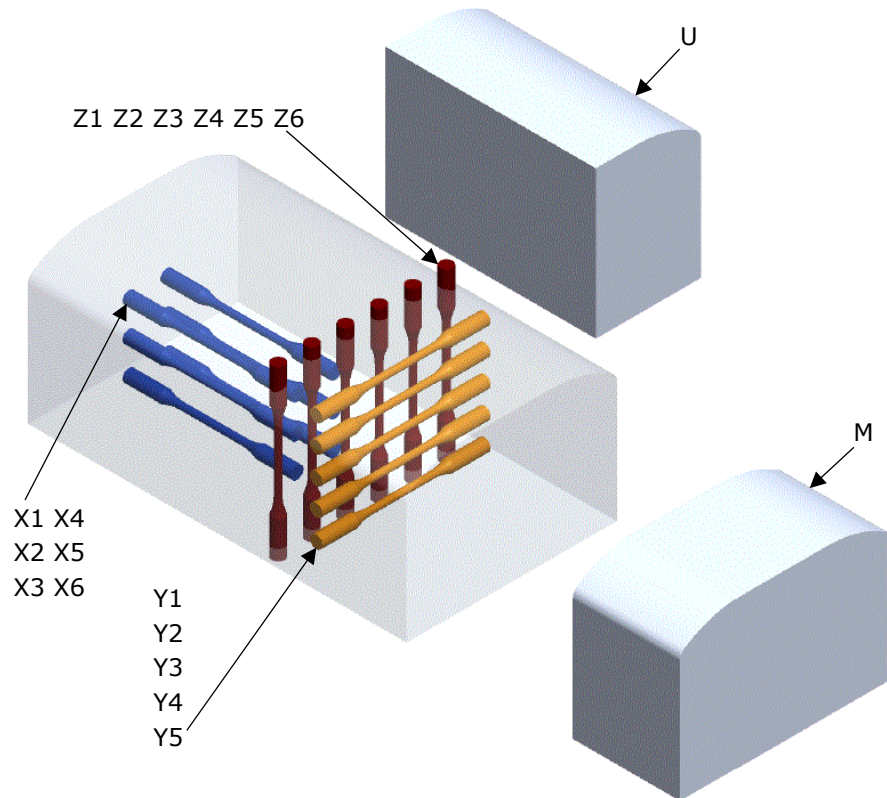


**Figure 3.9: WAAM specimen identities in approximate positions. X1-X6: Tensile test specimens in the x-direction (blue). Y1-Y5: in the y-direction (yellow). Z1-Z6: in the z-direction (red). M: Microstructural analysis specimen. U: Unused material**

### 3.3.5 List of Test Specimens

The test specimens are collected in Table 3.3 with a brief description of process method application. Specimens marked as "spare" in the column "Application" are unused specimens, available for further work.

Specimen	Process	Application	
P1	Permanent mold	Rejected	
P2			
P3			
P4		Tensile test	
P5			
P6			
P7			
P8			
P9			
P10			
P11			
P12			
P13			Microstructural analysis
P14			
P15		Spare	
P16			
S1	Sand mold	Microstructural analysis	
S2			
S3			
X1	WAAM		
X2			
X3			
X4			
X5			
X6			
Y1			Tensile test
Y2			
Y3			
Y4			
Y5			
Z1			
Z2			
Z3			
Z4			
Z5			
Z6			
M	Spare		
U			

**Table 3.3: List of specimens from both casting and WAAM. P15, P16 and U are saved for eventual further work**

## 3.4 Test Methods

### 3.4.1 Tensile Testing

A total of 23 circular tensile test specimens are machined and tested in the tensile test machine (MTS 810) in the NTNU Test Laboratory. Notice that in the WAAM specimens the y-direction goes abeam and contains multiple parallel beads. Figure 3.10 and Figure 3.11 show the dimensions of the tensile test specimens, for the WAAM specimens and the cast specimens respectively. Be aware that the WAAM specimens Z1 to Z6 became shorter than 80 mm as the height of the WAAM sample was only 70 mm.

The tensile specimen lengths 80 mm and 90 mm are used in the calculation of elongation to break for the WAAM specimens and the cast specimens respectively. The length 80 mm is also calculated for the specimens Z1 to Z6 for a better representation in the result. The reason is that any changes in the nominal gauge length 25 mm and the parallel length 30 mm would affect the mechanical properties significantly, and minor for the total specimen length 80 mm as it affects the clamping ends only. The gauge and the parallel length are the same for all the WAAM specimens.

Table 3.4 lists up the data input for the tensile test program, the nominal gauge length was set to 25 mm and positioned within the parallel length 30 mm as dimensioned in both the drawings. The strain endpoint was 0.3% as the aluminum alloys frequently fracture before 0.2%.

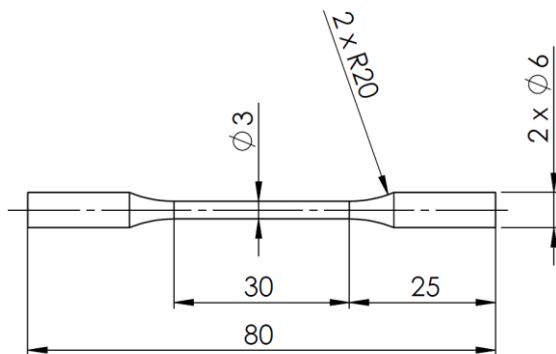


**Figure 3.10: Dimensions of the circular tensile test specimen by WAAM**

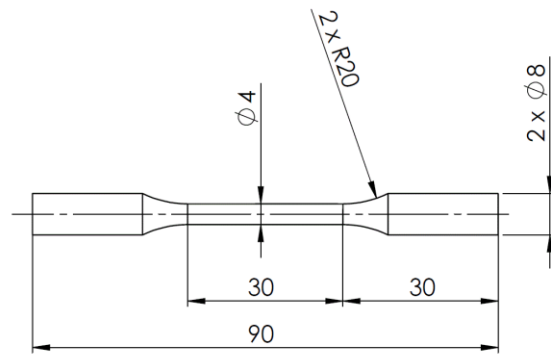


**Figure 3.11: Dimensions of the circular tensile test specimen by casting process**

Parameter	Value	Unit
Data acquisition rate	10	Hz
Gauge length	25	mm
Initial rate	2	(mm/mm)/min
Initial speed	2	mm/mm
Nominal gauge length	25	mm
Outer loop rate	100	Hz
Removal point	60	%
Secondary speed	2	mm/min
Strain endpoint	0.3	%

**Table 3.4: Tensile test data input**

### 3.4.2 Vickers Hardness Test

The hardness measurement method used is Vickers hardness test, also known as the Diamond Pyramid Hardness (DPH). The indenter is a diamond pyramid with an angle of  $\phi = 136^\circ$  on a square base as illustrated in Figure 3.12. DPH is defined as load divided by the impression area [10].

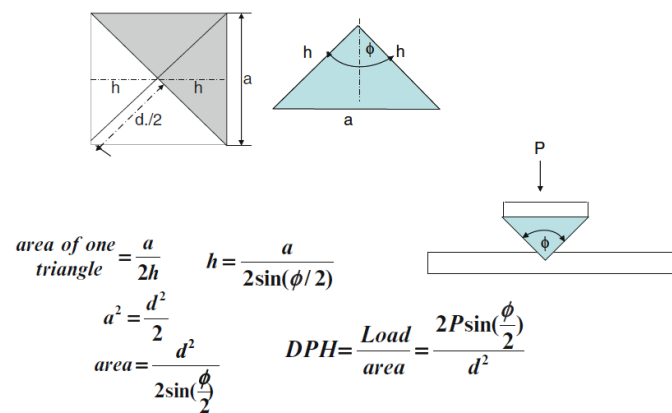


**Figure 3.12: Diamond Pyramid Hardness [10]**

The specimens were sliced, polished and analyzed in this test. The hardness test machine registered the loads and calculated the diagonals and the sloping surface of the indentation. The Vickers Pyramid Number (HV) is set to HV0.1, 100 g force in 10 seconds. The indentation interval is 350  $\mu\text{m}$  for the WAAM specimen and 350  $\mu\text{m}$  for the castings in selected fields where the microstructures alter. All indentations were taken in accordance to the standard ISO 6507-1:2018.

## 3.5 Microstructural Analysis

### 3.5.1 Preparation and Etching

The WAAM specimen M, the permanent mold castings P13 and P14 and the sand mold castings S2 and S3 are sliced, polished and then imaged by light optical microscopy (LOM). Preparation by polishing makes it possible to analyze the microstructures for weld defects and pores. P13 and S2 are etched with Keller's reagent to reveal the grain structures and the dendrites. Notice that the etching gives a brittle and coarse surface, making the specimen unsuitable for hardness measuring.

### 3.5.2 Pore Analysis

The pore analysis is carried out on sequence-imaged pictures in the image processing program ImageJ, see Figure 3.13. The images were changed to 32-bit with high threshold, and the size and the circularity in the function *Analyze Particles* were set to 0.002-Infinity mm<sup>2</sup> and 0.50-1.00 respectively.

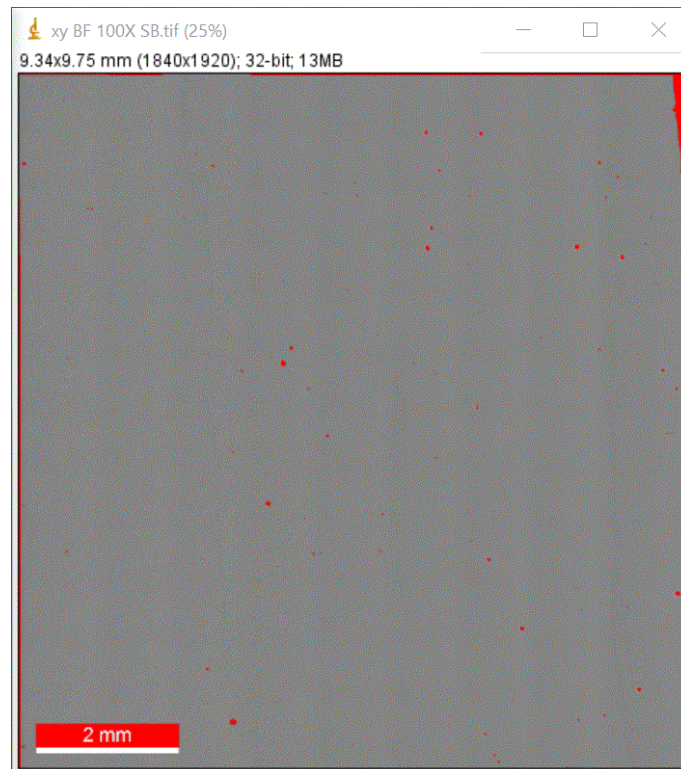


**Figure 3.13: Pore analysis in ImageJ, with threshold. Red circles are counted as metallurgical gas porosity.**

### 3.5.3 Dendrite Formation Analysis

The dendrite formations were found and imaged using LOM on the castings P13 and S2 etched by Keller's reagent. The space between the dendrite arms are measured using ImageJ (Figure 3.14) and the method D as described in Section 2.3. First, the distance between the upper and the lower dendrite arm are measured and registered. Then the secondary dendrite arm spacing (SDAS) can be calculated using the equation (1) in

method D. Finally, the cooling rates can be calculated based on the SDAS results by using the equation (3).

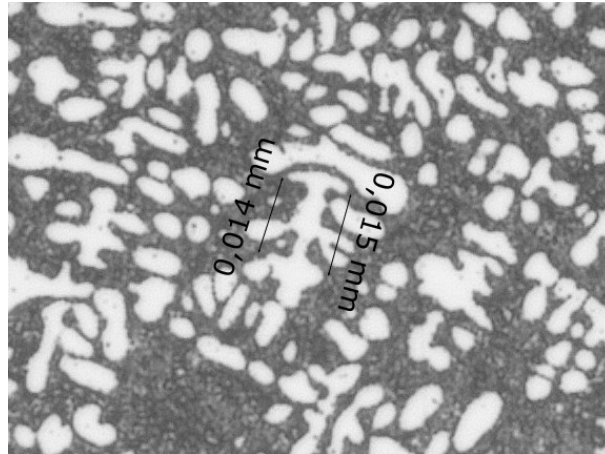


Figure 3.14: Measuring secondary dendrite arm spacing (SDAS)

#### 3.5.4 Scanning Electron Microscopy (SEM)

For elements and details that could not be interpreted from the LOM-generated images, the scanning electron microscopy (SEM), model Zeiss Ultra 55, was applied for more detailed images of the specimens with topography and composition. A total of four pieces are examined in the SEM: Microstructures of P14 and S3, and fracture surfaces of P8 and P11.

Firstly, the configuration setting is updated with an aperture radius of 30  $\mu\text{m}$ , high current mode, longer working distance to 10 mm and accelerating voltage ( $E_0$ ) at 15 keV and secondary electrons (SE) as the detected signal. Secondly, the prepared pieces are taped on the fixture plate and closed into the chamber. The vacuum pump started and worked for 5-10 minutes before it achieved high vacuum. The calibration is the third step and is done by seeking for a light point in the screen with a scalebar of 1  $\mu\text{m}$  and by wobbling it. The wobbling increases the image quality by aligning the beam perpendicular to the lens. Fourth and final step, the scanning can start and beam electrons down to the surfaces. The detector registers the scattered electrons from each point on the surface and forms an image. Desired images of scattered scales can be frozen and saved to disk, here between 20 and 500  $\mu\text{m}$ .

The signals SE and the back-scattered electrons (BSE) are used. For SE the electrons emitter closed to the surface and generates very high-resolution images. BSE are reflected electrons and can emerge from depths into the surface. BSE does not generate a high-resolution image like SE, but BSE can register distribution of different elements in the surface and is useful when scanning pores and fracture surfaces.

Finally, a short study was done by electron backscatter diffraction (ESBD) to reveal the grain structure. The configuration setting is set to an aperture radius of 120/300  $\mu\text{m}$ , high current mode, longer working distance to approximate 15-20 mm and  $E_0$  at 20 keV.



## 4 Results

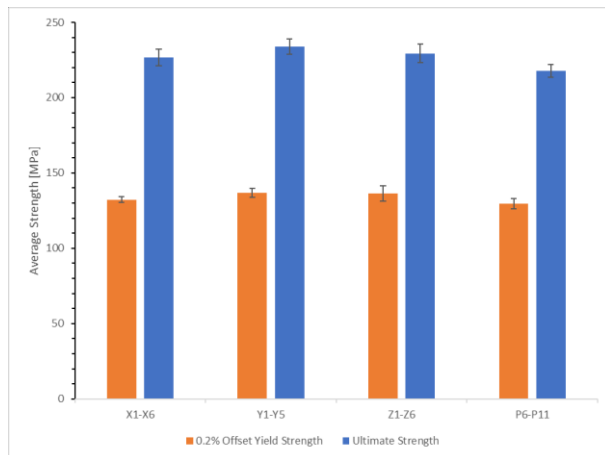
### 4.1 Mechanical Properties

The tensile test results are plotted in Figure 4.1-Figure 4.4. The average 0.2% offset yield strengths and ultimate tensile strengths are plotted in Figure 4.1, the elongations at break in Figure 4.2 and the elastic modulus in Figure 4.3. The permanent mold casting P8 (Al-12Si) is rejected and skipped from the results due to pollutions, which caused fracture at an earlier stage. The average elastic moduli are found by the Hooke's law (6) in the slope from strain  $\varepsilon$  0.002 to 0.01 for all specimens and resulted in between 61 and 82 GPa for the WAAM sample and between 45 and 71 GPa for the castings.

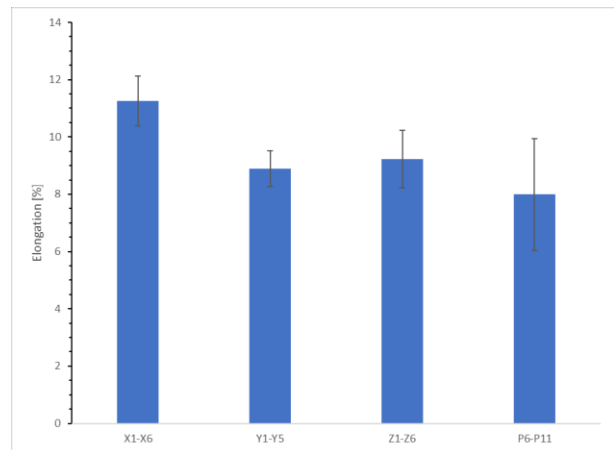
The stress-strain curves for all the tensile test specimens are schematically illustrated in Figure 4.4, the WAAM specimens (AA 4047) are in A, B and C and the castings (Al-12Si) in D. A summary of the tensile test data with details is enclosed in the Appendix. The WAAM specimens have almost identical curves, the tensile strengths are above 200 MPa for all specimens and the strains are above 0.1 for all specimens unless Z1. Pores are observed for the test specimens Y13, Y21 and Y23. Y12 had a small pore at the surface and thus fractured prematurely in this area instead of the middle.

Figure 4.4 D shows almost identical curves in the elastic field for the castings; the resemblance is discussed in Chapter 4.

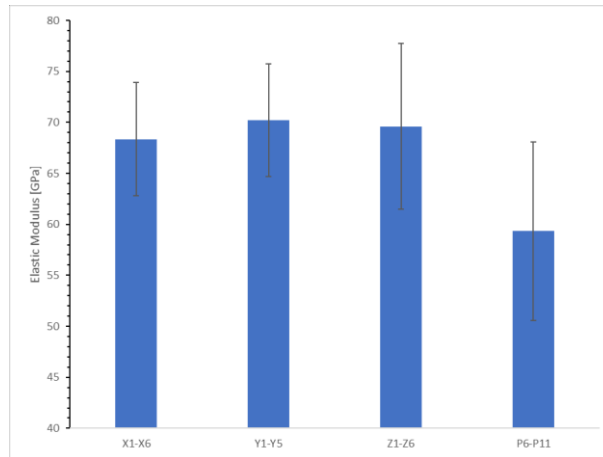
$$E = \frac{\sigma}{\varepsilon} \quad (6)$$



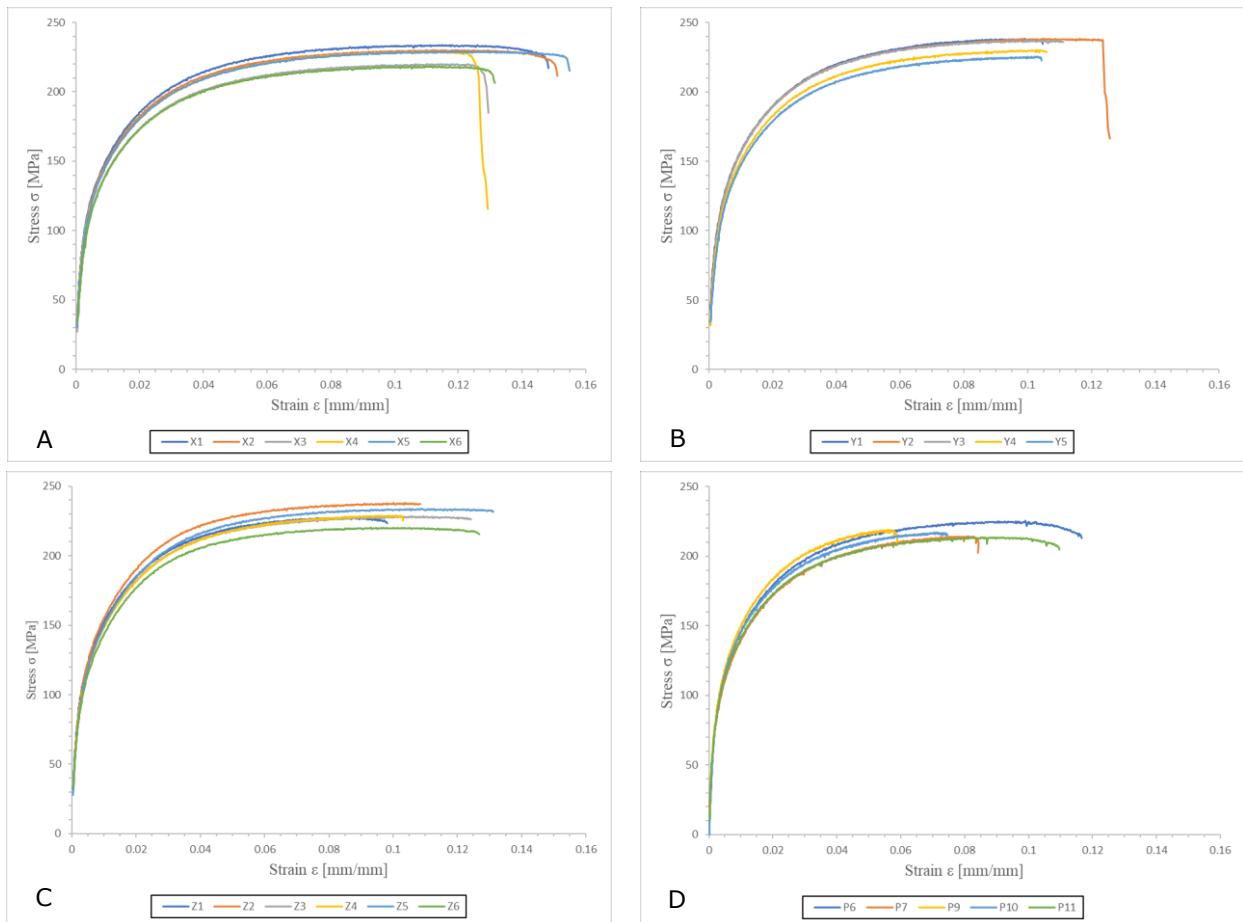
**Figure 4.1: Average 0.2% offset yield strengths and ultimate tensile strengths, registered for the WAAM specimens X1-X6, Y1-Y5 and Z1-Z6 and for the permanent mold castings P6-P11**



**Figure 4.2: Elongations at break, calculated for the WAAM specimens X1-X6, Y1-Y5 and Z1-Z6 and for the permanent mold castings P6-P11**



**Figure 4.3: Average elastic moduli calculated for the WAAM specimens X1-X6, Y1-Y5 and Z1-Z6 and for the permanent mold casting P6-P11**



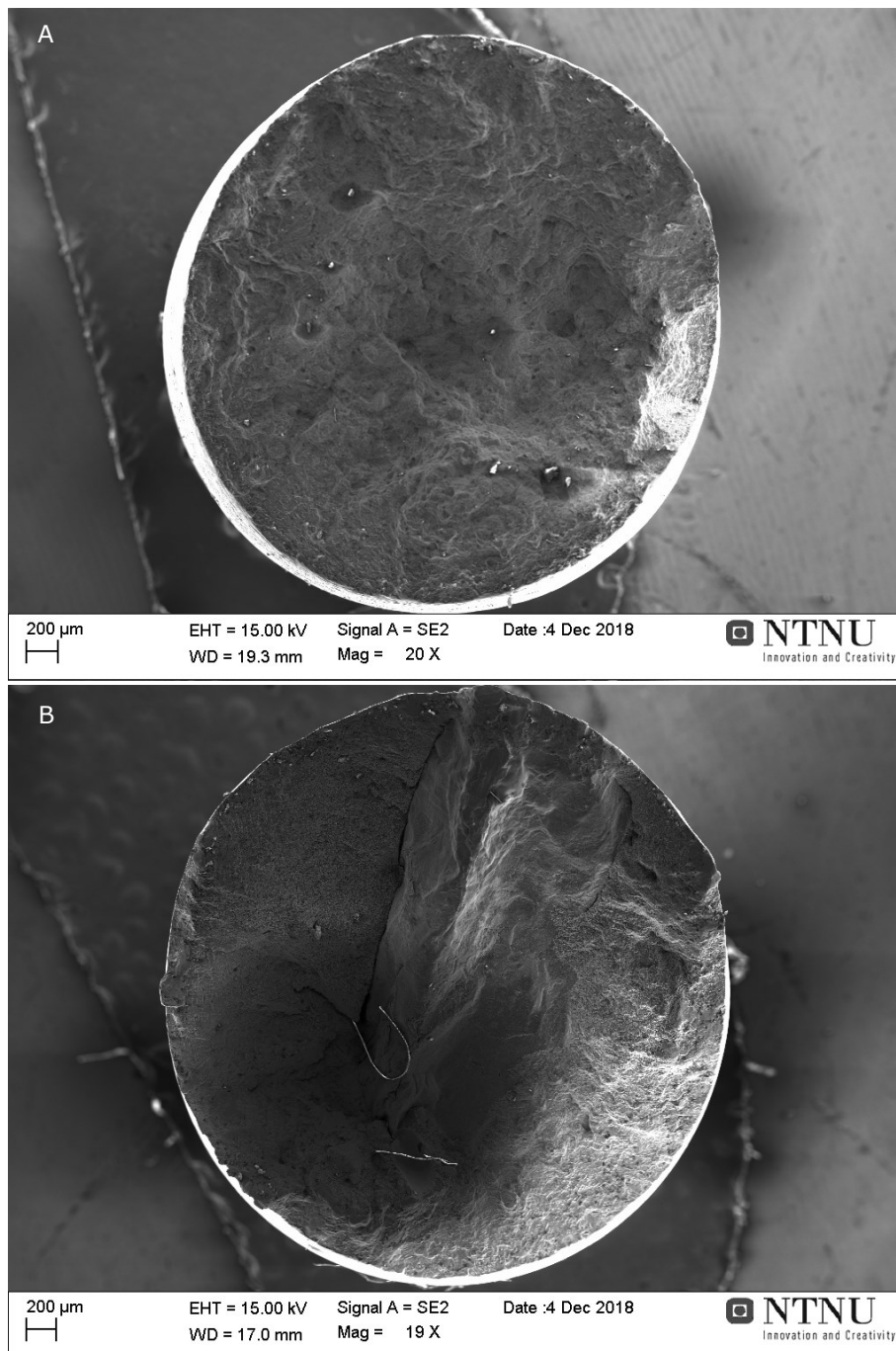
**Figure 4.4: Stress-strain curves for the tensile test specimens from the WAAM sample in three perpendicular direction: A) in x-direction, B) in y-direction and C) in z-direction. D) Curves for the permanent mold cast tensile specimens, P8 is rejected**

Figure 4.5 shows the fracture surfaces of P11 at the left and P8 at the right. The pieces are sliced from the tensile test specimens and glued to the fixture plate, ready for

examination in SEM. The dark field in P8 is pollution and served as a cleavage initiation point. Normally, a proper casting process would prevent this fracture type. The fracture angular is approximately  $45^\circ$  in not just one but several fracture planes, the fracture can have started as shear and ended as ductile in several localizations. Figure 4.6 A and B show the fractographies of P11 and P8 respectively. The fracture mechanisms are discussed in Chapter 5. More high magnification images can be found in the Appendix.



**Figure 4.5: Fracture surfaces of the permanent mold cast tensile specimens P11 (left) and P8 (right). Sliced from tensile test specimens and glued to the fixture plate for SEM. The black area in P8 (right) is pollution and oxide film.**



**Figure 4.6: Fractographies of the permanent mold cast tensile specimens. A) P11 and B) P8 (SEM, 200 µm)**

The microhardness test result for the WAAM specimen M are measured to minimum 61.0 HV<sub>0.1</sub> and maximum 80.9 HV<sub>0.1</sub>. For the castings P14 and S3 the results are minimum 50.0 and 42.0 HV<sub>0.1</sub>, and maximum 76.0 and 64.0 HV<sub>0.1</sub>, respectively. The average microhardness results included standard deviation are schematic illustrated in Figure 4.7. P14 and S3 are sliced into three parts where the slice -A represents the narrow end of the specimen, slice -B the middle part and slice -C the top end.

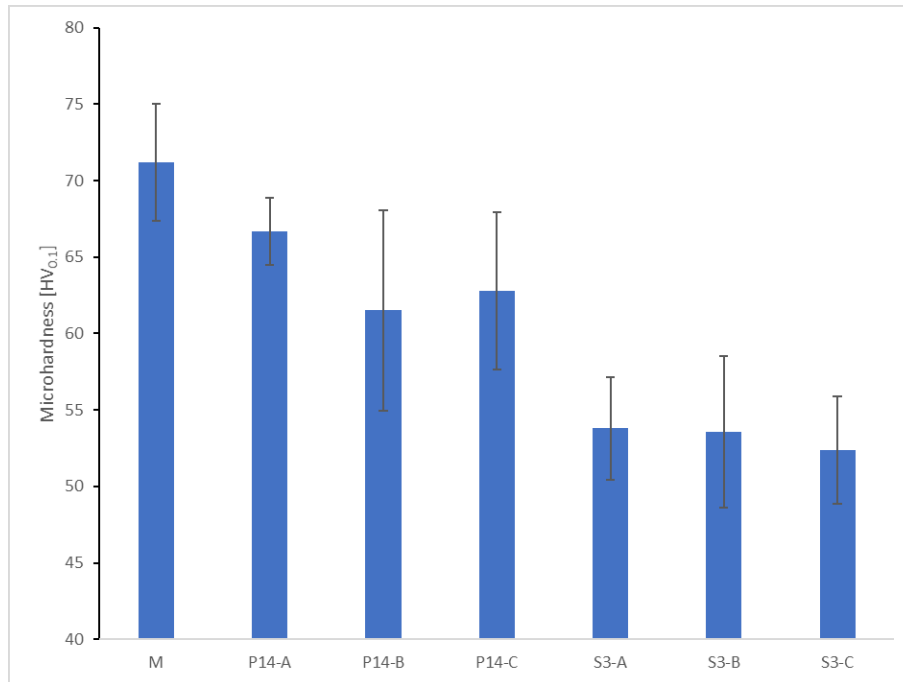


**Figure 4.7: Microhardness results. Carried out on the WAAM specimen M, the permanent mold casting P14 and the sand mold casting S3. The letters -A, -B and -C represent the sliced parts of P14 and S3 from the narrowed end to the top end.**

## 4.2 Microstructural Properties

The pore analysis results are shown in Figure 4.8. The analysis is based on images captured in LOM. The sand mold casting S3 had higher porosity level than the others, especially at the edges. The WAAM specimen M was sliced out from the center of the WAAM sample and had porosity level around 0.1%. The WAAM sample had also higher porosity along the edges. The porosity level data can be found in the Appendix.

Another study in pieces from the permanent mold casting P14 and of the sand mold casting S3 is carried out in SEM to examine and identify the pore types, see Figure 4.9 and Figure 4.10. Note that the pieces used for SEM are the mirrored cross-sections in the middle part of the specimens (P14-B and S3-B), hence the surfaces of the pieces are not in the center, but approximately 5 mm from the edges. Both gas pores and solidification shrinkage pores can be observed.

The dimensions of the riser were based on available components in the SINTEF workshop. The calculation by Chvorinov's rule and the equations (4) and (5) resulted in solidification time 0.29 s in the permanent mold, 60 s in the sand mold and 0.78 s in the riser. The mold constants B are calculated to 1459 s/m<sup>2</sup>, 299109 s/m<sup>2</sup> and 13995 s/m<sup>2</sup> for the permanent mold, the sand mold and the riser respectively. The calculation enclosed in the Appendix is based on the enclosed data sheets from other suppliers and should be used as an example only as the time results are improbable.

However, the results above show that the sand mold design gives longer solidification time than the riser and this can explain the larger shrinkage for the sand mold castings. The permanent mold had shorter solidification time than the riser and the shrinkage is assumed to have been compensated in the permanent mold.

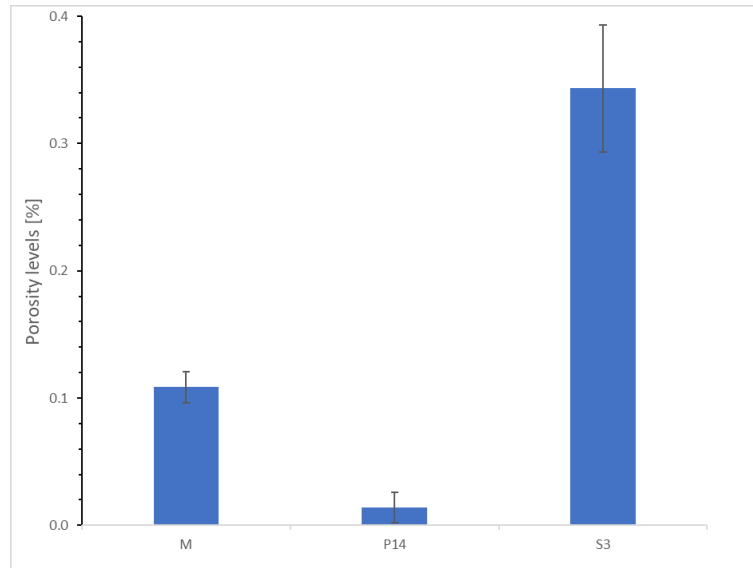


**Figure 4.8: Pore analysis results. Carried out on cross-sections of the WAAM specimens M, the permanent mold casting P14 and the sand mold casting S3.**

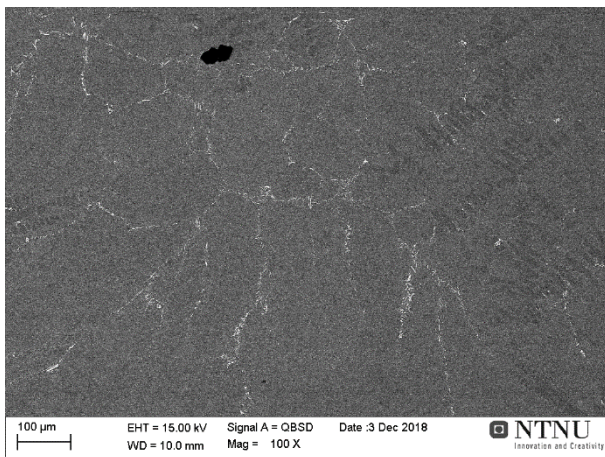


**Figure 4.9: Solidification shrinkage in permanent mold casting P14 (SEM, 100 µm)**

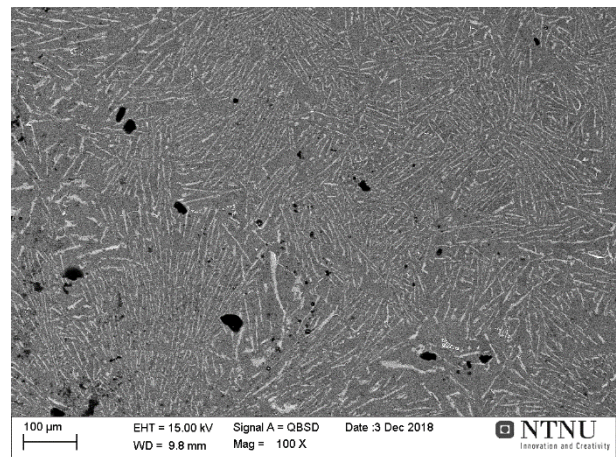


**Figure 4.10: Pores and solidification shrinkage in sand mold casting S3 (SEM, 100 µm)**

The SDAS in the WAAM specimen M are measured to be between 3 and 11 µm, see the box plots in Figure 4.11 and Figure 4.12 for equation (1) and (2) respectively. The SDAS are measured based on the LOM images in Figure 4.13. The measurement data can be found in the Appendix. Around ten measurements are registered in each image. Figure 4.14 shows eutectic microconstituent and partly dendrite formation in the WAAM specimen, captured in SEM.

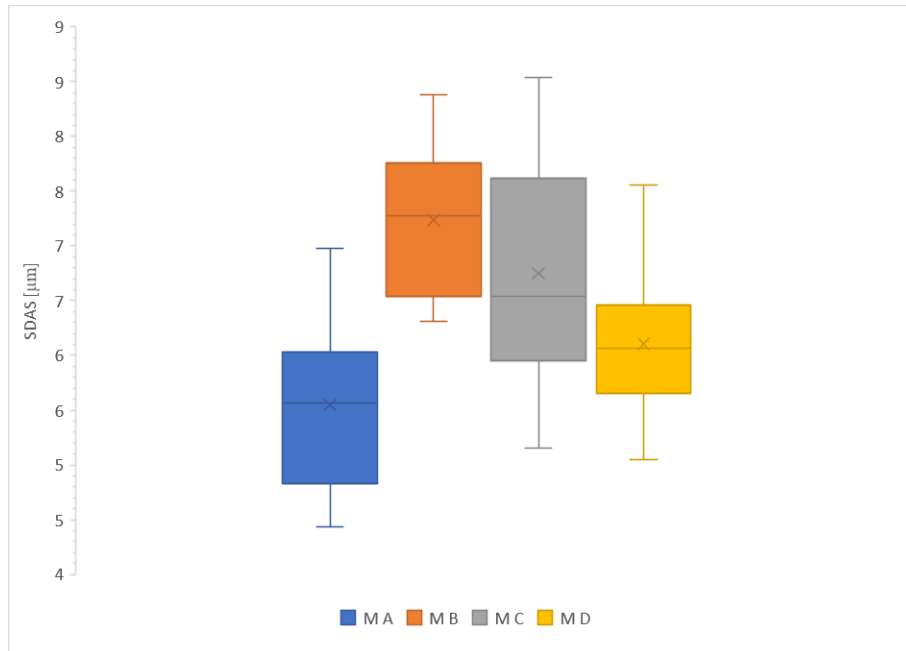


**Figure 4.11:** SDAS for the WAAM specimen M calculated with equation (1). The letters A, B, C and D represents measurements in Figure 4.16 A, B, C and D

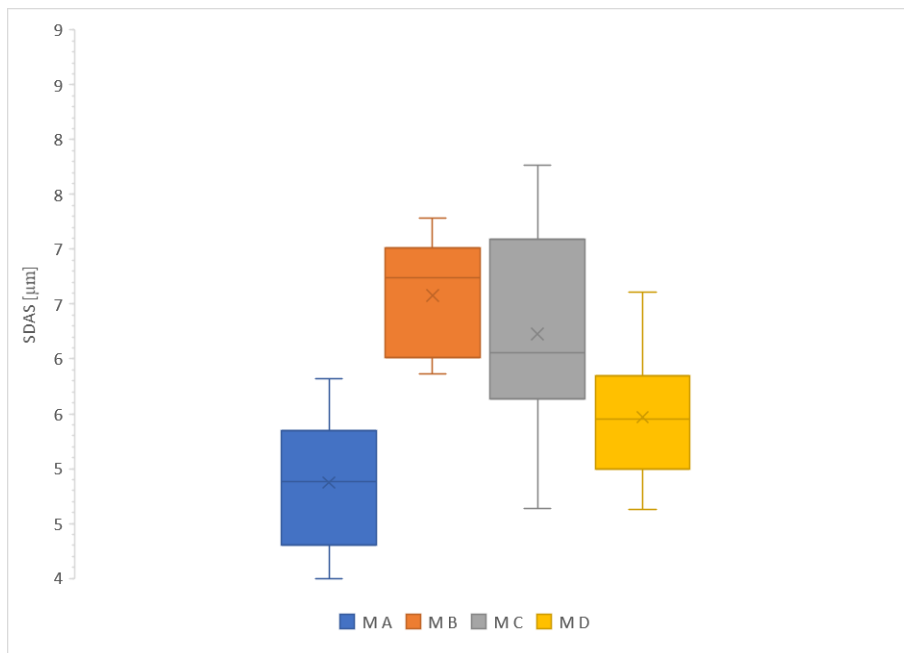


**Figure 4.12:** SDAS for the WAAM specimen M calculated with equation (2). The letters A, B, C and D represents measurements in Figure 4.16 A, B, C and D

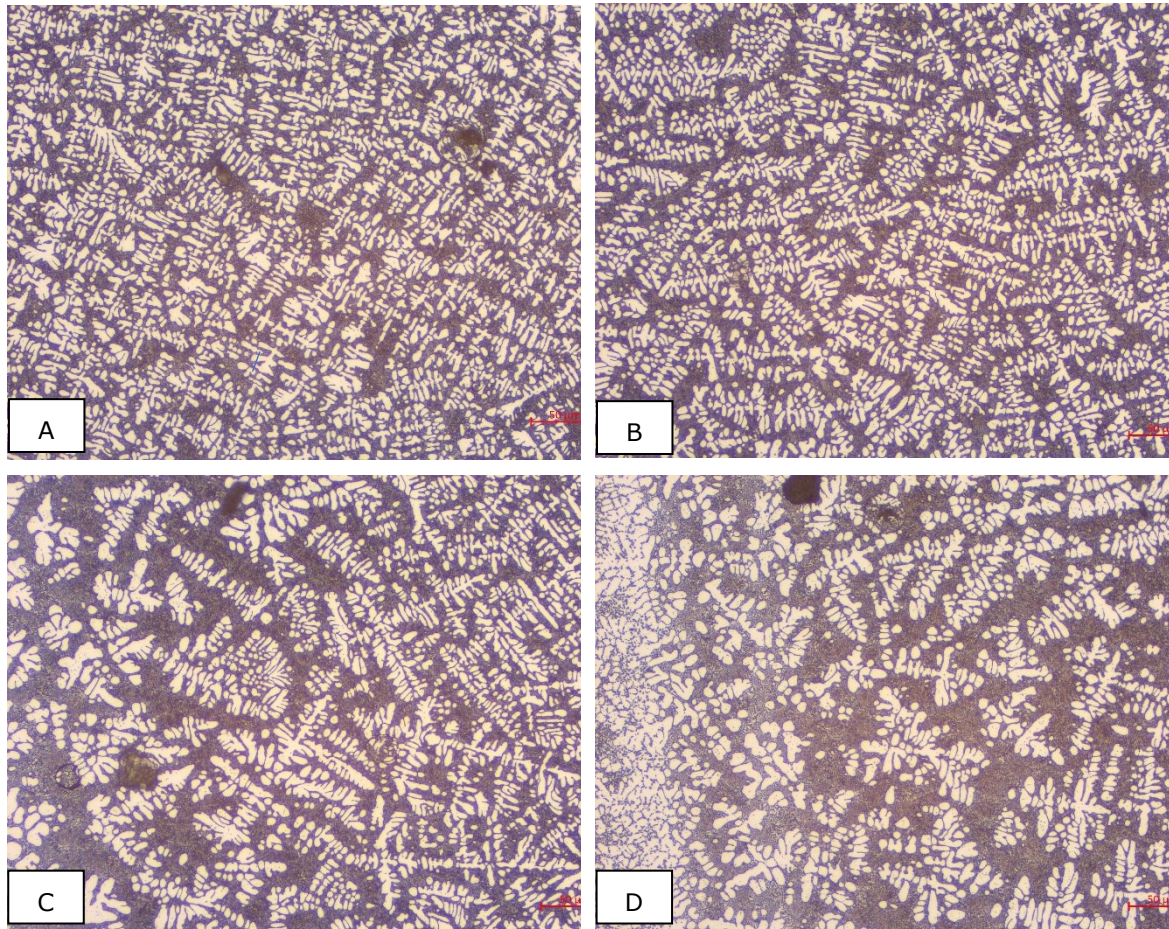


**Figure 4.13: Dendrite formation in the WAAM specimen M (LOM, 50 µm)**

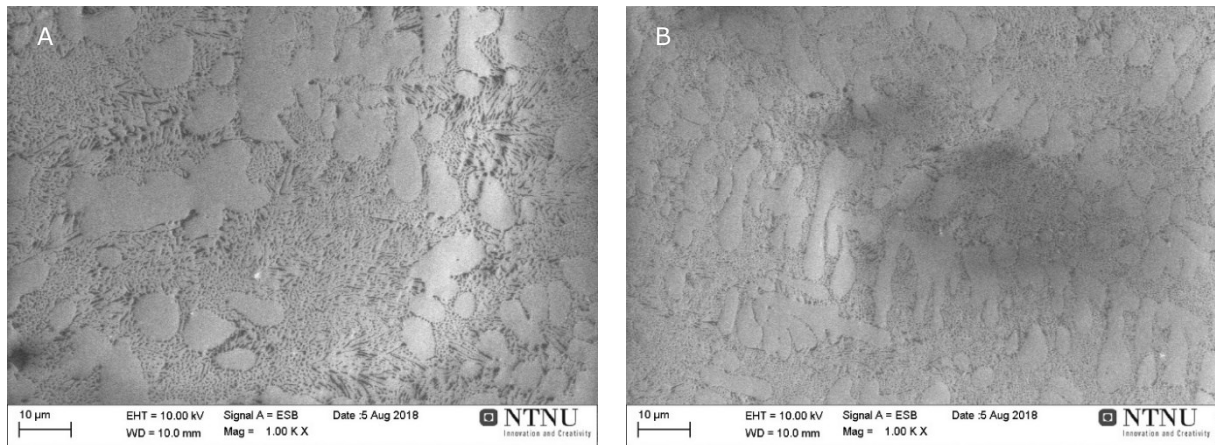


**Figure 4.14: Eutectic microconstituent in the WAAM sample (SEM, 10 µm). A) Coarse eutectic and B) fine eutectic structure**

The grain structures in the WAAM specimen M are revealed by EBSD and shown with the attached grain structure map in Figure 4.15. Unfortunately, the image quality is not sufficient for analysis and will not be profoundly discussed in this report. Still, we see a pattern in how the structure changes from equiaxed grains in the bead at the top to columnar grains by the bead edges.



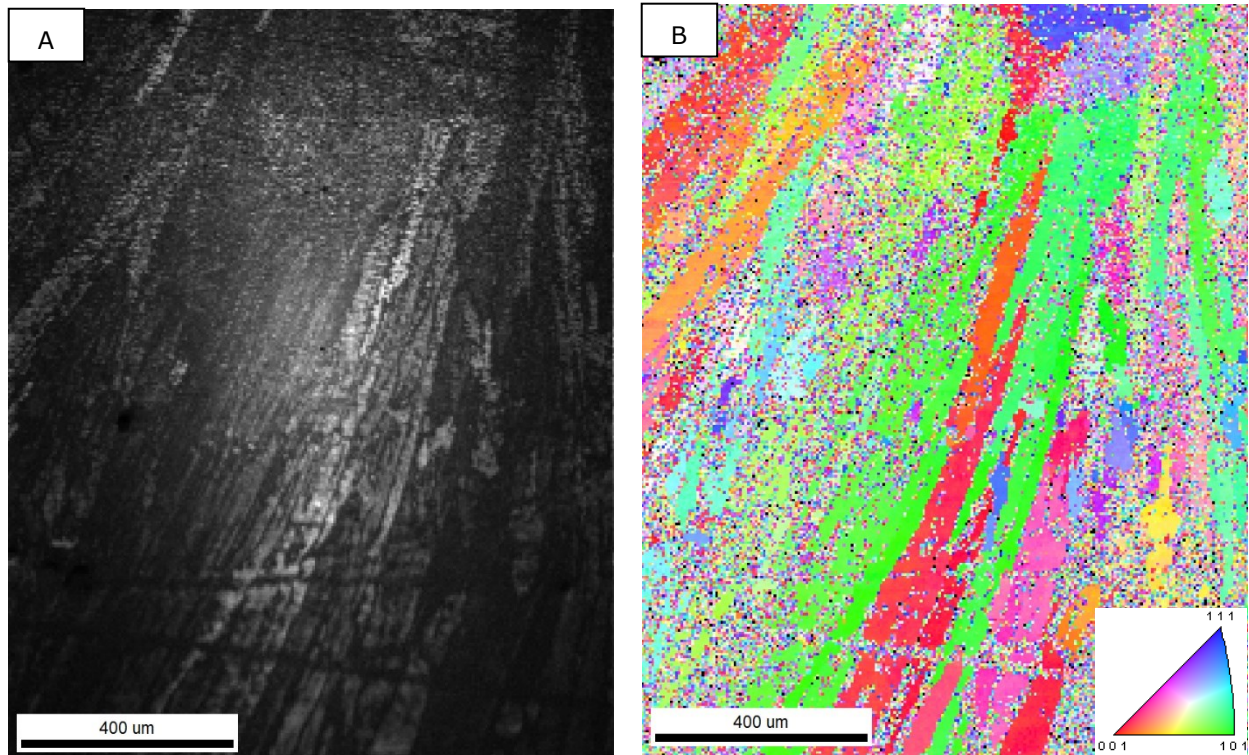


**Figure 4.15: EBSD images of A) the grain structure in the WAAM specimen M and B) the grain orientation with inverse pole figure. Due to poor image quality, the images will not be profoundly discussed in the report.**

For the castings the SDAS measurements have large variation and are measured to between 5 and 58  $\mu\text{m}$  for the permanent mold casting P13 and between 9 and 43  $\mu\text{m}$  for the sand mold casting S2, see the box plots in Figure 4.16 and Figure 4.17. The SDAS measurements are based on the LOM images as shown in Figure 4.18 and Figure 4.19 for equation (1) and (2) respectively. The measuring data can be found in the Appendix.

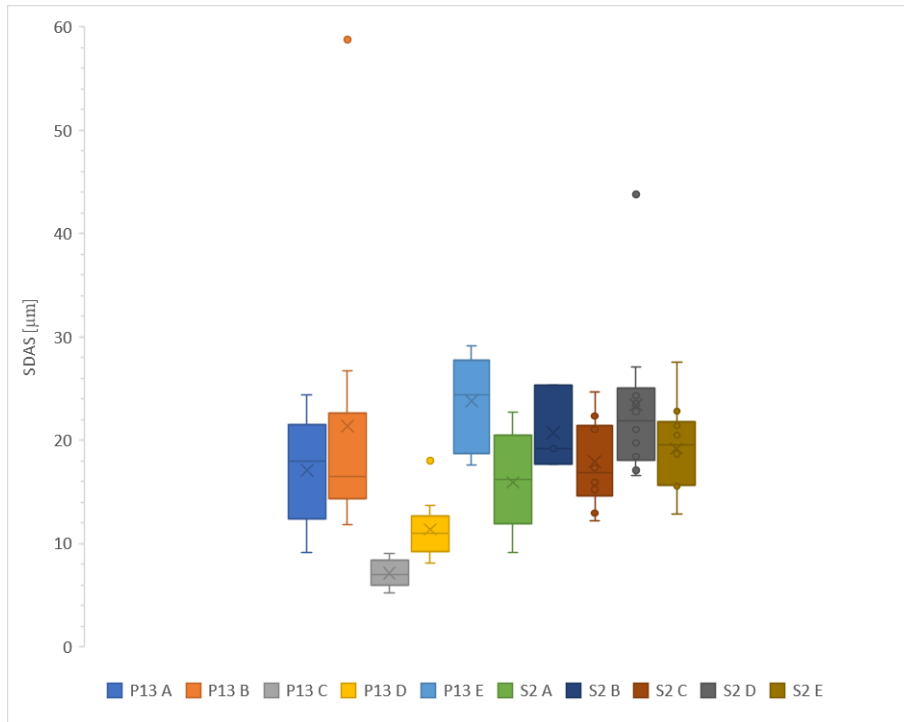


**Figure 4.16: SDAS for permanent mold casting P13 and sand mold casting S2 calculated with equation (1). The letters A, B, C, D and E represents measurements in Figure 4.18 A-E and Figure 4.19 A-E**

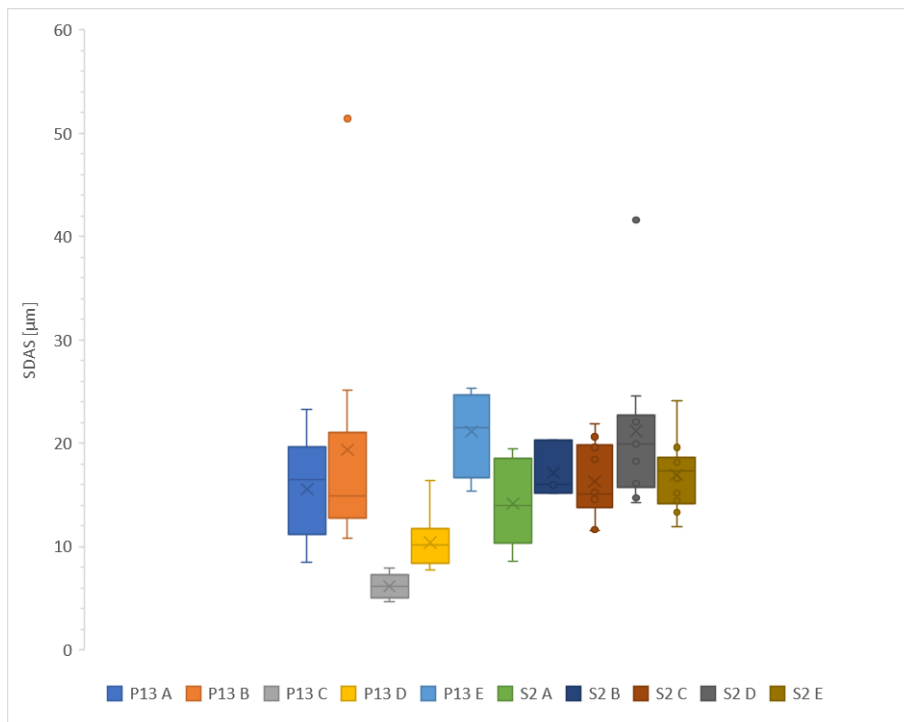


**Figure 4.17: SDAS for permanent mold casting P13 and sand mold casting S2 calculated with equation (2). The letters A, B, C, D and E represents measurements in Figure 4.18 A-E and Figure 4.19 A-E**

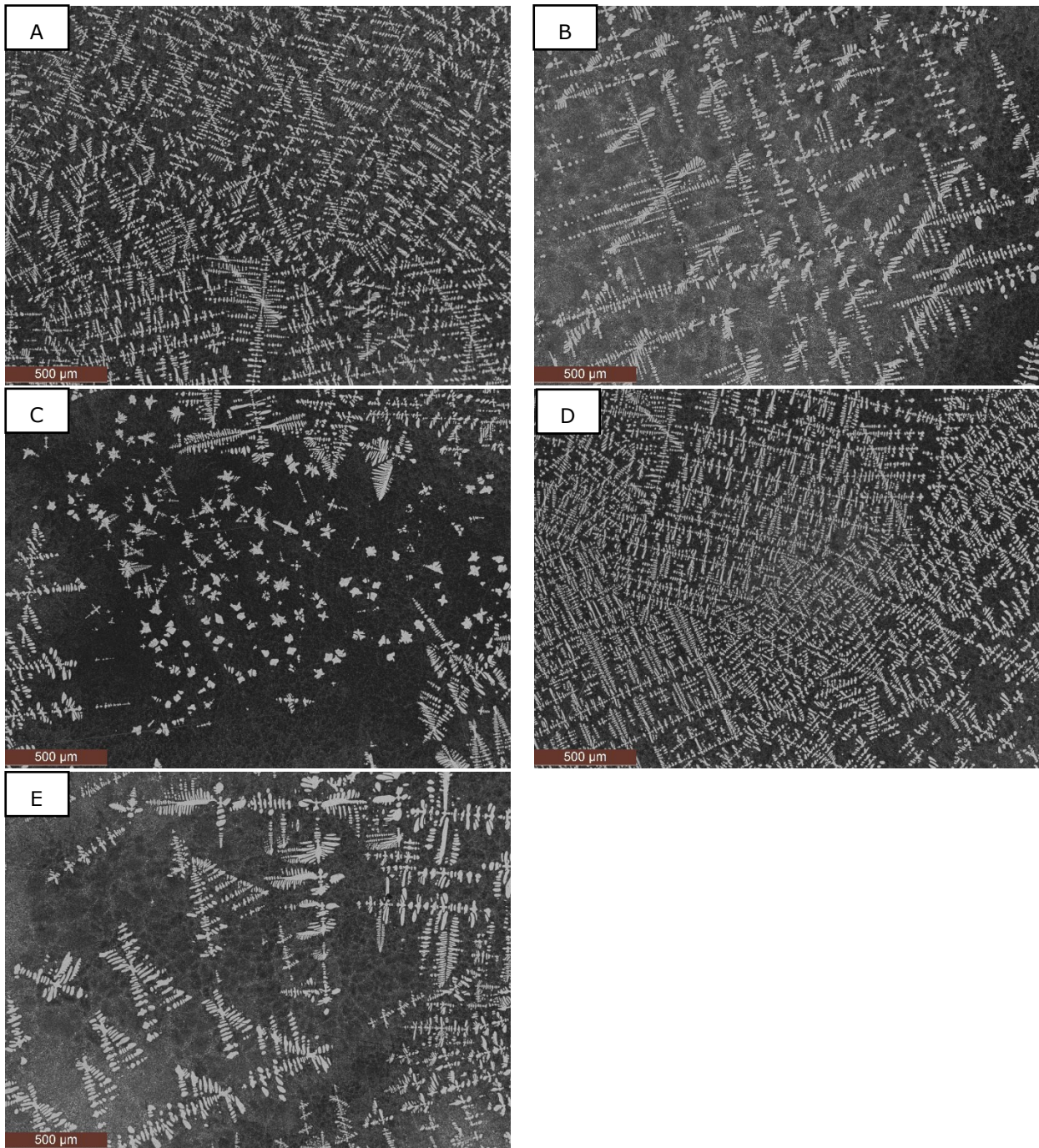


**Figure 4.18: Microstructures in permanent mold casting P13 used as basis for SDAS measurements quoted in Figure 4.16 and Figure 4.17**

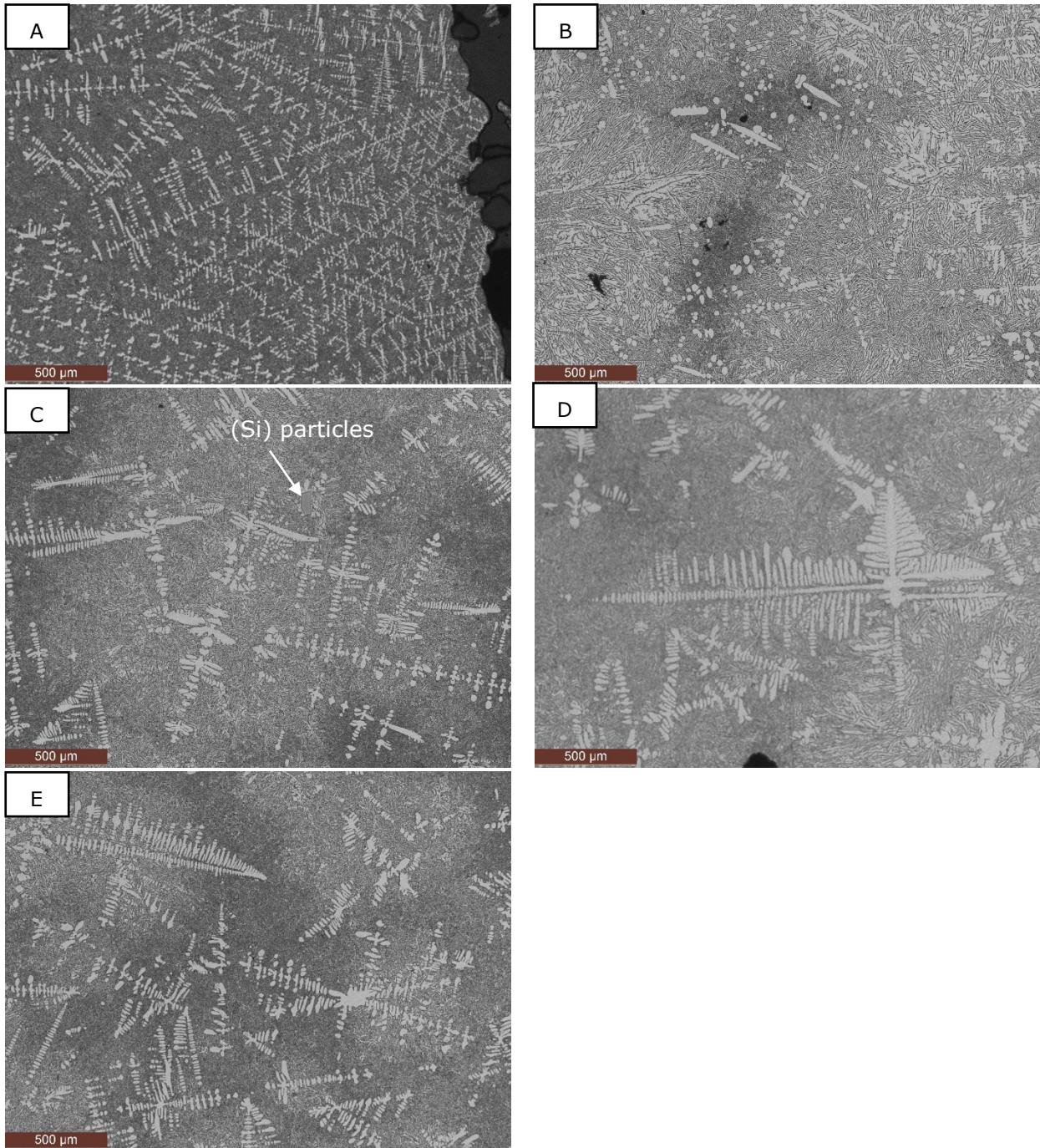


**Figure 4.19: Microstructures in sand mold casting S2 used as basis for SDAS measurements quoted in Figure 4.16 and Figure 4.17. C) Primary (Si) particles were to some extent present, see arrow**

## 5 Discussion

### 5.1 Fracture Mechanisms

The pollution in the permanent mold casting P8 may have caused the cleavage fracture marked with an arrow to the right in Figure 5.1. A clear interface between the Al-12Si alloy and the film can also be observed, and it may be the cleavage fracture, see the left arrow in Figure 5.1. We tried to identify the pollutions in the SEM but were not able to observe any accumulation but aluminum, oxygen and nitrogen. The theory is that the pollution is fibers from the aluminum silicate fiber bush, that dissolved and left oxide film. That can explain the dark field in Figure 4.5 and why any accumulation could not be observed.

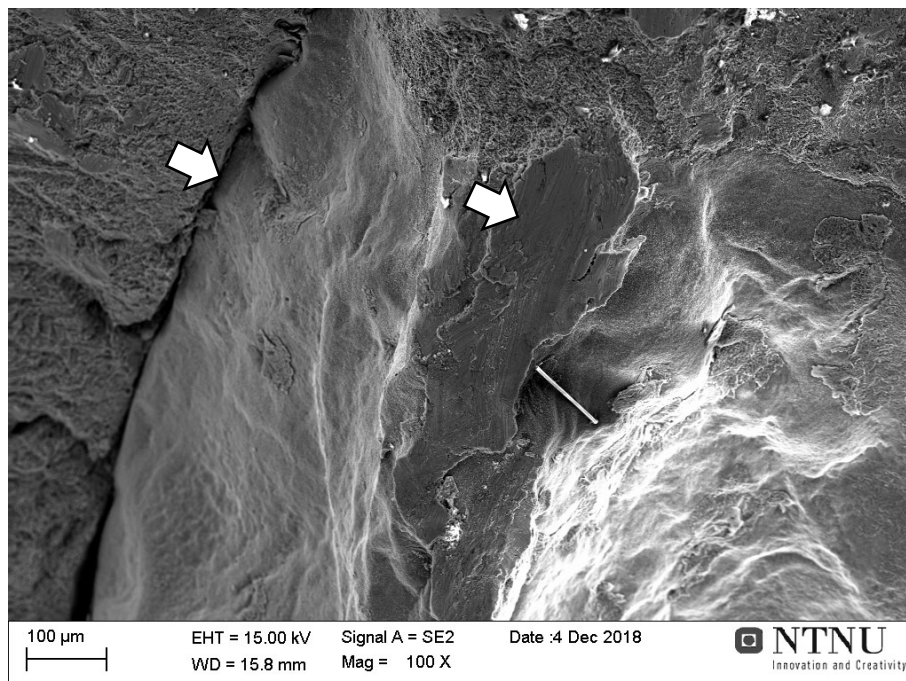


**Figure 5.1: Cleavage fracture in permanent mold casting P8. The right arrow marks the cleavage fracture and the left arrow marks the interface between the Al-12Si alloy and the pollution (SEM, 100 μm)**

The fractographies in Figure 5.2 shows the initial fracture in permanent mold casting P11, i.e. intergranular fractures can be observed and are marked with an arrow and enlarged image. There are also dimples from the plastic deformation prior to fracture, as marked in Figure 5.3. Dendritic traces are observed in Figure 5.4, it indicates inclusions or other weaknesses within the dendritic lobes. The final fracture is shown in Figure 5.5, with visible pore and precipitated brittle (Si) particles. A few (Si) particles were also observed in the polished microstructures of P13 and P14, see Figure 5.6 A and B.

Further microstructural analysis should be carried out on several cross-sections of the specimens and in the fracture surfaces to analyze the phases around the precipitated (Si) particles and the dendrites.

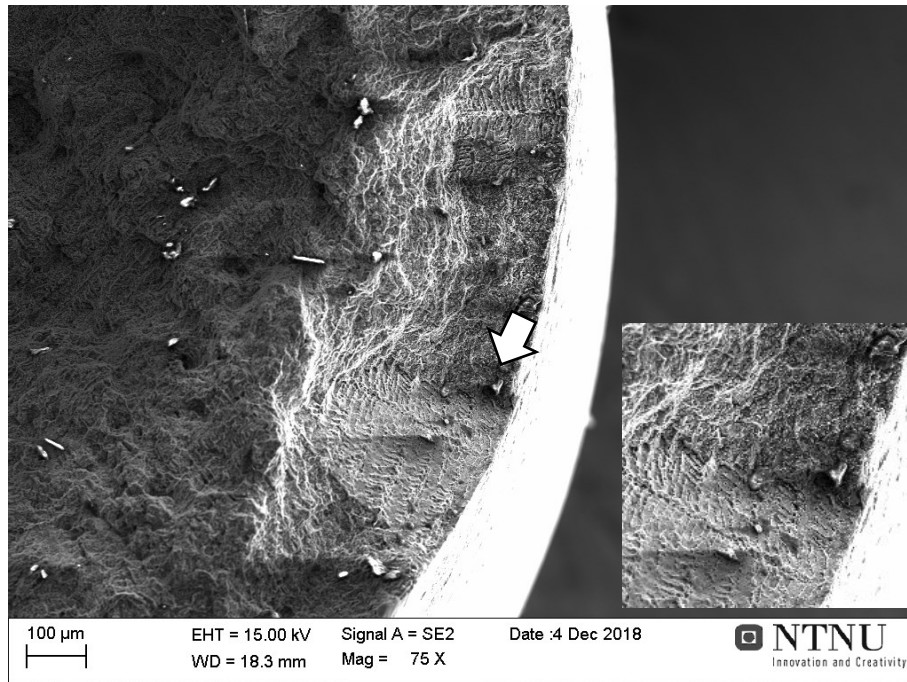


**Figure 5.2: Intergranular fractures in permanent mold casting P11 (SEM, 100 μm). Enlarged image in right corner represent the area indicated by the white arrow (no scale). It is believed the fracture initiated at this site as intergranular fracture**

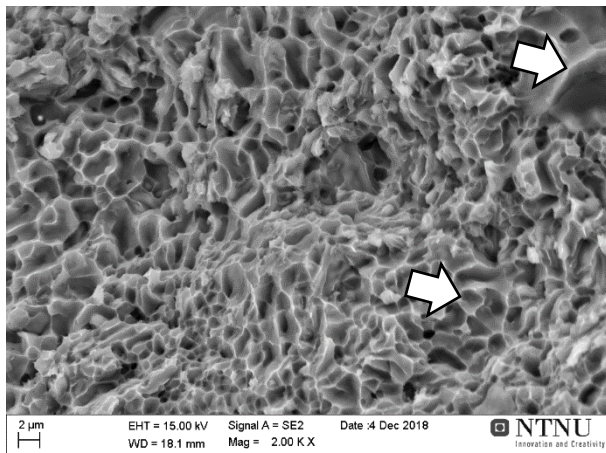


**Figure 5.3: Dimples (lower arrow) and intergranular fractures (upper arrow) in permanent mold casting P11 (SEM, 2 μm)**

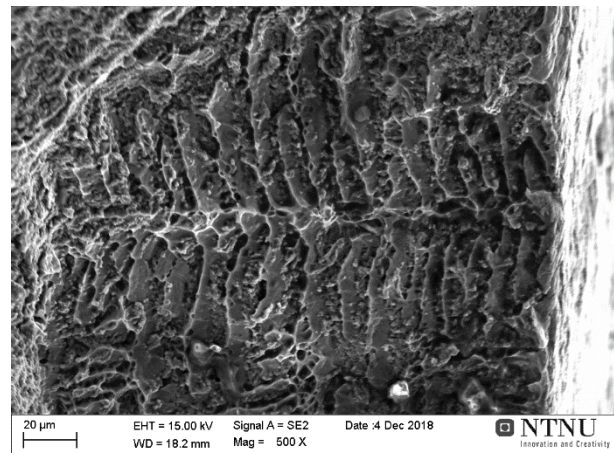


**Figure 5.4: Dendritic traces in permanent mold casting P11 (SEM, 20 μm)**

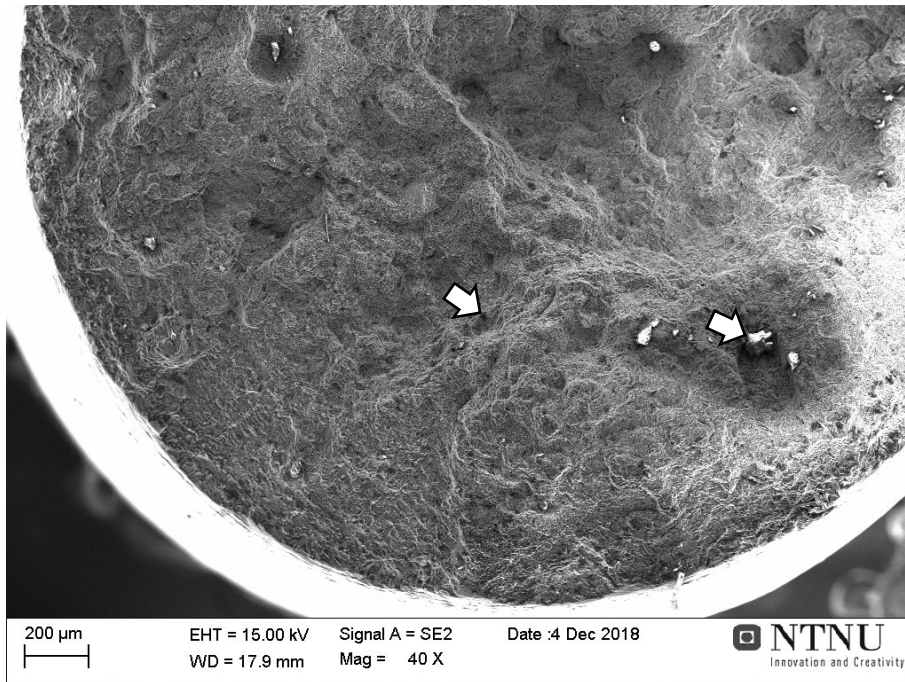


**Figure 5.5: (Si) particles and pores in permanent mold casting P11. The bright elements are (Si) particles and the dark fields are pores. (SEM, 100  $\mu\text{m}$ )**

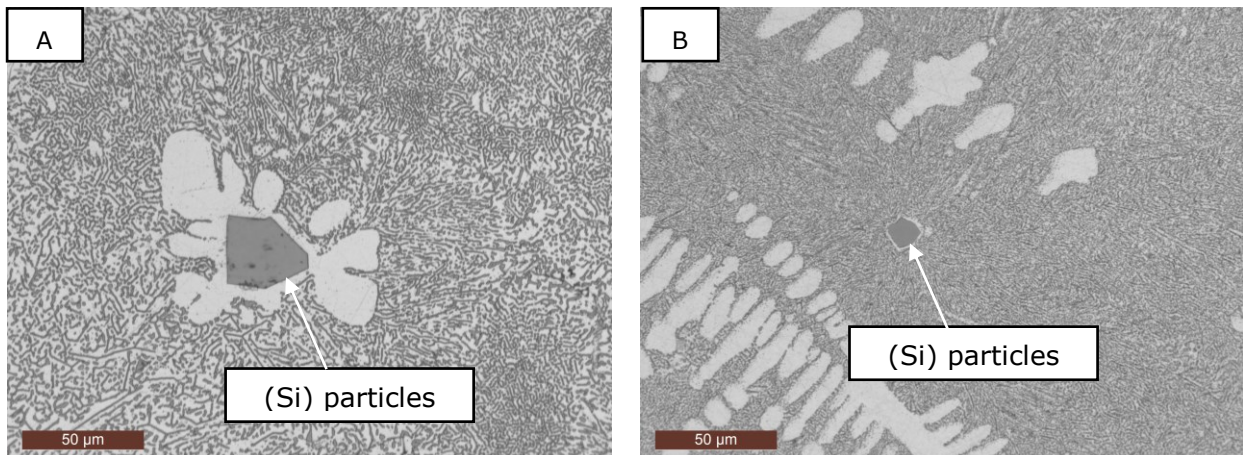


**Figure 5.6: (Si) particles in the permanent mold castings A) P13 and B) P14**

## 5.2 Porosity Levels

The porosity analysis shows that there are gas and shrinkage pores in both permanent mold and sand mold castings, especially the latter. The shrinkage pores occur when the liquid shrinks during solidification and are shown in Figure 5.7. The pore nucleation and coalescence can also have been the site for crack propagation and intergranular fracture.

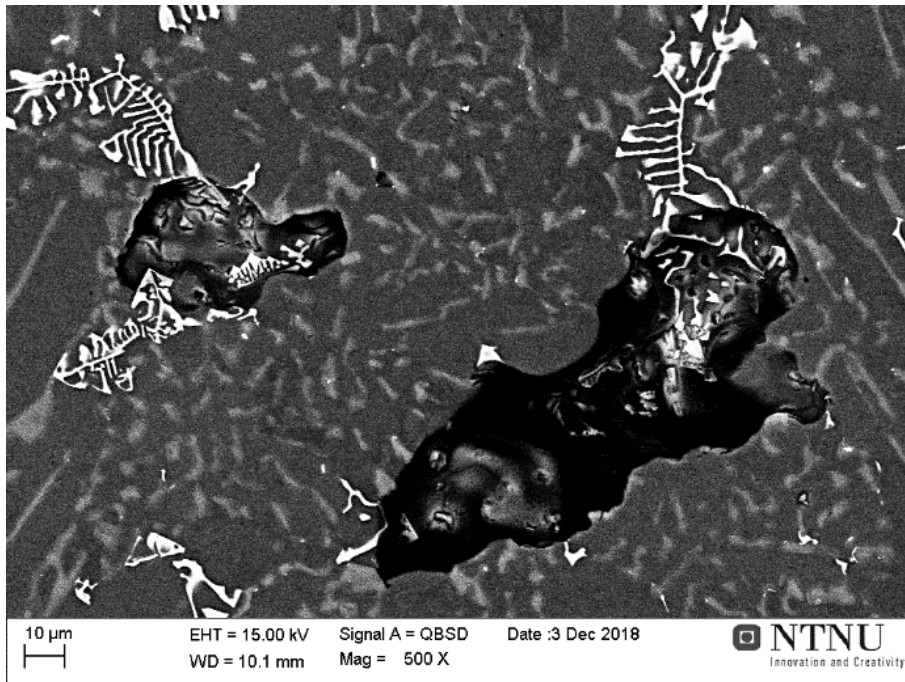


**Figure 5.7: Solidification shrinkage in sand mold casting S3 (SEM, 10  $\mu\text{m}$ )**

### 5.3 Microhardness

Figure 5.8 shows the microhardness distribution in the WAAM specimen (AA 4047) and lines up the bead edges. The measurement data are enclosed in the Appendix. The microhardness values tend to be higher within the beads and lower between the beads. The microstructural analysis revealed a coarser dendritic structure in the interfaces between the adjacent beads, explaining the decrease in hardness at the sites (Figure 4.7). See Section 2.1, the fusion zone (FZ) has equiaxed grains, the partially melted zone (PMZ) columnar grains and the heat-affected zone HAZ small and fine grains.

FZ can be observed within the beads and has higher level of hardness, while PMZ can be found in the interfaces and has lower hardness, see Figure 5.8. HAZ is the underlying layers reheated by the next depositing layers and has also high hardness due to the introduction of recrystallization and grain structure alteration.



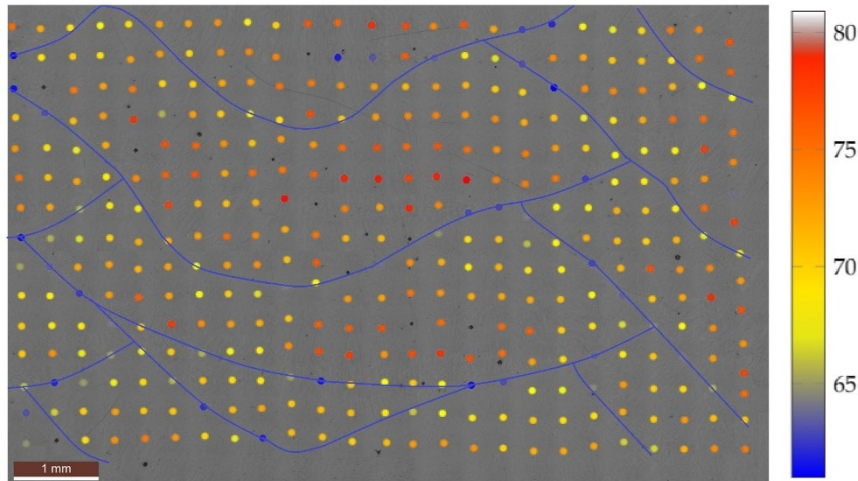


**Figure 5.8: Microhardness distribution in the WAAM specimen M. Section cut in the YZ-plane. The microhardness is low at the bead edges, indicated by blue lines [11]**

#### 5.4 Secondary Dendrite Arm Spacing (SDAS) and Cooling Rate

SDAS in the WAAM specimen M, the permanent mold casting P13 and the sand mold casting S2 are collected in the box plots in Figure 5.9 and Figure 5.10, calculated with the equations (1) and (2) respectively. The measurement data are enclosed in the Appendix. The total dendrite length is measured from upper to lower arm in accordance with the method D (see Section 2.3) and then the SDAS is calculated using equation (1). The SDAS is also calculated with equation (2) to compare with the effect of subtracting the denominator with 1 in the study by Haselhuhn et al. [2]. Equation (3) gives the associated cooling rates as shown in Figure 5.11 and Figure 5.12.

The variation in the SDAS measurements are scattered, the points representing the highest observed values and the crosses representing the average values. The box plots represent the measurement dispersion and skewness, that has a significant influence for the cooling rates. The range of cooling rate cover from  $0.6$  to  $2118 \text{ K s}^{-1}$  for the specimens M, P13 and S2.

When considering the average SDAS only, the average SDAS for equation (1) are  $6.4 \mu\text{m}$ ,  $16.1 \mu\text{m}$  and  $19.2 \mu\text{m}$  for M, P13 and S2, and for equation (2)  $5.8 \mu\text{m}$ ,  $14.5 \mu\text{m}$  and  $17.1 \mu\text{m}$  respectively. The associated cooling rates for equation (1) are  $591 \text{ K s}^{-1}$ ,  $133 \text{ K s}^{-1}$  and  $30 \text{ K s}^{-1}$ , and for equation (2) the rates are  $813 \text{ K s}^{-1}$ ,  $194 \text{ K s}^{-1}$  and  $41 \text{ K s}^{-1}$  respectively.

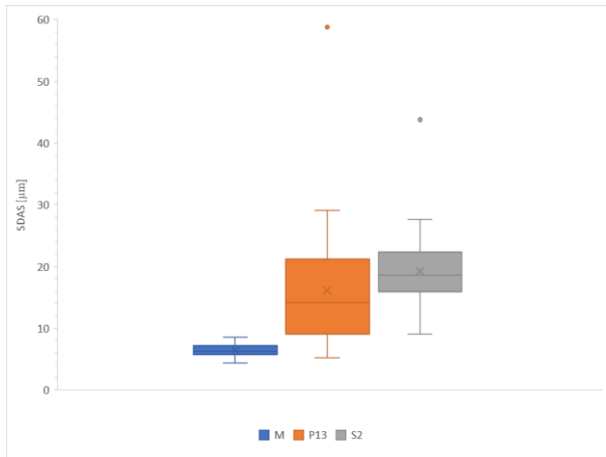


**Figure 5.9: SDAS calculated with equation (1) for the WAAM specimen M, the permanent mold casting P13 and the sand mold casting S2**

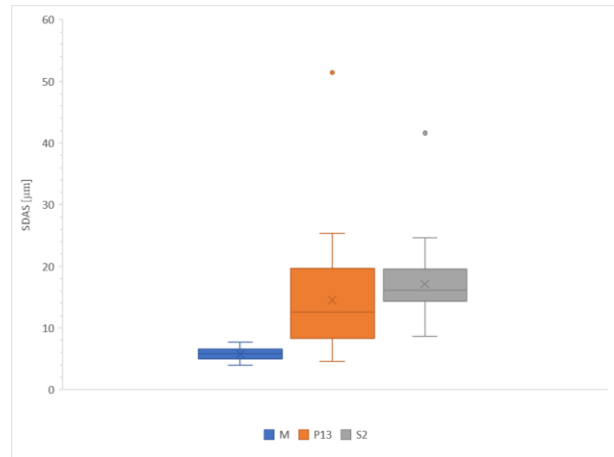


**Figure 5.10: SDAS calculated with equation (2) for the WAAM specimen M, the permanent mold casting P13 and the sand mold casting S2**

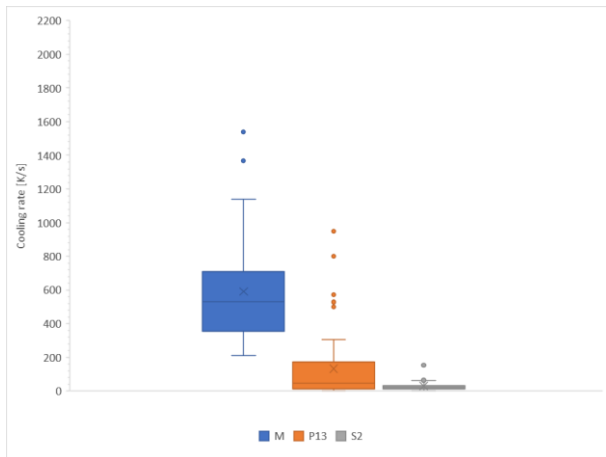


**Figure 5.11: Cooling rates based on equations (1) and (3) for the WAAM specimen M, the permanent mold casting P13 and the sand mold casting S2**

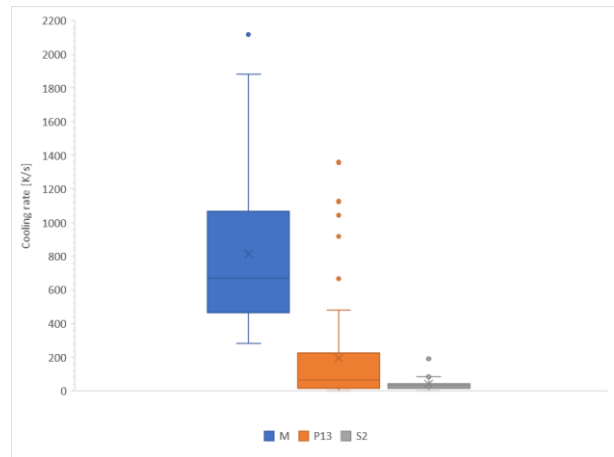


**Figure 5.12: Cooling rates based on equations (2) and (3) for the WAAM specimen M, the permanent mold casting P13 and the sand mold casting S2**

In light of the large variation, we decided to perform another examination in SEM to verify the SDAS measurements. Due to time and resource limitation, only few ranges of the WAAM specimen M, the permanent mold casting P14 and the sand mold casting S3 are studied in SEM: The WAAM specimen is studied in the fusion zone (FZ) in the bead, partially melted zone (PMZ) between the beads and heat-affected zone (HAZ) in the adjacent bead, see Figure 5.13, Figure 5.14 and Figure 5.15. The permanent mold casting P14 and the sand mold casting S3 are studied in the middle parts, see Figure 5.16 and Figure 5.17. New SDAS measurements based on the SEM images are box plotted in Figure 5.18 and Figure 5.19 for the equations (1) and (2) respectively. The measurement data are enclosed in the Appendix.

The SDAS in M tend to be smaller in FZ than in PMZ and are more closed to the SDAS in P14. The dendrites in HAZ are small and entangled (between 2 and 4 µm), hard to

measure and resulted into large outcomes in the cooling rates ( $3390 \text{ Ks}^{-1}$  and  $6666 \text{ Ks}^{-1}$ ). No significant impact of the large thickness is observed regarding the cooling speed or the microstructure in the WAAM sample.

The average SDAS calculated with equations (1) are  $6.0 \mu\text{m}$ ,  $11.3 \mu\text{m}$  and  $21.5 \mu\text{m}$  for M, P14 and S3 respectively. The corresponding average cooling rates are  $1018 \text{ Ks}^{-1}$ ,  $116.9 \text{ Ks}^{-1}$  and  $14.5 \text{ Ks}^{-1}$  respectively. Calculated with equation (2), the average SDAS decreased to  $5.3 \mu\text{m}$ ,  $9.2 \mu\text{m}$  and  $18.2 \mu\text{m}$  respectively, and the corresponding cooling rates increased to  $1695 \text{ Ks}^{-1}$ ,  $200 \text{ Ks}^{-1}$  and  $26 \text{ Ks}^{-1}$  respectively. The latter box plots without the HAZ measurements are the most suitable.

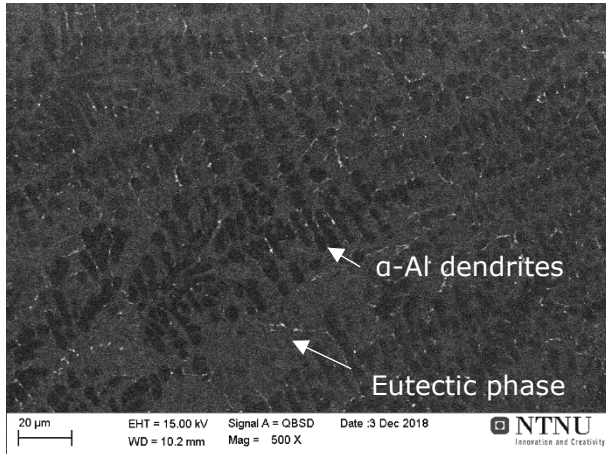


**Figure 5.13: Dendrites in FZ in the WAAM specimen M (SEM, 20  $\mu\text{m}$ )**

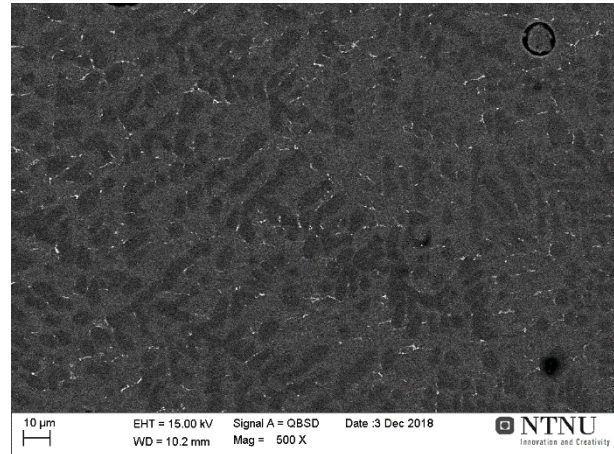


**Figure 5.14: Dendrites in PMZ in the WAAM specimen M (SEM, 10  $\mu\text{m}$ )**

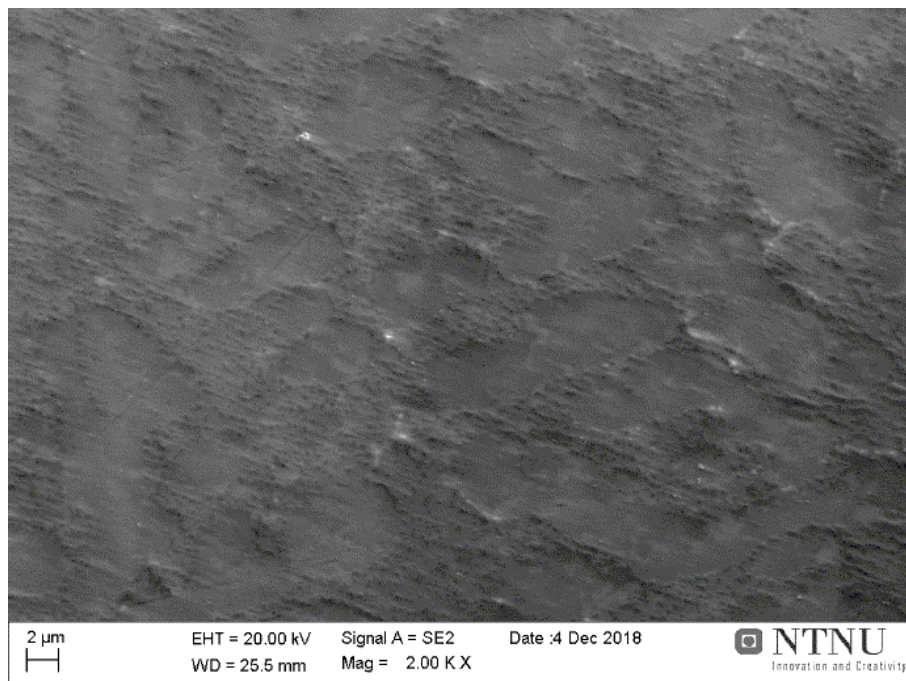


**Figure 5.15: Dendrites in HAZ in the WAAM specimen M (SEM, 2  $\mu\text{m}$ ). The dendrites are small and entangled (between 2 and 4  $\mu\text{m}$ ), hard to measure and gives large calculated cooling rates**

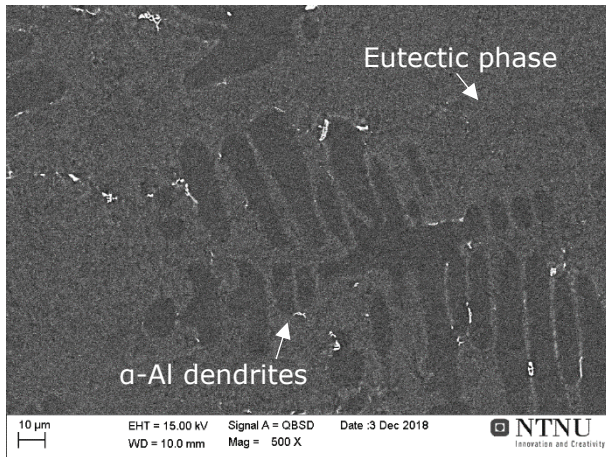


**Figure 5.16: Dendrites in the middle part of the permanent mold casting P14 (SEM, 10 μm)**

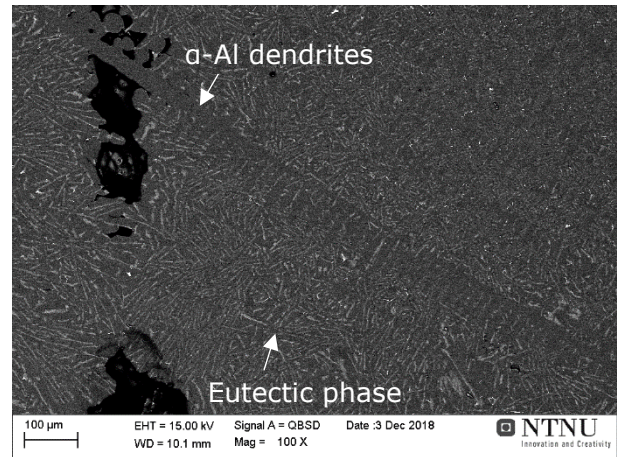


**Figure 5.17: Dendrites in the middle part of the sand mold casting S3 (SEM, 100 μm)**

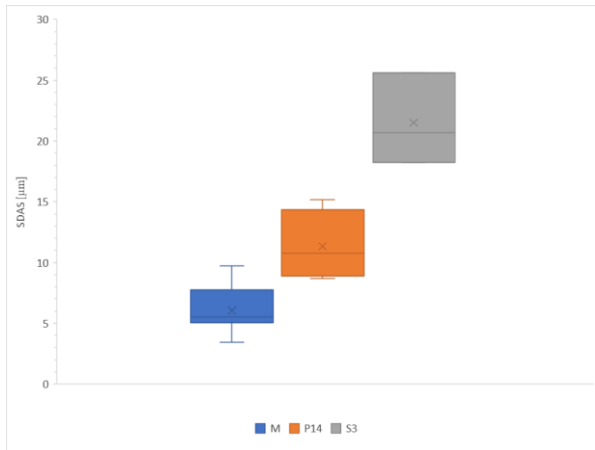


**Figure 5.18: Based on SEM images, SDAS calculated with equation (1) for the WAAM specimen M, the permanent mold casting P14 and the sand mold casting S3**

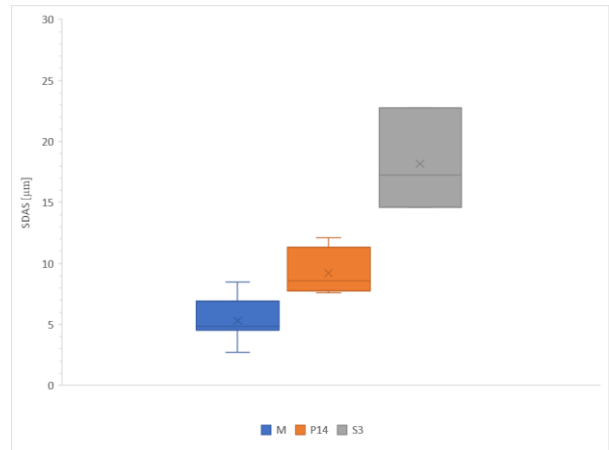


**Figure 5.19: Based on SEM images, SDAS calculated with equation (2) for the WAAM specimen M, the permanent mold casting P14 and the sand mold casting S3**

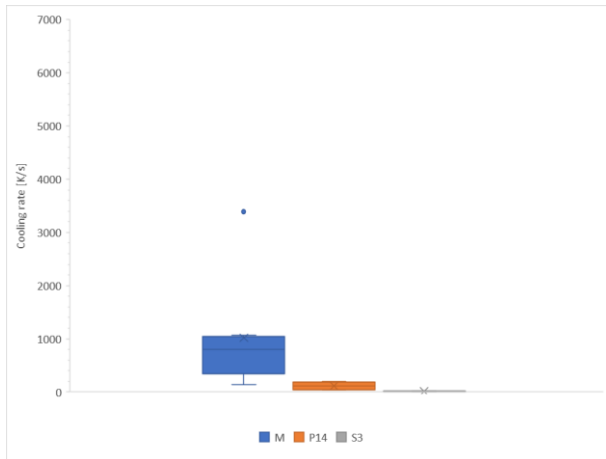


**Figure 5.20:** Based on SEM images, cooling rate calculated with equations (1) and (3) for the WAAM specimen M, the permanent mold casting P14 and the sand mold casting S3

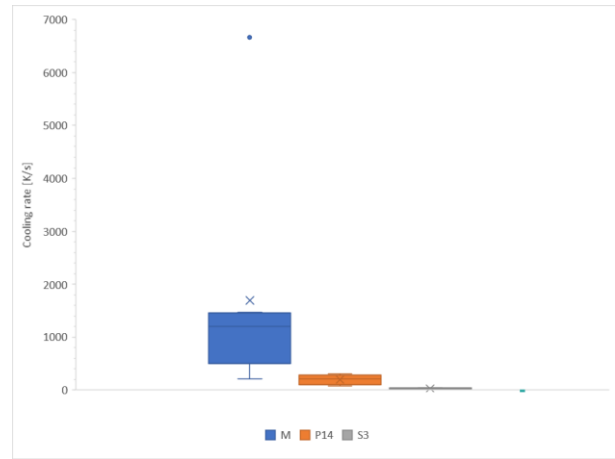


**Figure 5.21:** Based on SEM images, cooling rate calculated with equations (2) and (3) for the WAAM specimen M, the permanent mold casting P14 and the sand mold casting S3

The dendrites in the HAZ are of a distinctive characteristic and should not represent the SDAS and the cooling rate of the whole WAAM sample. To get a better picture of the SDAS and the cooling rates, the HAZ are rejected from the box plots for SDAS and cooling rates in Figure 5.22, Figure 5.23, Figure 5.24 and Figure 5.25. The average SDAS for M calculated with equations (1) and (2) increases to 6.4 and 5.7 respectively. The belonging cooling rate decreases to  $679 \text{ Ks}^{-1}$  and  $985 \text{ Ks}^{-1}$  respectively.

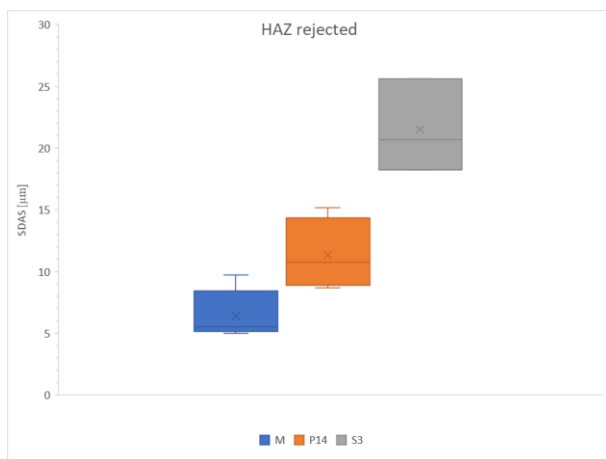


**Figure 5.22:** HAZ rejected from the SDAS, calculated with equation (1) for the WAAM specimen M, the permanent mold casting P14 and the sand mold casting S3

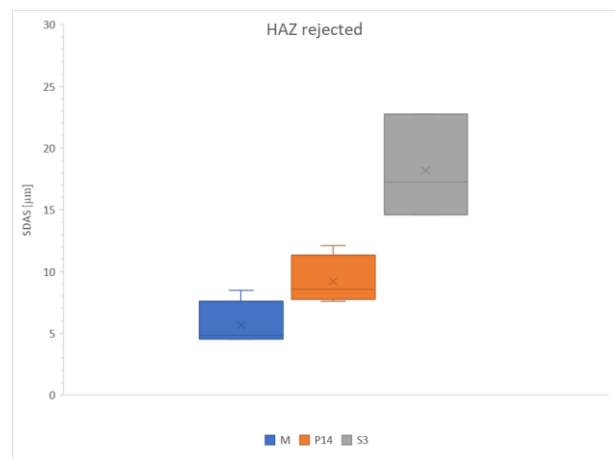


**Figure 5.23:** HAZ rejected from the SDAS, calculated with equation (2) for the WAAM specimen M, the permanent mold casting P14 and the sand mold casting S3

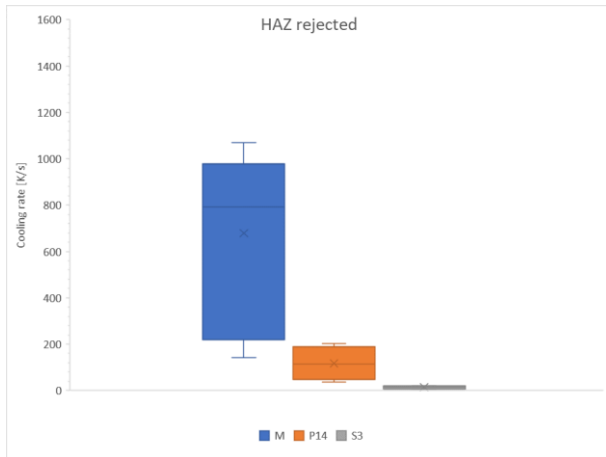


**Figure 5.24: HAZ rejected from the cooling rate, calculated with equation (1) for the WAAM specimen M, the permanent mold casting P14 and the sand mold casting S3**

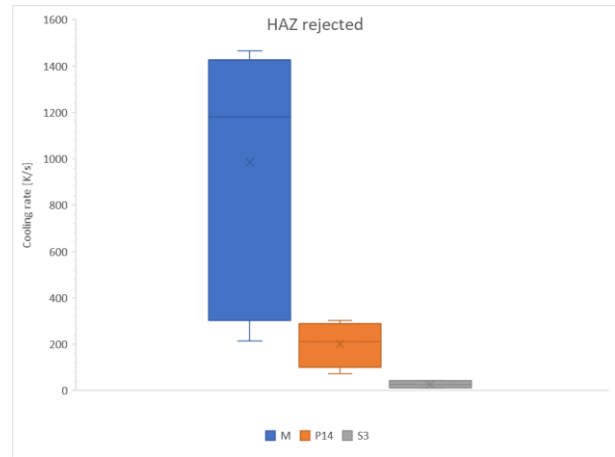


**Figure 5.25: HAZ rejected from the cooling rates, calculated with equation (2) for the WAAM specimen M, the permanent mold casting P14 and the sand mold casting S3**

Table 5.1 and Table 5.2 gives a briefly comparing overview of the average SDAS and cooling rates based on the images captured in LOM or SEM for the specimens M, P14 and S3, with HAZ rejected for M in the last row. The average SDAS value for M is more closed when the HAZ is rejected. Based on the tables, we can assume the final values for SDAS are between 6-7  $\mu\text{m}$ , 11-16  $\mu\text{m}$  and 19-21  $\mu\text{m}$  for M, P14 and S3 respectively and for the cooling rates approximate 590-680  $\text{Ks}^{-1}$ , 120-130  $\text{Ks}^{-1}$ , and 10-30  $\text{Ks}^{-1}$  respectively. With equation (2), the SDAS values decreases with 0.6-3.3  $\mu\text{m}$  and the cooling rates increases with between 11 and 677  $\text{Ks}^{-1}$ .

Haselhuhn et al. [2] reported an average SDAS during wedge casting to be approximate 8.5  $\mu\text{m}$ . The resulting cooling was thus estimated to 240  $\text{Ks}^{-1}$ . This fits well with the permanent mold casting P14 when using the same equation (2): 9.2  $\mu\text{m}$  and 200  $\text{Ks}^{-1}$ . The final question is, which of the equation (1) and (2) represents the real-world case?

	Equation (1)			Equation (2)		
	M	P14	S3	M	P14	S3
<b>LOM images</b>	6.41	16.14	19.22	5.79	14.51	17.13
<b>SEM images</b>	6.05	11.33	21.50	5.31	9.21	18.19
<b>SEM images, HAZ rejected</b>	6.43			5.68		

**Table 5.1: Comparing the SDAS [ $\mu\text{m}$ ] for the WAAM specimen M, the permanent mold casting P14 and the sand mold casting S3, calculated by either equation (1) or (2)**

	Equation (1)			Equation (2)		
	M	P14	S3	M	P14	S3
<b>LOM images</b>	591	133	30	813	194	41
<b>SEM images</b>	1018	116	14	1695	200	26
<b>SEM images HAZ rejected</b>	679			985		

**Table 5.2: Comparing the cooling rates [ $\text{Ks}^{-1}$ ] for the WAAM specimen M, the permanent mold casting P14 and the sand mold casting S3, calculated by either equation (1) or (2)**

The smaller the SDAS, the greater the variation in the cooling rate. To show it, the equation (3) is plotted for SDAS between 1 and 100  $\mu\text{m}$  in Figure 5.26, the cooling rate is in logarithmic scale [ $\log \text{Ks}^{-1}$ ]. This means that the equations have higher susceptibility for variation when the SDAS is small due to the exponent, as observed for the specimen M (5-7  $\mu\text{m}$ ). The equation (3) is the invers function of the equation (7) [12], where the  $\lambda$  is SDAS and  $\Delta T/t_s$  is the cooling rate.

$$\lambda = B \times \left( \frac{\Delta T}{t_s} \right)^{-n} \quad (7)$$

The invers function can be problematic, as the exponent is  $1/0.33 = 3.03$  with positive sign and accelerates the cooling rate exponentially. Results need to be treated carefully when using the equation (3). The very source of the equation (3) stated:

It must here be noted that the exact values for the cooling rates are not obtained but the order will be approximately the same. Dendrite arm coarsening is unlikely to occur because each experiment lasted of the order of 1 s. The use of the resulting dendrite secondary arm spacing will thus be a lower bound because if coarsening occurs, the spacing will be larger and thus the estimated cooling rate becomes lower. [13]

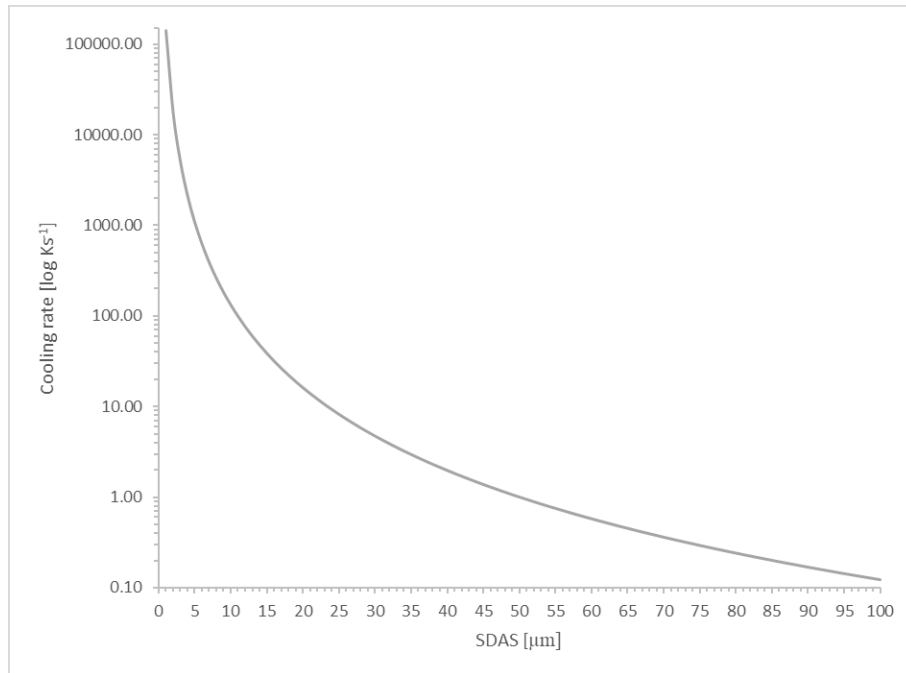


**Figure 5.26: Plot of the cooling rate equation (3) for SDAS 1 to 100  $\mu\text{m}$**

When measuring the SDAS by the method E (Figure 2.5) for dendrites in the SEM images, the average SDAS become 5.5  $\mu\text{m}$ , 11.7  $\mu\text{m}$  and 21.1  $\mu\text{m}$  for M, P14 and S3 respectively. Equation (2) gives a balance of probabilities for this report, as the population is small with approximately ten measurements per image and considerable variation in the microstructures. Equation (1) suites for larger populations, e.g. 50 measurements per image or when the images are more uniform.

Recall to Section 2.3, the method D is widely used by SINTEF and as the report becomes a part of the SINTEF research project, Equation (1) and  $N - 1$  will be the prevalent result.

The final values for the average SDAS in the report are rounded to approximate 6  $\mu\text{m}$ , 11  $\mu\text{m}$  and 21  $\mu\text{m}$  for M, P14 and S3 respectively and for the average cooling rates approximate 620  $\text{Ks}^{-1}$ , 100  $\text{Ks}^{-1}$ , and 15  $\text{Ks}^{-1}$  respectively.

## 5.5 Relationship in the Results

To find the relationship between the cooling rate and the mechanical properties, the results are plotted as stress and elongation vs SDAS in Figure 5.27, and as microhardness vs SDAS in Figure 5.28. The data are enclosed in the Appendix. The sample range is quite small, but the plots help us understand how the connection trends are. The sand castings are not tensile tested and are skipped in the strength plot.

The strengths have minor reduction as the SDAS increases and larger reduction for the elongation. The microhardness decreases with increased SDAS. Recall, the cooling rate increases with decreasing SDAS and then the plots can be interpreted as following: Increased cooling rate gives higher strength, larger elongation and higher hardness in Al-12%Si. P14 is less ductile than M, it can be caused by the casting defects as



mentioned above in this section. Recall to Section 3.2, the WAAM sample is AA 4047 and the casting samples are Al-12Si. The mechanical properties are highly depended of the material compensation, hence samples of the WAAM and the casting should be analyzed.

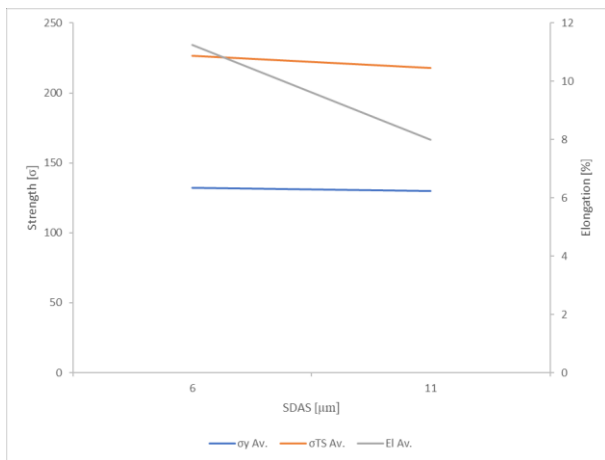


**Figure 5.27: Relationship between strength, elongation and SDAS for the WAAM specimen M and the permanent mold casting P14**

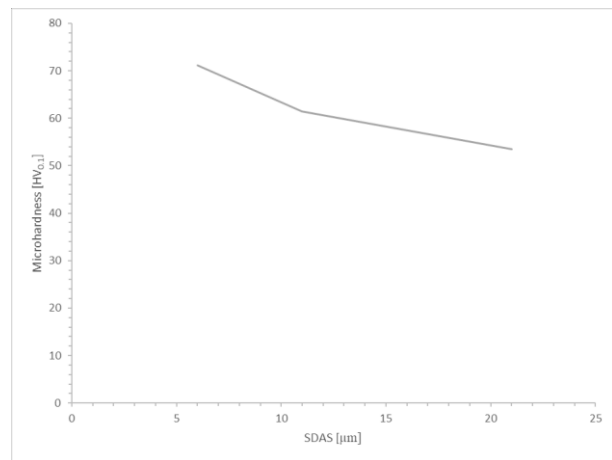


**Figure 5.28: Relationship between microhardness and SDAS for the WAAM specimen M, the permanent mold casting P14 and the sand mold casting S3**



## 6 Conclusion

Two fracture mechanisms are observed in the fractographies for the permanent mold casting P11 (Al-12Si). The first are the brittle (Si) particles and the second the gas and shrinkage pores. The alloy Al-12Si is ductile and fractures when stress concentration takes place in the sharp-edged (Si) particles or pores and grows to intergranular fracture. Also, there are observed dendrite trades in the initial fracture, which indicate inclusions between the dendrite lobes.

The results show a widely variation in the secondary dendrite arm spacing (SDAS), on account of the overlapping beads in the WAAM specimen and to increasing thickness diameter in the awl-shaped castings. The SDAS are smaller in the permanent mold castings P13 and P14 than in the sand mold castings S2 and S3. The WAAM specimen M (AA 4047) has larger SDAS in the partially melted zone (PMZ) than in the fusion zone (FZ). The dendrites in the heat-affected zone (HAZ) are small and entangled. The SDAS measured for the WAAM in the FZ has some resemblance with the SDAS in the middle of the permanent mold castings.

The SDAS calculated by method D and equation (1) are the prevalent result and rounded to approximate 6  $\mu\text{m}$ , 11  $\mu\text{m}$  and 21  $\mu\text{m}$  for M, P14 and S3 respectively. The corresponding average cooling rates are approximate 620  $\text{Ks}^{-1}$ , 100  $\text{Ks}^{-1}$ , and 15  $\text{Ks}^{-1}$  respectively. It turns out that the equation (3) for cooling rates escalates considerably by small SDAS and should not be used in the comparison.

The specimens are compared by strengths, elongation, hardness and SDAS. The microhardness decreases with increased SDAS. Interpreting the plots, the increased cooling rate gives the higher strength, the larger elongation and the higher hardness in Al-12%Si. A permanent mold with even smaller diameter might allow achieving SDAS and a cooling rate closer to the WAAM sample.

Further microstructural analysis should be carried out to analyze the phases around the precipitated (Si) particles and the dendrites. The mechanical properties are highly depended of the material, hence component element properties of the WAAM sample and the casting should be analyzed.



## 7 References

1. Horgar, A., et al., *Additive manufacturing using WAAM with AA5183 wire*. Journal of Materials Processing Tech., 2018. **259**: p. 68-74.
2. Haselhuhn, A.S., et al., *Structure-property relationships of common aluminum weld alloys utilized as feedstock for GMAW-based 3-D metal printing*. Materials Science and Engineering: A, 2016. **673**: p. 511-523.
3. Guo, J. *Feature based cost and carbon emission modelling for wire and arc additive manufacturing*. 2012; Available from: <http://dspace.lib.cranfield.ac.uk/handle/1826/7923>.
4. Zolotarevskii, V.S., *Casting aluminum alloys*, N.A. Belov and M.V. Glazoff, Editors. 2007, Elsevier Science: Amsterdam, Oxford.
5. Vandersluis, E. and C. Ravindran, *Comparison of Measurement Methods for Secondary Dendrite Arm Spacing*. Metallography, Microstructure, and Analysis, 2017. **6**(1): p. 89-94.
6. Askeland, D.R., *The science and engineering of materials*. 5th ed. ed, ed. P.P. Fulay. 2006, Toronto, Ont: Thomson.
7. Haselhuhn, A.S., P.G. Sanders, and J.M. Pearce, *Hypoeutectic aluminum-silicon alloy development for gmaw-based 3-D printing using wedge castings*. International Journal of Metalcasting, 2017. **11**(4): p. 843-856.
8. al., W.U.V.e. *Chvorinov's rule*. 2018 23.10.2018 [cited 2018 20.12]; Available from: [https://en.wikipedia.org/wiki/Chvorinov%27s\\_rule](https://en.wikipedia.org/wiki/Chvorinov%27s_rule).
9. DeGarmo, E.P., *Materials and processes in manufacturing*. 9th ed. ed, ed. R.A. Kohser and J.T. Black. 2003, Hoboken, N.J: Wiley.
10. Pelleg, J., *Mechanical Testing of Materials*, in *Mechanical Properties of Materials*, J. Pelleg, Editor. 2013, Springer Netherlands: Dordrecht. p. 1-84.
11. Langelandsvik, G., *Microhardness distribution in the WAAM specimen M*. 2018, SINTEF Trondheim.
12. Heard, D.W., S. Brophy, and M. Brochu, *Solid freeform fabrication of Al-Si components via the CSC-MIG process*. Canadian Metallurgical Quarterly, 2012. **51**(3): p. 302-312.
13. Jarfors, A.E.W., *Solidification behaviour of Al-7% Si-0.3% Mg during rotary spray forming*. Journal of Materials Science, 1998. **33**(15): p. 3907-3918.



# Appendix





# Data Sheets



## 4047 Aluminum

**Categories:** [Metal](#); [Nonferrous Metal](#); [Aluminum Alloy](#); [4000 Series Aluminum Alloy](#).

**Material Notes:** Data points with the AA note have been provided by the Aluminum Association, Inc. and are NOT FOR DESIGN.

**Composition Notes:**

Composition information provided by the Aluminum Association and is not for design.

**Key Words:** UNS A94047; Aluminium 4047; AA4047; Al4047

**Vendors:** [Eagle Alloys Corporation](#) is a leading supplier of quality metals and alloys. Our staff prides itself on working fast, efficiently and courteously to get you the information you need. Call (800) 237-9012 or visit [www.EagleAlloys.com](http://www.EagleAlloys.com).

[Click here to view all available suppliers for this material.](#)

Please [click here](#) if you are a supplier and would like information on how to add your listing to this material.

Physical Properties	Metric	English	Comments
Density	2.66 g/cc	0.0961 lb/in <sup>3</sup>	AA; Typical

Thermal Properties	Metric	English	Comments
Melting Point	577 - 582 °C	1070 - 1080 °F	
Solidus	577 °C	1070 °F	
Liquidus	582 °C	1080 °F	

Component Elements Properties	Metric	English	Comments
Aluminum, Al	85.3 - 89 %	85.3 - 89 %	As remainder
Beryllium, Be	<= 0.0008 %	<= 0.0008 %	welding electrode and filler wire only
Copper, Cu	<= 0.30 %	<= 0.30 %	
Iron, Fe	<= 0.80 %	<= 0.80 %	
Magnesium, Mg	<= 0.10 %	<= 0.10 %	
Manganese, Mn	<= 0.15 %	<= 0.15 %	
Other, each	<= 0.05 %	<= 0.05 %	
Other, total	<= 0.15 %	<= 0.15 %	
Silicon, Si	11 - 13 %	11 - 13 %	
Zinc, Zn	<= 0.20 %	<= 0.20 %	

[References](#) for this datasheet.

Some of the values displayed above may have been converted from their original units and/or rounded in order to display the information in a consistent format. Users requiring more precise data for scientific or engineering calculations can click on the property value to see the original value as well as raw conversions to equivalent units. We advise that you only use the original value or one of its raw conversions in your calculations to minimize rounding error. We also ask that you refer to MatWeb's [terms of use](#) regarding this information. [Click here](#) to view all the property values for this datasheet as they were originally entered into MatWeb.

# Direct chill casted Al-12Si ingots from Hydro Sunndal Metallverk

18.12.2018 G. Langelandsvik

Charge no.	Mass [kg]	Offcut	%Si	%Fe	%Cu	%Mn	%Mg	%Cr	%Ni	%Zn	%Ga	%Pb	%Ti	%V	%Zr
139349	7.09	0.40	12.742	0.129	0.001	0.004	0.009	0.001	0.004	0.002	0.01	0.001	0.014	0.01	0.004
138009	7.05	0.45	12.765	0.117	0.002	0.002	0.015	0.001	0.004	0.002	0.01	0.001	0.016	0.011	0.002
138677	6.01	0.40	12.859	0.106	0.001	0.001	0.012	0	0.004	0.002	0.011	0.001	0.011	0.004	0.001
<b>Total</b>	<b>20.15</b>	<b>1.25</b>	<b>12.785</b>	<b>0.118</b>	<b>0.001</b>	<b>0.002</b>	<b>0.012</b>	<b>0.001</b>	<b>0.004</b>	<b>0.002</b>	<b>0.010</b>	<b>0.001</b>	<b>0.014</b>	<b>0.009</b>	<b>0.002</b>

Element	Charge 139349	Kons.	Std. avvik
Si		12.74206	0,095747
Fe		0,129426	0,002858
Cu		0,000813	0,000015
Mn		0,003719	0,000113
Mg		0,00891	0,000188
Cr		0,000553	0,000013
Ni		0,004481	0,00002
Zn		0,00175	0,000047
B		0,000106	0,000046
Be		0,000029	0,000004
Bi		0,00001	0
Ca		0,000264	0,000014
Ga		0,01005	0,000163
Li		0,00001	0
Na		0,000016	0,000005
P		0,000414	0,000019
Pb		0,00084	0,000024
Sb		0,000101	0,000046
Sn		0,000073	0,000065
Sr		0,00011	0,000015
Ti		0,01414	0,000171
V		0,009643	0,000146
Zr		0,003536	0,000028
Cd		0,00001	0
Co		0,000243	0,000056
Al		87,114374	0,098025

Element	Charge 138009	Kons.	Std. avvik
Si		12.765013	0,037951
Fe		0,116529	0,001708
Cu		0,002047	0,000019
Mn		0,001759	0,000033
Mg		0,014614	0,000167
Cr		0,0005	0,000006
Ni		0,004293	0,000074
Zn		0,001859	0,000032
B		0,000549	0,000023
Be		0,00003	0
Bi		0,00001	0
Ca		0,000073	0,000015
Ga		0,010289	0,000103
Li		0,00001	0
Na		0,000023	0,000005
P		0,000287	0,00003
Pb		0,00073	0,000012
Sb		0,000019	0,000009
Sn		0,00001	0
Sr		0,000029	0,000004
Ti		0,016001	0,000161
V		0,01055	0,000088
Zr		0,002184	0,00001
Cd		0,00001	0
Co		0,00001	0
Al		87,087843	0,038999

Element	Charge 138677	Kons.	Std. avvik
Si		12.859337	0,062804
Fe		0,105601	0,001835
Cu		0,001133	0,000013
Mn		0,001421	0,000041
Mg		0,011813	0,000235
Cr		0,000164	0,000005
Ni		0,004906	0,000034
Zn		0,001736	0,000032
B		0,000706	0,000024
Be		0,00003	0
Bi		0,00001	0
Ca		0	0
Ga		0,010607	0,000109
Li		0,00001	0
Na		0,000036	0,000005
P		0,000599	0,00003
Pb		0,000706	0,00001
Sb		0,000029	0,000018
Sn		0,000013	0,000008
Sr		0,000236	0,000032
Ti		0,010993	0,000065
V		0,00396	0,000052
Zr		0,000814	0,00001
Cd		0,00001	0
Co		0,000041	0,000046
Al		87,012256	0,063350

CLICK

 for **FREE**  
 Information Technology  
 publication subscriptions.

 No catch.  
 No charge.  
 No kidding!  
**Subscribe Today!**
[Free Trade Publications, Click Here!](#)

## AISI Type H13 Hot Work Tool Steel

 Categories: [Metal](#); [Ferrous Metal](#); [Tool Steel](#); [Hot Work Steel](#)

**Material Notes:** High hardenability, excellent wear resistance and hot toughness. H13 has good thermal shock resistance and will tolerate some water cooling in service. Nitriding improves hardness, but can diminish shock resistance if hardened layer is too thick. Electroslag Remelted (ESR) H13 has greater homogeneity and an exceptionally fine structure, resulting in improved machinability, polishability and high temperature tensile strength.

**Applications:** hot work applications: pressure die casting tools, extrusion tools, forging dies, hot shear blades, stamping dies, plastic molds. ESR H13 is great for aluminum die-casting tools and plastic mold tools requiring a very high polish.

**Weldability:** Pre and Post-heating recommended, can be welded with oxy-acetylene, inert shielded gas and shielded metal arc; Filler should be similar to the base metal.

**Key Words:** UNS T20813, ASTM A681, FED QQ-T-570, BS 4659 BH13, BS 4659 H13, BS EN ISO 4957 :2000 X40CrMoV5-1, Werkstoff 1.2344

**Vendors:** No vendors are listed for this material. Please [click here](#) if you are a supplier and would like information on how to add your listing to this material.



 [Printer friendly version](#)
 [Download as PDF](#)
 [Download to Excel \(requires Excel and Windows\)](#)  
 [Export data to your CAD/FEA program](#)

 Add to Folder:  My Folder ▼  
 0/0

Physical Properties	Metric	English	Comments
Density	7.80 g/cc	0.282 lb/in <sup>3</sup>	

Mechanical Properties	Metric	English	Comments
Hardness, Rockwell C	28 - 30	28 - 30	air or oil quenched and tempered at 705°C (1300°F).
	31 - 33	31 - 33	air or oil quenched and tempered at 675°C (1250°F).
	39 - 41	39 - 41	air or oil quenched and tempered at 650°C (1200°F).
	45 - 47	45 - 47	air or oil quenched and tempered at 620°C (1150°F).
	49 - 51	49 - 51	air or oil quenched and tempered at 595°C (1100°F).
	51 - 53	51 - 53	air or oil quenched and tempered at 565°C (1050°F).
	51 - 53	51 - 53	air quenched from 1025°C (1875°F) or oil quenched from 1010°C (1850°F) with no temper, or tempered for 1 hour at 315°C (600°F), 425°C (800°F), and 480°C (900°F).
	52 - 54	52 - 54	air or oil quenched and tempered at 510°C (950°F) and 540°C (1000°F).
Tensile Strength, Ultimate	1990 MPa	289000 psi	at HRC = 55 (air or oil quenched from 995-1025°C)
Tensile Strength, Yield	1650 MPa	239000 psi	at HRC = 55 (air or oil quenched from 995-1025°C)
Elongation at Break	9.0 %	9.0 %	at HRC = 55 (air or oil quenched from 995-1025°C)
Modulus of Elasticity	210 GPa	30500 ksi	

Bulk Modulus	160 GPa	23200 ksi	Typical for steel.
Poissons Ratio	0.30	0.30	Calculated
Machinability	50 %	50 %	Based on 1% carbon steel. as 100% machinability
Shear Modulus	81.0 GPa	11700 ksi	Estimated from elastic modulus

Thermal Properties	Metric	English	Comments
CTE, linear 	11.0 µm/m-°C @Temperature 25.0 - 95.0 °C	6.11 µin/in-°F @Temperature 77.0 - 203 °F	
	11.5 µm/m-°C @Temperature 25.0 - 205 °C	6.39 µin/in-°F @Temperature 77.0 - 401 °F	
	12.4 µm/m-°C @Temperature 25.0 - 540 °C	6.89 µin/in-°F @Temperature 77.0 - 1000 °F	
Specific Heat Capacity	0.460 J/g-°C @Temperature 0.000 - 100 °C	0.110 BTU/lb-°F @Temperature 32.0 - 212 °F	
Thermal Conductivity 	24.3 W/m-K @Temperature 215 °C	169 BTU-in/hr-ft²-°F @Temperature 419 °F	
	24.3 W/m-K @Temperature 475 °C	169 BTU-in/hr-ft²-°F @Temperature 887 °F	
	24.4 W/m-K @Temperature 350 °C	169 BTU-in/hr-ft²-°F @Temperature 662 °F	
	24.7 W/m-K @Temperature 605 °C	171 BTU-in/hr-ft²-°F @Temperature 1120 °F	

Processing Properties	Metric	English	Comments
Processing Temperature	540 - 650 °C	1000 - 1200 °F	Tempering Temperature
	995 - 1040 °C	1820 - 1900 °F	Hardening Temperature
Annealing Temperature	850 - 870 °C @Time 14400 sec	1560 - 1600 °F @Time 4.00 hour	furnace cool < 20°C/hour

Component Elements Properties	Metric	English	Comments
Carbon, C	0.32 - 0.40 %	0.32 - 0.40 %	
Chromium, Cr	5.13 - 5.25 %	5.13 - 5.25 %	
Iron, Fe	>= 90.9 %	>= 90.9 %	as remainder
Molybdenum, Mo	1.33 - 1.4 %	1.33 - 1.4 %	
Silicon, Si	1.0 %	1.0 %	
Vanadium, V	1.0 %	1.0 %	

Descriptive Properties	Metric	English
Stress Relieving Temperature	600 - 650°C for 2 hours (approx.)	cool in still air; always stress relief before hardening.

[References](#) for this datasheet.

Some of the values displayed above may have been converted from their original units and/or rounded in order to display the information in a consistent format. Users requiring more precise data for scientific or engineering calculations can click on the property value to see the original value as well as raw conversions to equivalent units. We advise that you only use the original value or one of its raw conversions in your calculations to minimize rounding error. We also ask that you refer to MatWeb's [terms of use](#) regarding this information. [Click here](#) to view all the property values for this datasheet as they were originally entered into MatWeb.

**Users viewing this material also viewed the following:**

- [Bohler-Uddeholm UDDEHOLM ORVAR® SUPREME \(Premium AISI H13\) Hot Work Tool Steel](#)
- [Bohler-Uddeholm UDDEHOLM ORVAR® SUPERIOR \(Premium AISI H13\) Hot Work Tool Steel](#)
- [420 Stainless Steel](#)
- [Bohler-Uddeholm SUPERIOR® H13 Hot Work Tool Steel](#)
- [AISI Type O1 Oil-hardening Tool Steel, oil quenched at 800°C, tempered at 425°C](#)

MSTH13A / 14076

**CLICK** for **FREE**  
Information Technology  
publication subscriptions.



No catch.  
No charge.  
No kidding!  
**Subscribe Today!**

[Free Trade Publications, Click Here!](#)

**Other Links:** [Advertising](#) • [Submit Data](#) • [Database Licensing](#) • [Web Design & Hosting](#) • [Trade Publications](#)  
[Supplier List](#) • [Unit Converter](#) • [Reference](#) • [Links](#) • [Help](#) • [Contact Us](#) • [Site Map](#) • [FAQ](#) • [Home](#)



MatWe...

Like Page

[Follow @MatWeb](#)

Please read our [License Agreement](#) regarding materials data and our [Privacy Policy](#). Questions or comments about MatWeb? Please contact us at [webmaster@matweb.com](mailto:webmaster@matweb.com). We appreciate your input.

The contents of this web site, the MatWeb logo, and "MatWeb" are Copyright 1996-2018 by MatWeb, LLC. MatWeb is intended for personal, non-commercial use. The contents, results, and technical data from this site may not be reproduced either electronically, photographically or substantively without permission from MatWeb, LLC.

## Sand, Dry

Categories: [Ceramic](#)

**Material Notes:** Natural material - properties will vary by specimen.

**Vendors:** No vendors are listed for this material. Please [click here](#) if you are a supplier and would like information on how to add your listing to this material.

Physical Properties	Metric	English	Comments
Density	1.60 - 1.70 g/cc	0.0578 - 0.0614 lb/in <sup>3</sup>	

Electrical Properties	Metric	English	Comments
Electrical Resistivity	1000 ohm-cm - 1e+05	1000 ohm-cm - 1e+05	

Thermal Properties	Metric	English	Comments
Specific Heat Capacity	0.753 - 0.799 J/g-°C	0.180 - 0.191 BTU/lb-°F	
Thermal Conductivity	0.270 - 0.340 W/m-K	1.87 - 2.36 BTU-in/hr-ft <sup>2</sup> -°F	

[References](#) for this datasheet.

Some of the values displayed above may have been converted from their original units and/or rounded in order to display the information in a consistent format. Users requiring more precise data for scientific or engineering calculations can click on the property value to see the original value as well as raw conversions to equivalent units. We advise that you only use the original value or one of its raw conversions in your calculations to minimize rounding error. We also ask that you refer to MatWeb's [terms of use](#) regarding this information. [Click here](#) to view all the property values for this datasheet as they were originally entered into MatWeb.



# Aluminum Silicate

CAS #: [1332-58-7](#)

Linear Formula:  $\text{Al}_2\text{O}_3 \cdot 2\text{SiO}_2 \cdot 2\text{H}_2\text{O}$

MDL Number: MFCD00062311

[Email SDS](#)



EC No.: 310-194-1

## ORDER

### (2N) 99% Aluminum Silicate

[Pricing >](#)

[SDS >](#)

[Data Sheet >](#)

### (2N5) 99.5% Aluminum Silicate

[Pricing >](#)

[SDS >](#)

[Data Sheet >](#)

### (3N) 99.9% Aluminum Silicate

[Pricing >](#)

[SDS >](#)

[Data Sheet >](#)

### (3N5) 99.95% Aluminum Silicate

[Pricing >](#)

[SDS >](#)

[Data Sheet >](#)

### (4N) 99.99% Aluminum Silicate

[Pricing >](#)

[SDS >](#)

[Data Sheet >](#)

### (5N) 99.999% Aluminum Silicate

[Pricing >](#)

[SDS >](#)

[Data Sheet >](#)

WHOLESALE/SKU 0000-742-12876

[Question? Ask an American Elements Engineer](#)



## Aluminum Silicate Properties (Theoretical)



<b>Compound Formula</b>	<b><math>\text{Al}_2\text{H}_4\text{O}_9\text{Si}</math></b>
<b>Molecular Weight</b>	<b>258.160437</b>
<b>Appearance</b>	<b>white, grayish, or yellowish powder</b>
<b>Melting Point</b>	<b>N/A</b>
<b>Boiling Point</b>	<b>N/A</b>
<b>Density</b>	<b>2.3 to 2.5 g/cm<sup>3</sup></b>
<b>Specific Heat</b>	<b>840 J/kg-K</b>
<b>Tensile Strength</b>	<b>6.9 to 21 MPa (Ultimate)</b>
<b>Thermal Conductivity</b>	<b>2.0 W/m-K</b>
<b>Thermal Expansion</b>	<b>2.5 to 3.3 <math>\mu\text{m}/\text{m-K}</math></b>
<b>Exact Mass</b>	<b>257.902462</b>
<b>Monoisotopic Mass</b>	<b>257.902462</b>

## Aluminum Silicate Health & Safety Information



<b>Signal Word</b>
<b>Warning</b>
<b>Hazard Statements</b>
<b>N/A</b>
<b>Hazard Codes</b>
<b>N/A</b>
<b>Flash Point</b>
<b>No data</b>



### Risk Codes

N/A

### Safety Statements

N/A

### Transport Information

N/A

[View and Print SDS](#)



### About Aluminum Silicate



Aluminum Silicate is generally immediately available in most volumes. Ultra high purity and high purity compositions improve both optical quality and usefulness as scientific standards. Nanoscale elemental powders and suspensions, as alternative high surface area forms, may be considered. American Elements produces to many standard grades when applicable, including Mil Spec (military grade); ACS, Reagent and Technical Grade; Food, Agricultural and Pharmaceutical Grade; Optical Grade, USP and EP/BP (European Pharmacopoeia/British Pharmacopoeia) and follows applicable ASTM testing standards. Typical and custom packaging is available, as is additional research, technical and safety (MSDS) data. Please contact us for information on lead time and pricing above.

### Aluminum Silicate Synonyms



*Aluminum silicate hydroxide, Bolus, Hydrated aluminum silicate, Kaolin,  $\mu$ -{Hydrogenato(2-)- $\kappa$ O [(hydroxy- $\kappa$ O)(oxo)silyl]silicate}(dioxo)dialuminium dihydrate, Aluminum, dioxo- $\mu$ -[silicic acid (H<sub>2</sub>SiO<sub>3</sub>)ato(2-)- $\kappa$ O, (hydroxy- $\kappa$ O)oxosilyl ester]-, hydrate (1:2), Al<sub>2</sub>SiO<sub>3</sub>(OH)<sub>4</sub>, Imogolite, 12141-46-7, Aluminum oxide silicate, Aluminum Silicate n-Hydrate, aluminum silicate synthetic, aluminum silicate natural, Al<sub>2</sub>O(SiO<sub>4</sub>), Al<sub>2</sub>O<sub>5</sub>Si, 235-253-8, Kerphalite, Pyrax ABB, 37287-16-4, 22708-90-3, 1327-36-2, 22708-90-3, Grade A Lava, Grade M Lava, Aluminosilicate, alumino silicate, aluminosilica, alumina-silica, silica-alumina, Machinable Alumina Silicate L911A*



Chemical Identifiers 	
Linear Formula	$\text{Al}_2\text{O}_3 \cdot 2\text{SiO}_2 \cdot 2\text{H}_2\text{O}$
MDL Number	MFCD00062311
EC No.	310-194-1
Beilstein Registry No.	N/A
Pubchem CID	56841936
IUPAC Name	oxo-oxoalumanyloxy-[oxo(oxoalumanyloxy)silyl] oxysilane; dihydrate
SMILES	<chem>O.O.O=[Al]O[Si](=O)O[Si](=O)O[Al]=O</chem>
Inchl Identifier	InChI=1S/2Al.05Si2.2H2O.20/c;;1-6(2)5-7(3)4;;;;/h;;;2*1H2;;/q2*+1;-2;;;;
Inchl Key	NLYAJNPCOHFWQQ-UHFFFAOYSA-N

Customers For Aluminum Silicate Have Also Viewed 
<a href="#">Magnesium Aluminum Silicate</a>
<a href="#">Aluminum Silicate Nanoparticles</a>
<a href="#">Cordierite</a>
<a href="#">Halloysite Nanoclay</a>
<a href="#">Strontium Silicate Aluminate, Europium and Dysprosium Doped</a>
<a href="#">Halloysite Nanotubes</a>
<a href="#">Yttrium Silicate</a>
<a href="#">Lithium Aluminum Silicate</a>
<a href="#">Lithium Aluminum Silicate (Petalite)</a>

## Additive Manufacturing & 3D Printing

Ceramics

Chemical Manufacturing

Electronics

Life Sciences

Metallurgy

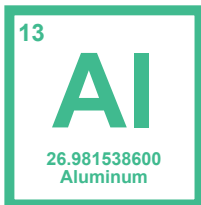
Pigments & Coatings

Research & Laboratory

Silicates

Packaging Specifications

## Related Elements



[See more Aluminum products.](#) Aluminum (or Aluminium) (atomic symbol: Al, atomic number: 13) is a Block P, Group 13, Period 3 element with an atomic weight of 26.9815386. It is the third most abundant element in the earth's crust and the most abundant metallic element. Aluminum's

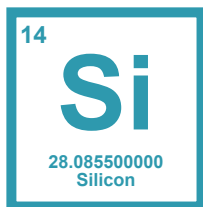


name is derived from alumina, the mineral from which Sir Humphrey Davy attempted to refine it from in 1812. It wasn't until 1825 that Aluminum was first isolated by Hans Christian Oersted. Aluminum is a silvery gray metal that possesses many desirable characteristics. It is light, nonmagnetic and non-sparking. It stands second among [metals](#) in the scale of malleability, and sixth in ductility. It is extensively used in many industrial applications where a strong, light, easily constructed material is needed. Although it has only 60% of the electrical conductivity of [copper](#), it is used in electrical transmission lines because of its light weight. Pure aluminum is soft and lacks strength, but [alloyed](#) with small amounts of [copper](#), [magnesium](#), [silicon](#), [manganese](#), or other elements it imparts a variety of useful properties.



Aluminum was first predicted by Antoine Lavoisier in 1787 and first isolated by Friedrich Wöhler in 1827.





[See more Silicon products.](#) Silicon (atomic symbol: Si, atomic number: 14) is a Block P, Group 14, Period 3 element with an atomic weight of 28.085. The number of electrons in each of Silicon's shells is 2, 8, 4 and its electron configuration is [Ne] 3s<sup>2</sup> 3p<sup>2</sup>. The silicon atom has a radius of 111 pm and a Van der Waals radius of 210 pm.



Silicon was discovered and first isolated by Jöns Jacob Berzelius in 1823. Silicon makes up 25.7% of the earth's crust, by weight, and is the second most abundant element, exceeded only by oxygen. The metalloid is rarely found in pure crystal form and is usually produced



Elemental  
Silicon

from the iron-silicon alloy ferrosilicon. Silica (or [silicon dioxide](#)), as sand, is a principal ingredient of glass, one of the most inexpensive of materials with excellent mechanical, optical, thermal, and electrical properties. [Ultra high purity](#) silicon can be doped with [boron](#), [gallium](#), phosphorus, or [arsenic](#) to produce silicon for use in transistors, [solar cells](#), rectifiers, and other solid-state devices which are used extensively in the [electronics industry](#). The name Silicon originates from the Latin word *sillex* which means flint or hard stone.

## Recent Research

[Effect of barium-coated halloysite nanotube addition on the cytocompatibility, mechanical and contrast properties of poly\(methyl methacrylate\) cement.](#)

[Effect of Added Mullite Whisker on Properties of Lithium Aluminosilicate \(LAS\) Glass-Ceramics Prepared for Dental Restoration.](#)

[Sodium caseinate-magnesium aluminum silicate nanocomposite films for modified-release tablets.](#)

[Phase separation strategy to facilely form fluorescent \[Ag\]/\[Ag\] quantum clusters in boro-aluminosilicate multiphase glasses.](#)

[Non-Isothermal Crystallization Kinetics of Transparent Glass-Ceramic Phosphors Containing Calcium Magnesium Aluminosilicate Nanocrystals.](#)

[Influence of aluminates on the structure and dynamics of water and ions in the nanometer channel of calcium silicate hydrate \(C-S-H\) gel.](#)

[Particle agglomeration of chitosan-magnesium aluminum silicate nanocomposites for direct compression tablets.](#)



Evaluation of synthetic aluminum silicate modified by magnesia for the removal of  $^{137}\text{Cs}$ ,  $^{60}\text{Co}$  and  $^{152+154}\text{Eu}$  from low-level radioactive waste.

The black and white coatings on Ti-6Al-4V alloy or pure titanium by plasma electrolytic oxidation in concentrated silicate electrolyte

Brain aluminium accumulation and oxidative stress in the presence of calcium silicate dental cements.

## TODAY'S SCIENCE POST™ !

December 14, 2018  
Los Angeles, CA

*Each business day American Elements' scientists & engineers post their choice for the most exciting materials science news of the day*



### Foldable Drone Flies through Narrow Holes in Rescue Missions

[Click here to see the primary source for this post and previous posts > > >](#)

**Please join us and our customer and co-sponsor [GlaxoSmithKline](#) at the [IBioIC's Annual Conference 2019, Industrial Biotechnology for a Sustainable Future](#) in Glasgow, Scotland, on January 30 - 31, 2019.**

>

Periodic table of the elements science and academic information, elements and advanced materials data, scientific presentations and all pages, designs, concepts, logos, and color schemes herein are the copyrighted proprietary rights and intellectual property of American Elements. American Elements is a U.S. Registered Trademark. © 1998-2018 American Elements. All rights reserved.





## Aluminum 4043-O

**Categories:** [Metal](#); [Nonferrous Metal](#); [Aluminum Alloy](#); [4000 Series Aluminum Alloy](#)


**Material Notes:** Data points with the AA note have been provided by the Aluminum Association, Inc. and are NOT FOR DESIGN.

**Composition Notes:**

Composition information provided by the Aluminum Association and is not for design.

**Key Words:** UNS A94043; ISO AISi5; Aluminium 4043-O; AA4043-O; Al4043-O

**Vendors:** No vendors are listed for this material. Please [click here](#) if you are a supplier and would like information on how to add your listing to this material.

Physical Properties	Metric	English	Comments
Density	2.69 g/cc	0.0972 lb/in <sup>3</sup>	AA; Typical
Mechanical Properties	Metric	English	Comments
Hardness, Brinell	39	39	500 kg load with 10 mm ball. Calculated value.
Tensile Strength, Ultimate	145 MPa	21000 psi	
Tensile Strength, Yield	70.0 MPa	10200 psi	
Elongation at Break	22 %	22 %	In 5 cm, wire, diameter 1.6 mm
Poissons Ratio	0.34	0.34	Estimated from trends in similar Al alloys.
Shear Strength	90.0 MPa	13100 psi	Calculated value.
Electrical Properties	Metric	English	Comments
Electrical Resistivity	0.00000416 ohm-cm @Temperature 20.0 °C	0.00000416 ohm-cm @Temperature 68.0 °F	AA; Typical
Thermal Properties	Metric	English	Comments
CTE, linear 	22.1 µm/m-°C @Temperature 20.0 - 100 °C	12.3 µin/in-°F @Temperature 68.0 - 212 °F	AA; Typical; average over range
	23.7 µm/m-°C @Temperature 20.0 - 300 °C	13.2 µin/in-°F @Temperature 68.0 - 572 °F	
Specific Heat Capacity	0.850 J/g-°C	0.203 BTU/lb-°F	Estimated from trends in similar Al alloys.
Thermal Conductivity	163 W/m-K	1130 BTU-in/hr-ft <sup>2</sup> -°F	AA; Typical at 77°F
Melting Point	573.9 - 632 °C	1065 - 1170 °F	AA; Typical range based on typical composition for wrought products 1/4 inch thickness or greater
Solidus	573.9 °C	1065 °F	AA; Typical
Liquidus	632 °C	1170 °F	AA; Typical
Processing Properties	Metric	English	Comments
Annealing Temperature	349 °C	660 °F	
Component Elements Properties	Metric	English	Comments
Aluminum, Al	92.3 - 95.5 %	92.3 - 95.5 %	As remainder
Beryllium, Be	<= 0.0008 %	<= 0.0008 %	welding electrode and filler wire only
Copper, Cu	<= 0.30 %	<= 0.30 %	
Iron, Fe	<= 0.80 %	<= 0.80 %	
Magnesium, Mg	<= 0.05 %	<= 0.05 %	
Manganese, Mn	<= 0.05 %	<= 0.05 %	
Other, each	<= 0.05 %	<= 0.05 %	
Other, total	<= 0.15 %	<= 0.15 %	
Silicon, Si	4.5 - 6.0 %	4.5 - 6.0 %	

Titanium, Ti	<= 0.20 %	<= 0.20 %
Zinc, Zn	<= 0.10 %	<= 0.10 %

[References](#) for this datasheet.

Some of the values displayed above may have been converted from their original units and/or rounded in order to display the information in a consistent format. Users requiring more precise data for scientific or engineering calculations can click on the property value to see the original value as well as raw conversions to equivalent units. We advise that you only use the original value or one of its raw conversions in your calculations to minimize rounding error. We also ask that you refer to MatWeb's [terms of use](#) regarding this information. [Click here](#) to view all the property values for this datasheet as they were originally entered into MatWeb.

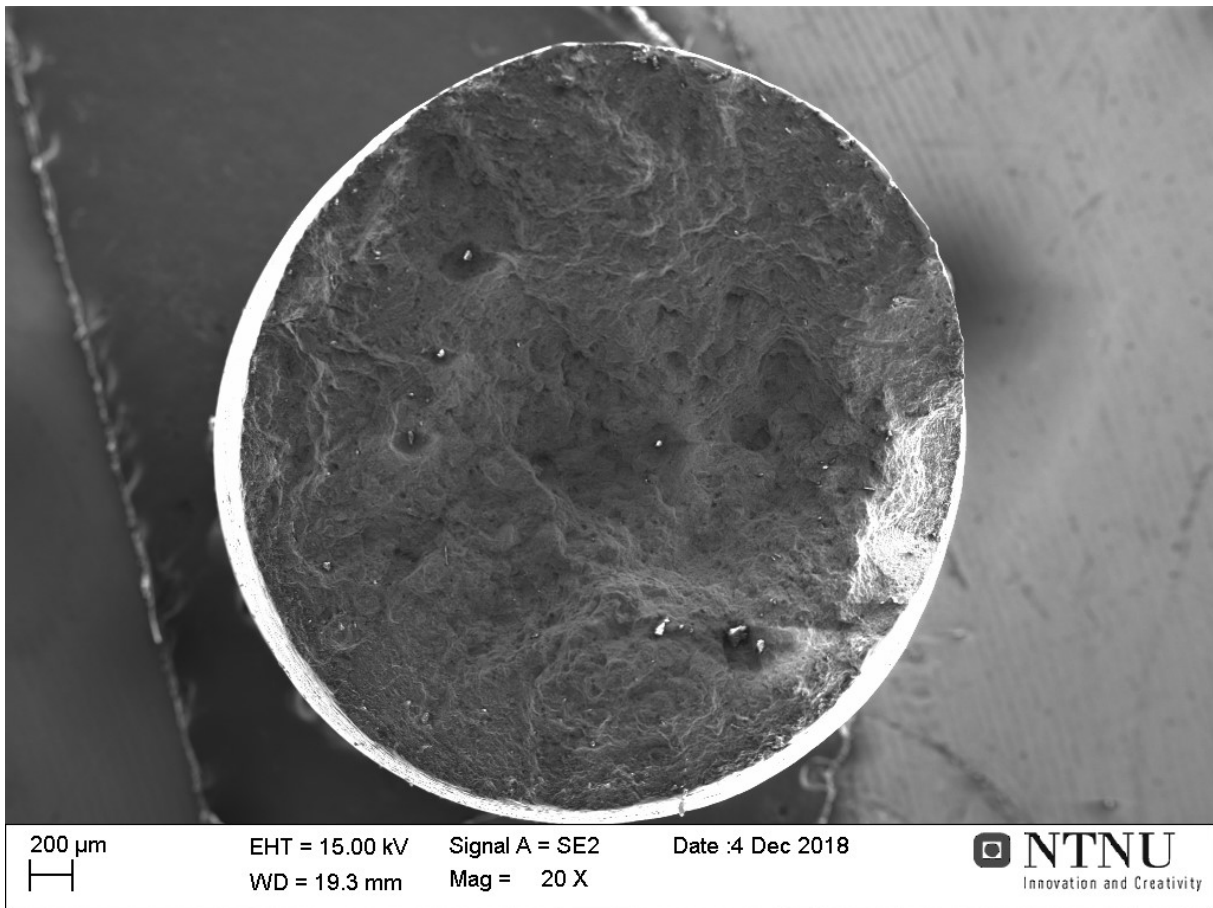
# Images

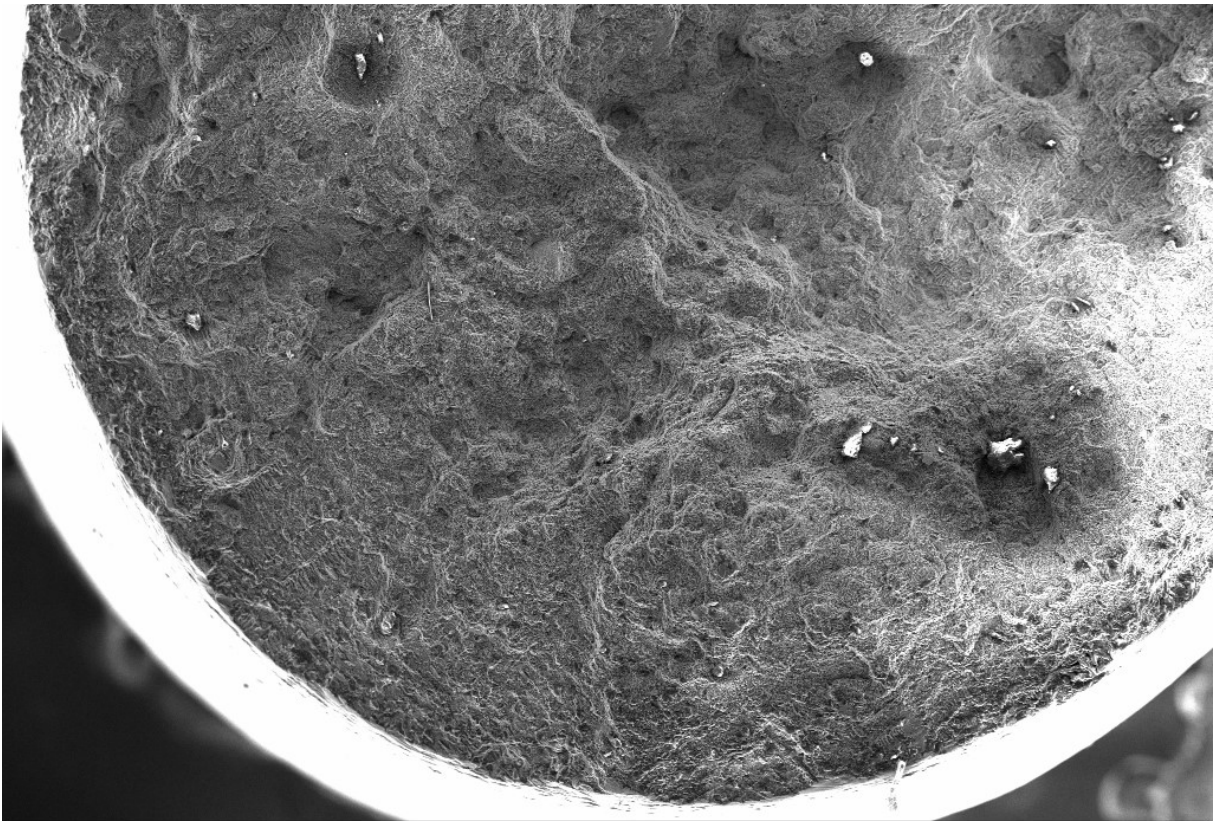


# Fractographies of the Permanent Mold Castings P8 and P11

---

P11: High magnification images





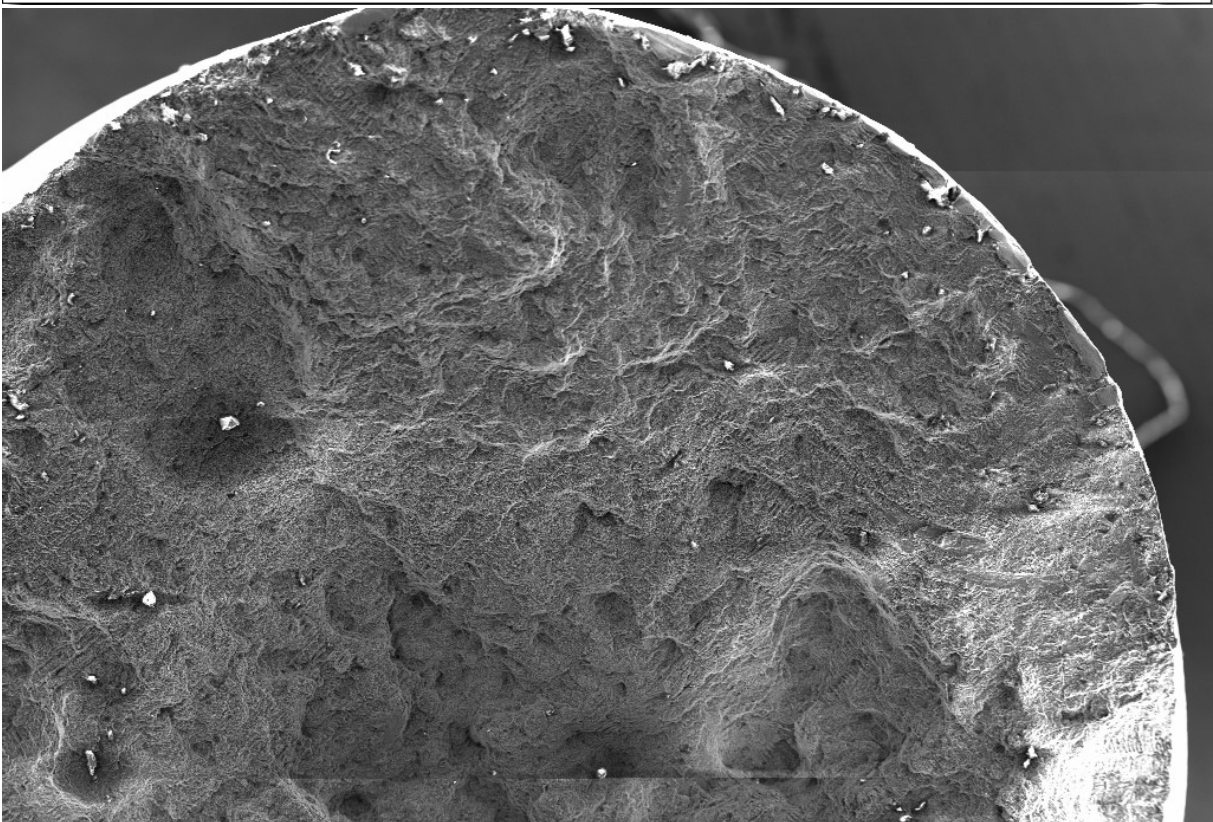
200  $\mu$ m  
|-----|

EHT = 15.00 kV  
WD = 17.9 mm

Signal A = SE2  
Mag = 40 X

Date :4 Dec 2018

 **NTNU**  
Innovation and Creativity



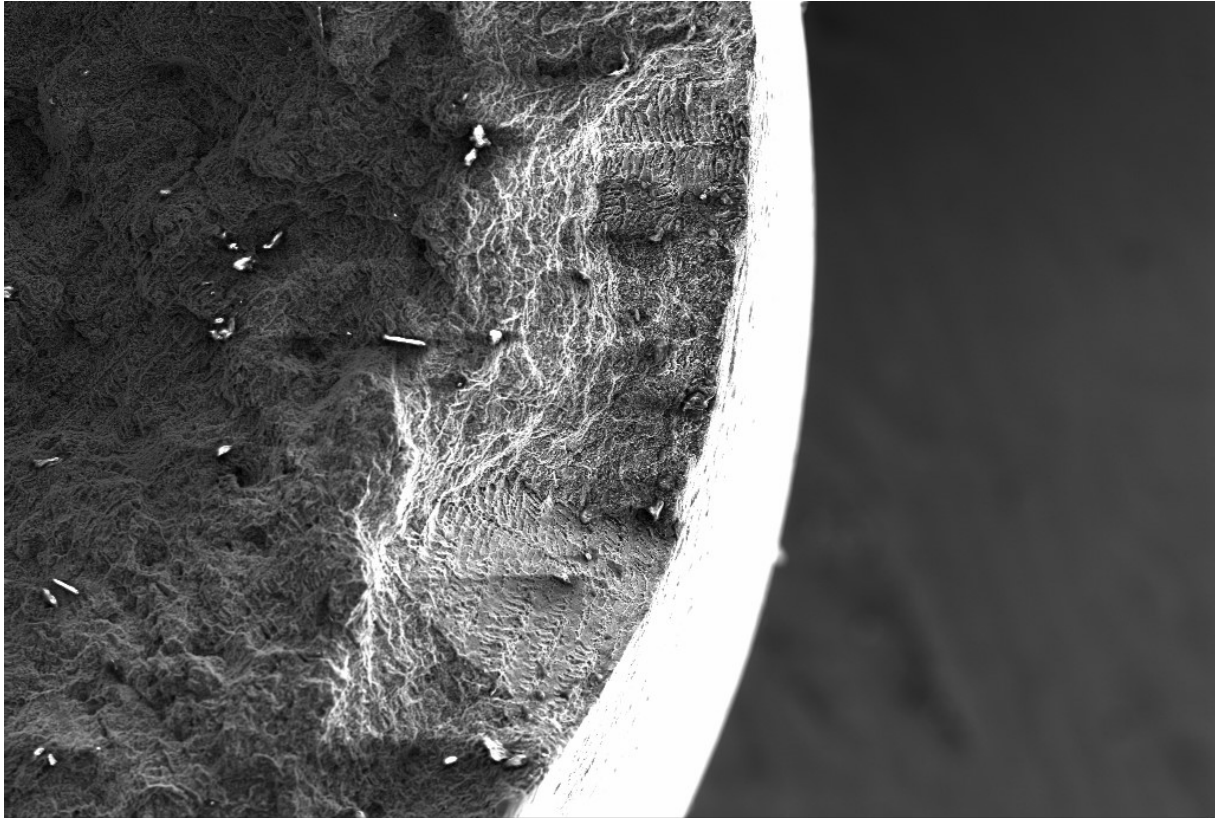
200  $\mu$ m  
|-----|

EHT = 15.00 kV  
WD = 17.7 mm

Signal A = SE2  
Mag = 40 X

Date :4 Dec 2018

 **NTNU**  
Innovation and Creativity



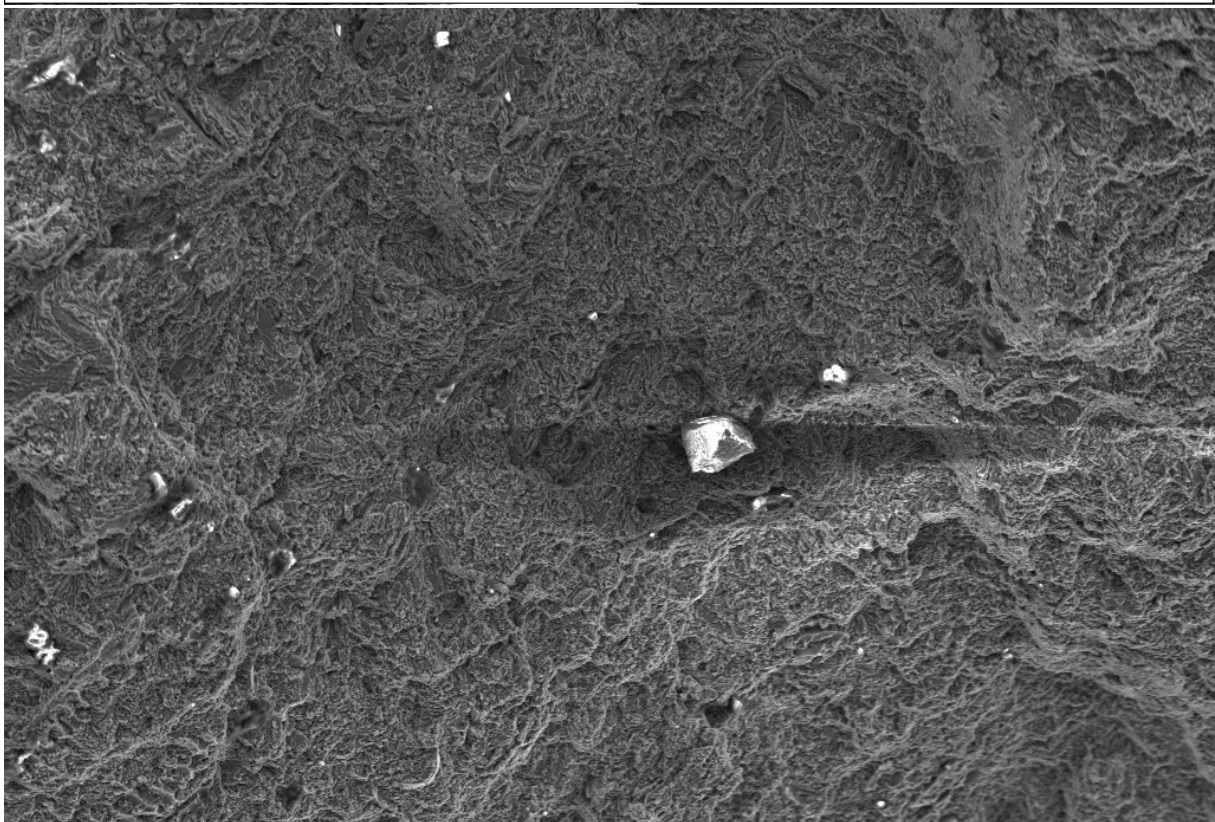
100  $\mu$ m

EHT = 15.00 kV  
WD = 18.3 mm

Signal A = SE2  
Mag = 75 X

Date :4 Dec 2018

 **NTNU**  
Innovation and Creativity



100  $\mu$ m

EHT = 15.00 kV  
WD = 17.4 mm

Signal A = SE2  
Mag = 150 X

Date :4 Dec 2018

 **NTNU**  
Innovation and Creativity



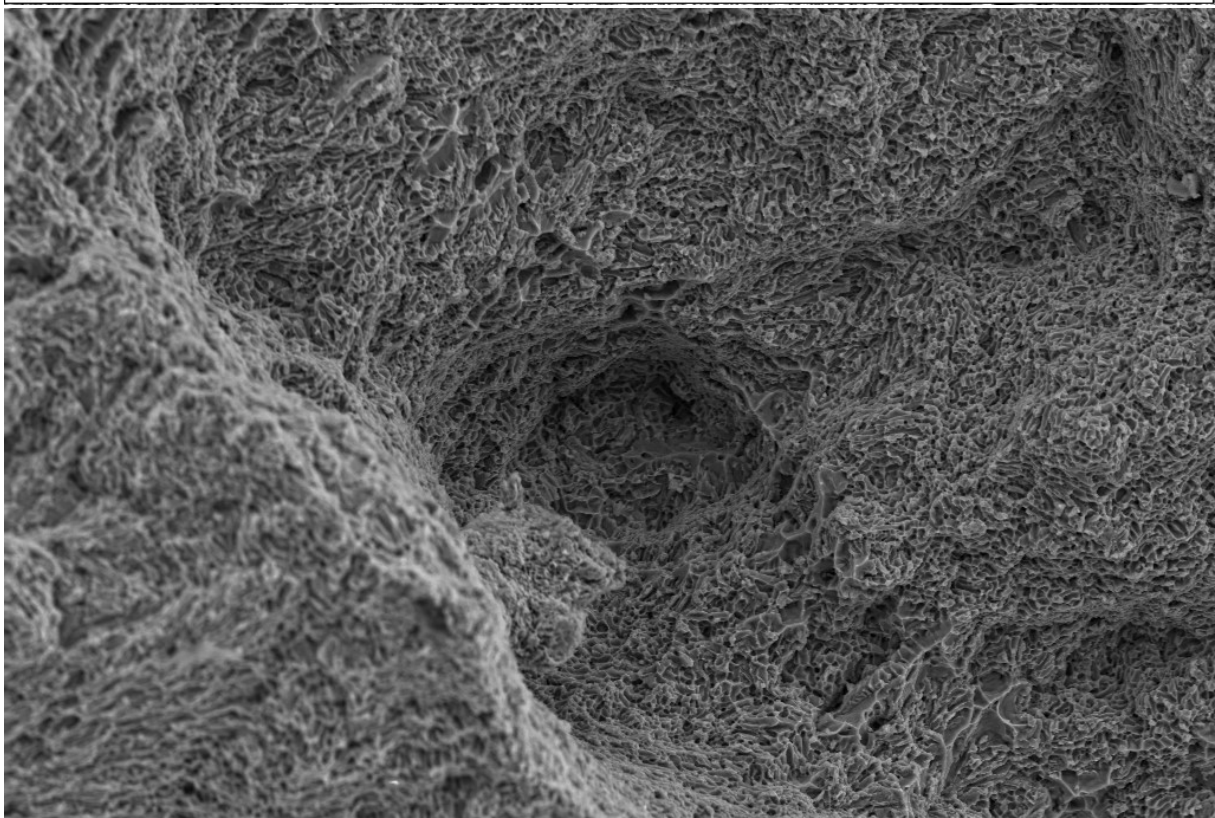
20  $\mu$ m  
┌───┐  
└───┘

EHT = 15.00 kV  
WD = 17.9 mm

Signal A = SE2  
Mag = 200 X

Date :4 Dec 2018

 **NTNU**  
Innovation and Creativity



20  $\mu$ m  
┌───┐  
└───┘

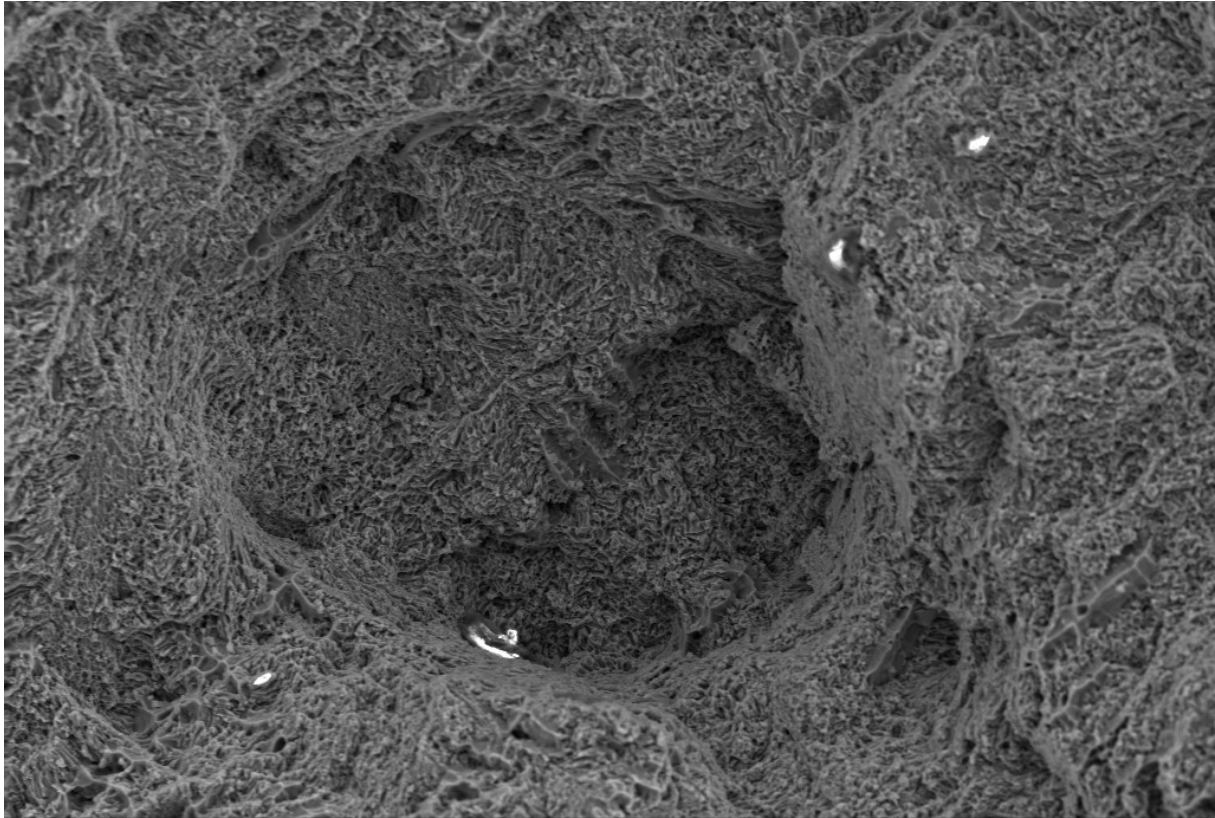
EHT = 15.00 kV  
WD = 18.1 mm

Signal A = SE2  
Mag = 300 X

Date :4 Dec 2018

 **NTNU**  
Innovation and Creativity





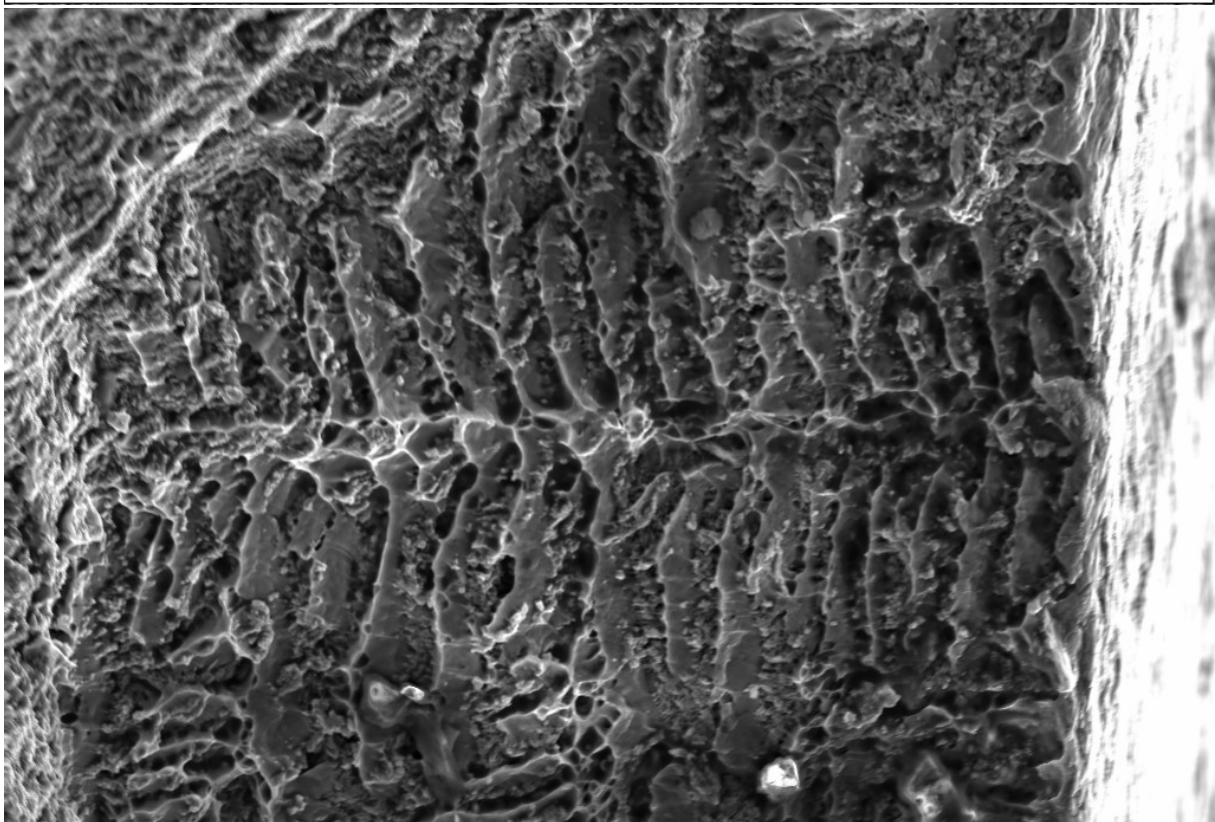
20  $\mu$ m  
|-----|

EHT = 15.00 kV  
WD = 18.3 mm

Signal A = SE2  
Mag = 300 X

Date :4 Dec 2018

 **NTNU**  
Innovation and Creativity



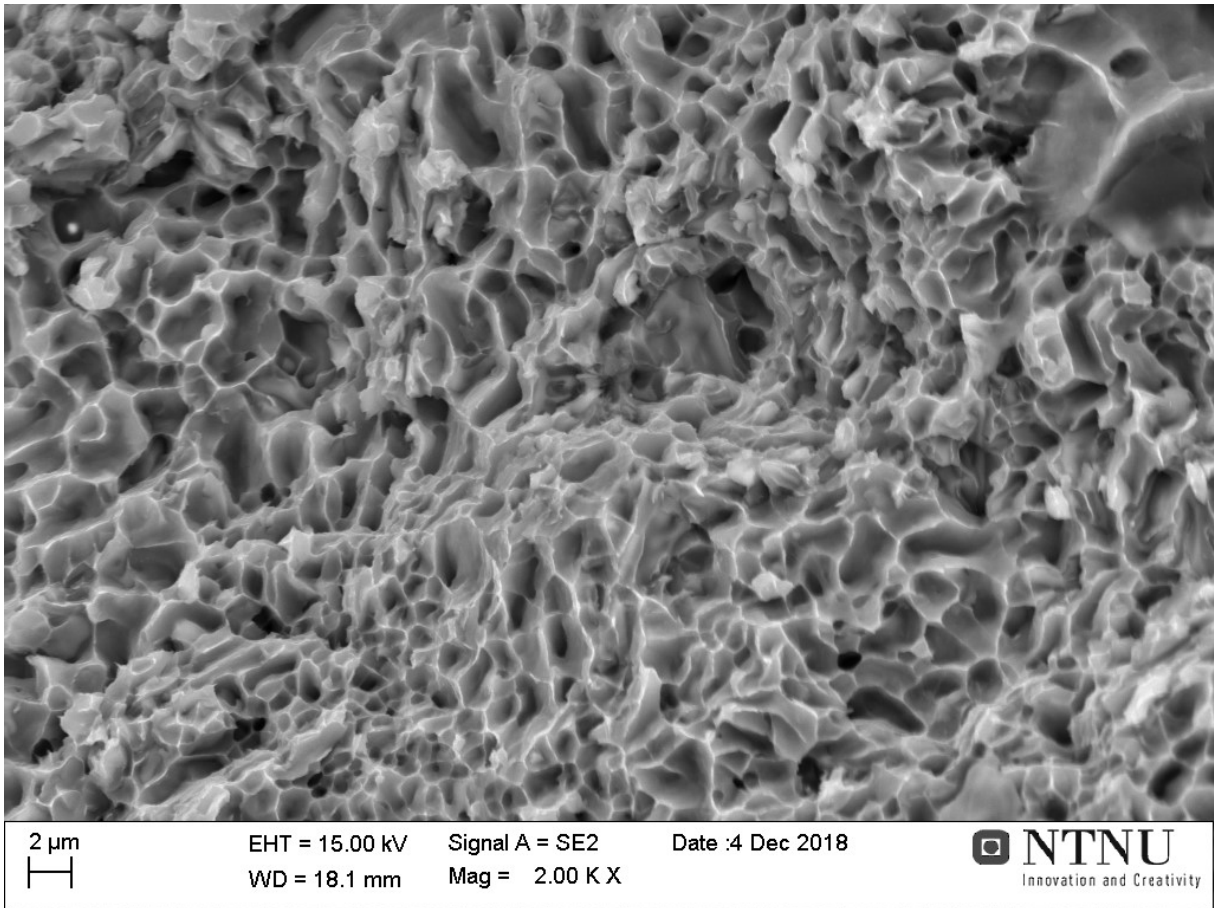
20  $\mu$ m  
|-----|

EHT = 15.00 kV  
WD = 18.2 mm

Signal A = SE2  
Mag = 500 X

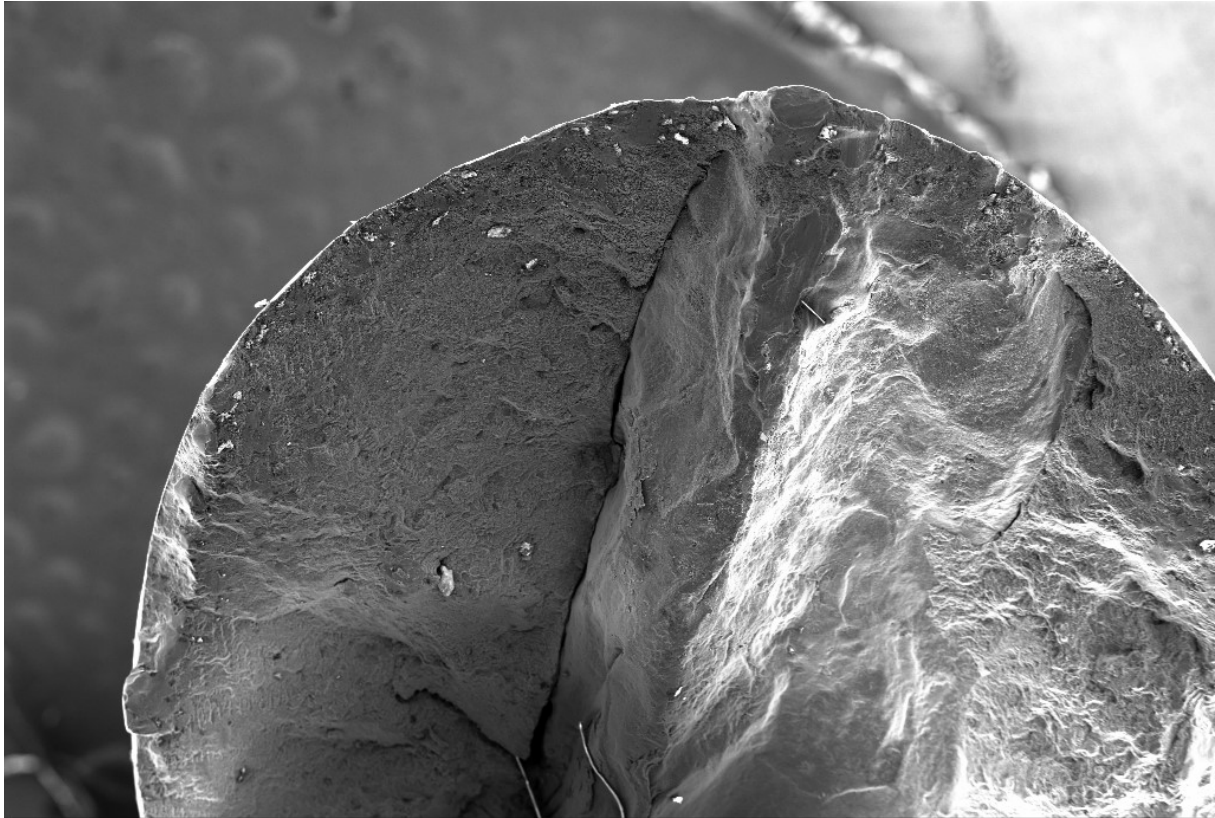
Date :4 Dec 2018

 **NTNU**  
Innovation and Creativity



---

P6: High magnification images



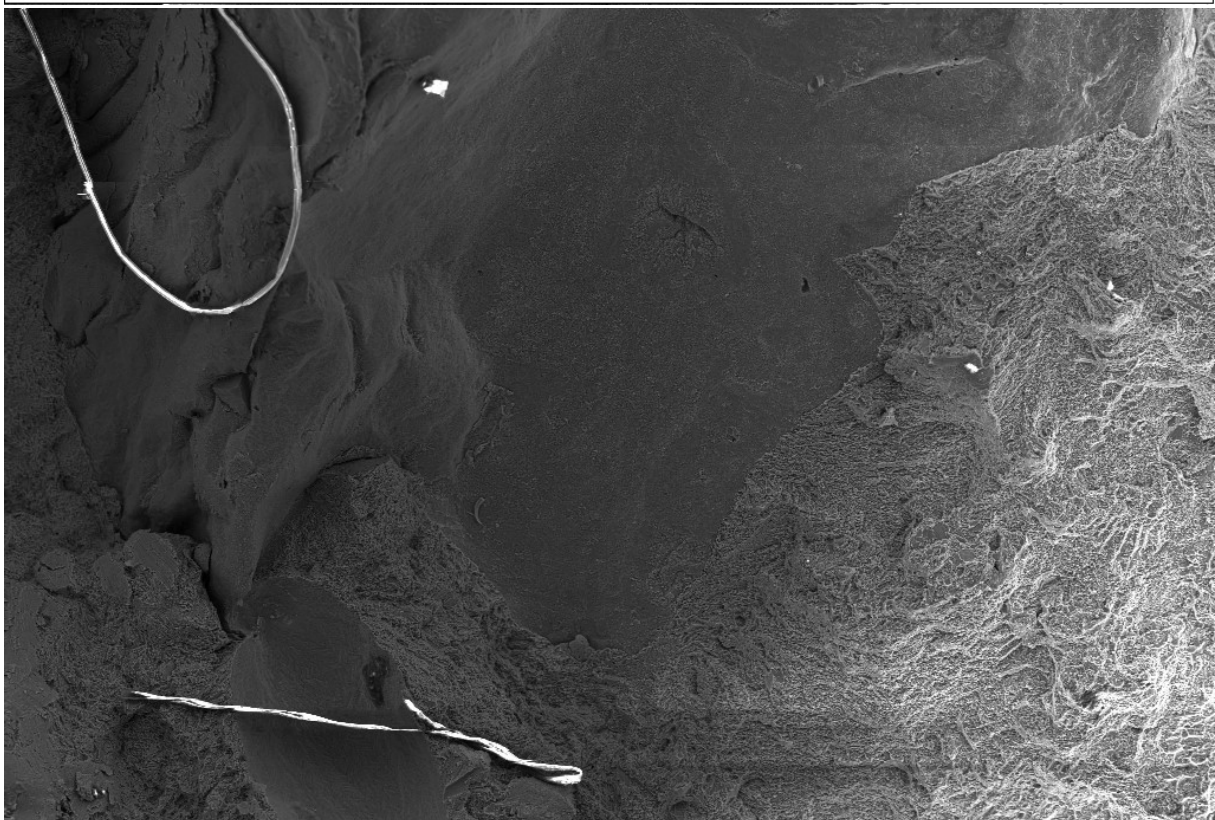
200  $\mu$ m  


EHT = 15.00 kV  
WD = 16.2 mm

Signal A = SE2  
Mag = 30 X

Date :4 Dec 2018

 **NTNU**  
Innovation and Creativity



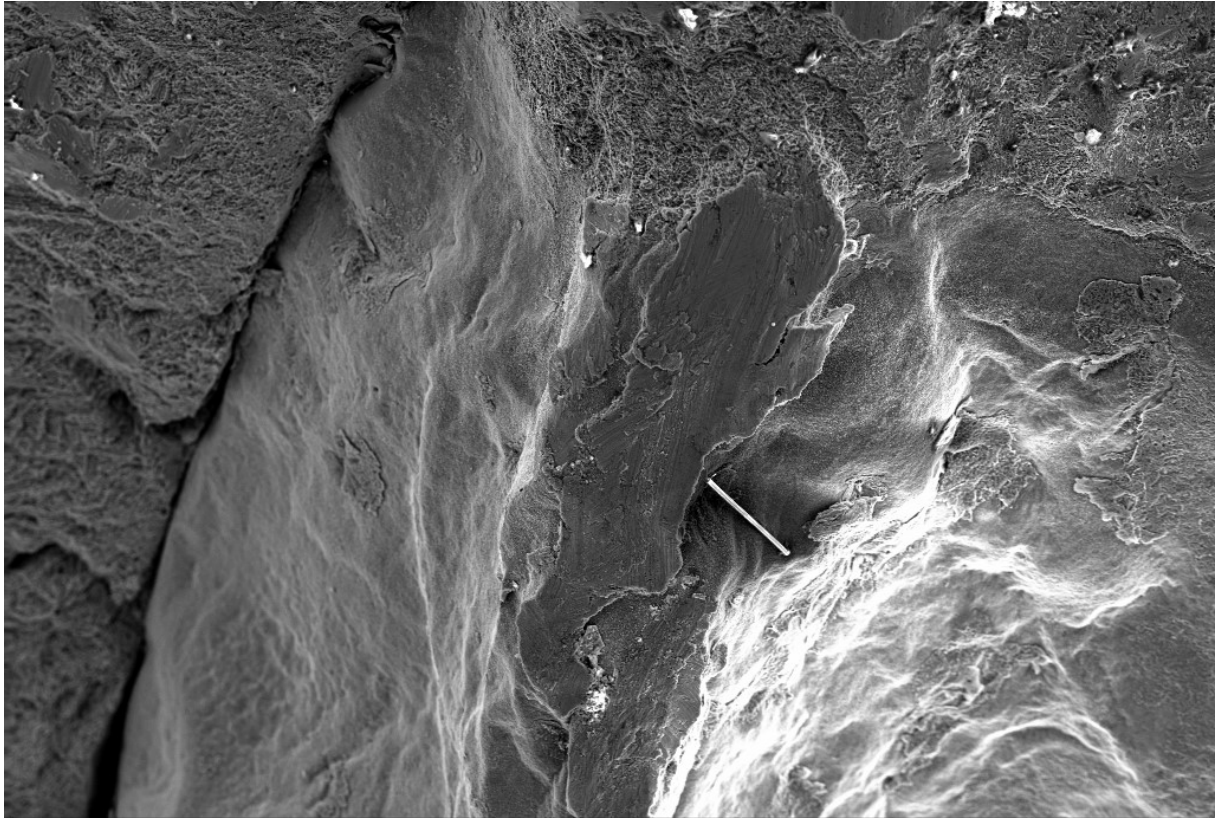
100  $\mu$ m  


EHT = 15.00 kV  
WD = 17.4 mm

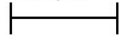
Signal A = SE2  
Mag = 75 X

Date :4 Dec 2018

 **NTNU**  
Innovation and Creativity



100  $\mu$ m



EHT = 15.00 kV

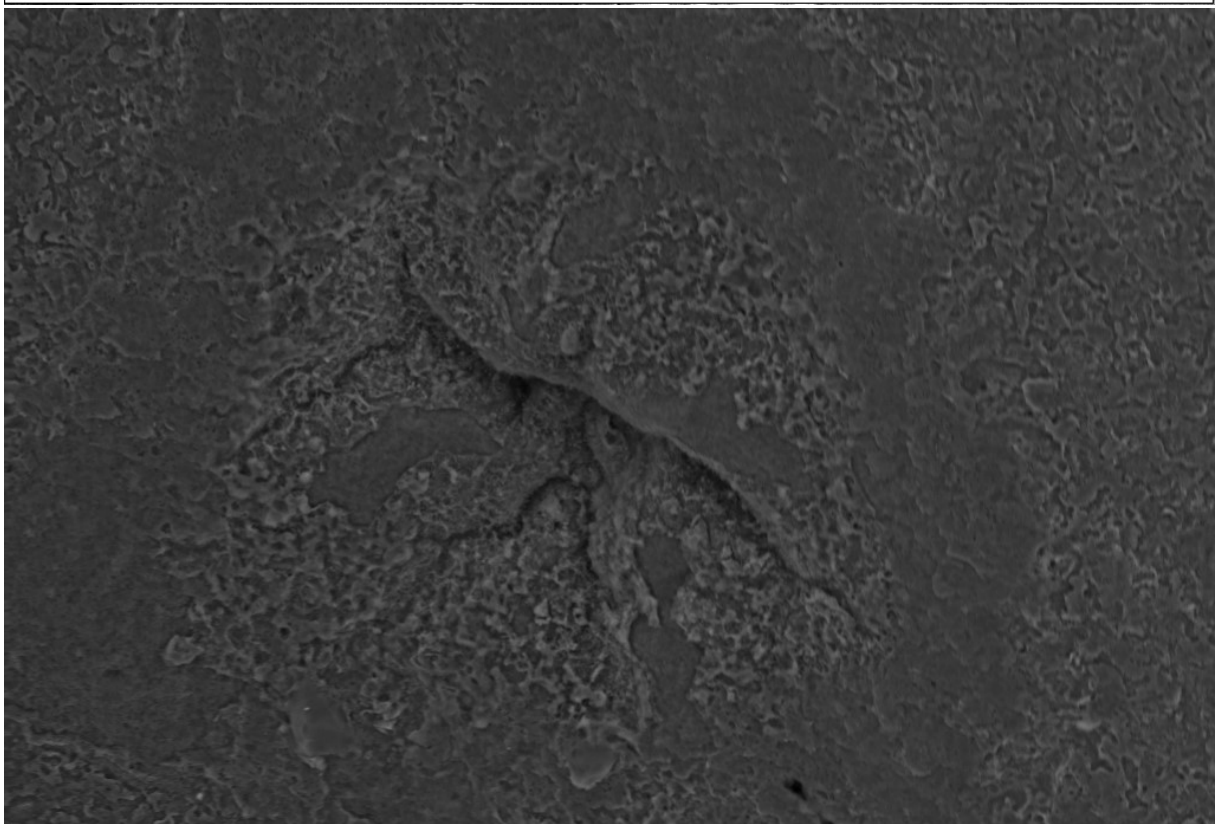
WD = 15.8 mm

Signal A = SE2

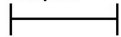
Mag = 100 X

Date :4 Dec 2018

 **NTNU**  
Innovation and Creativity



20  $\mu$ m



EHT = 15.00 kV

WD = 17.3 mm

Signal A = SE2

Mag = 500 X

Date :4 Dec 2018

 **NTNU**  
Innovation and Creativity



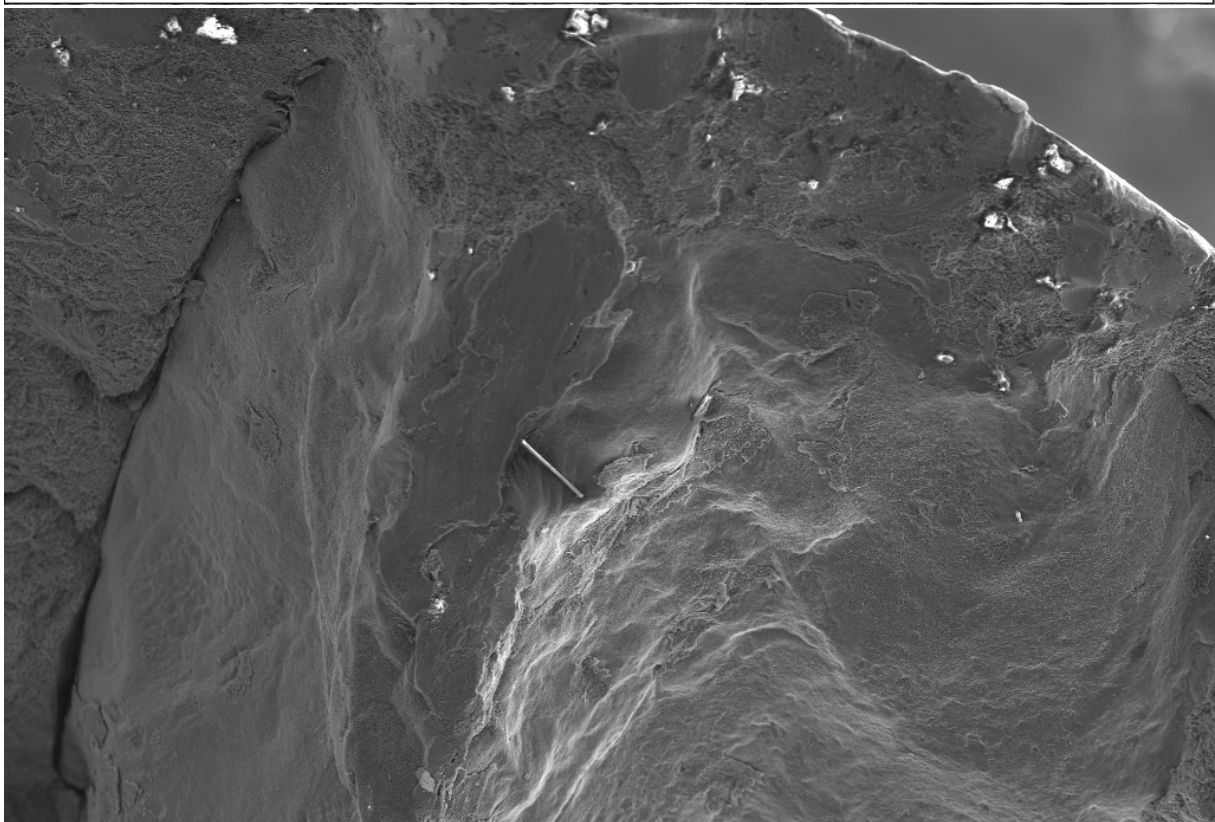
2  $\mu$ m

EHT = 15.00 kV  
WD = 15.9 mm

Signal A = SE2  
Mag = 2.50 K X

Date :4 Dec 2018

 **NTNU**  
Innovation and Creativity



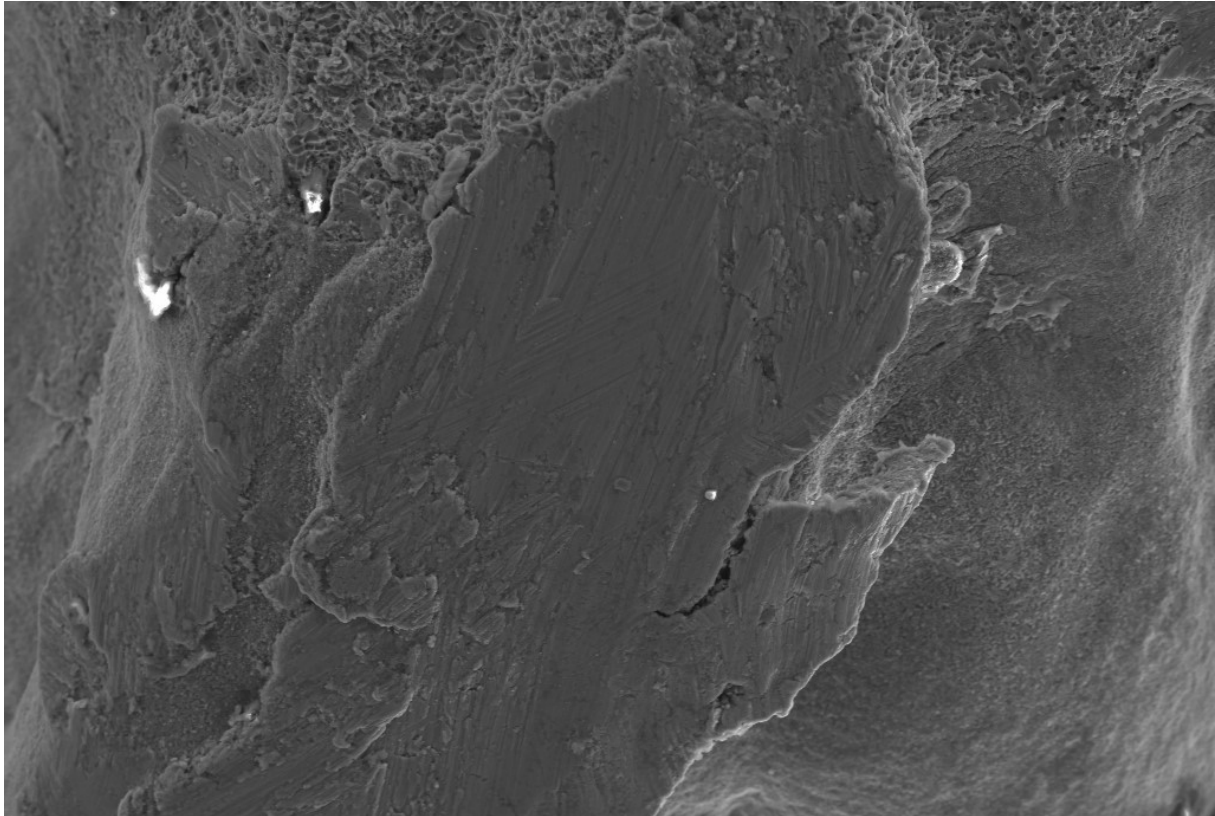
100  $\mu$ m

EHT = 15.00 kV  
WD = 16.1 mm

Signal A = SE2  
Mag = 75 X

Date :4 Dec 2018

 **NTNU**  
Innovation and Creativity



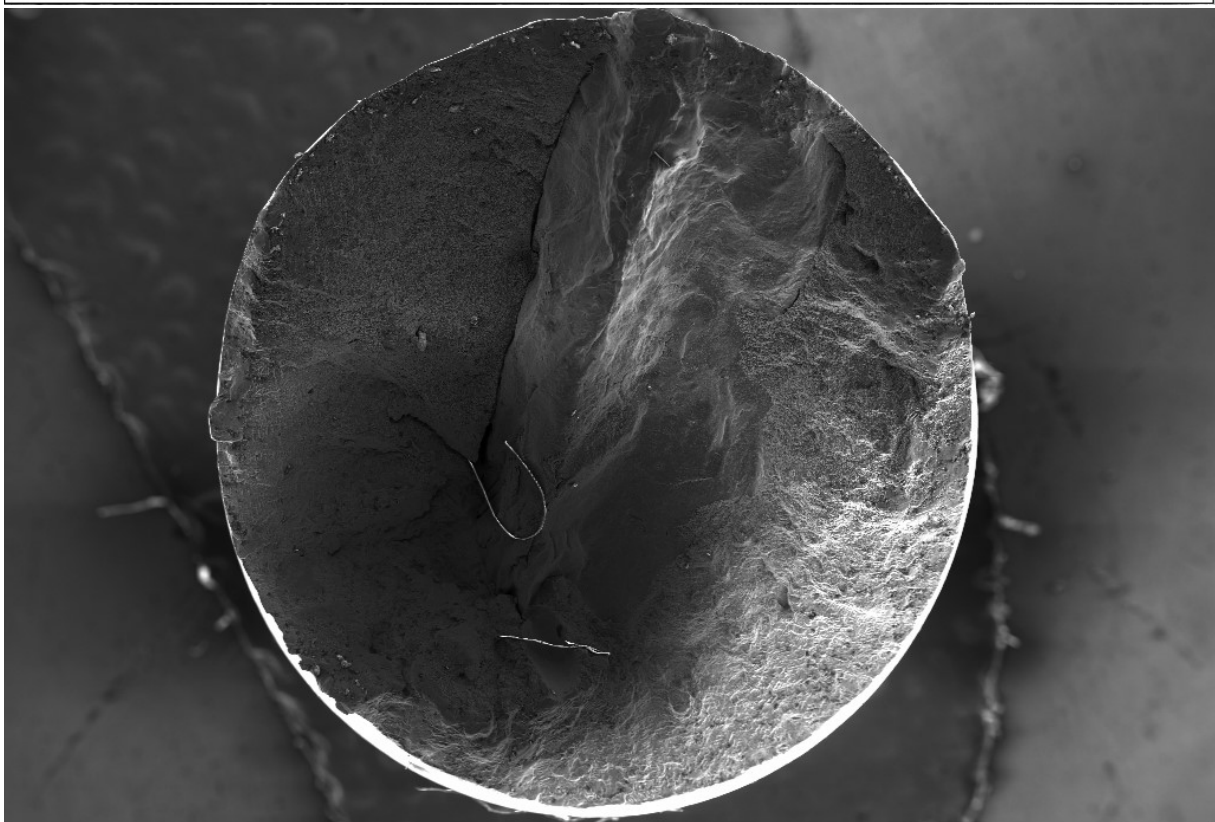
20  $\mu$ m  
H

EHT = 15.00 kV  
WD = 15.7 mm

Signal A = SE2  
Mag = 300 X

Date :4 Dec 2018

 **NTNU**  
Innovation and Creativity



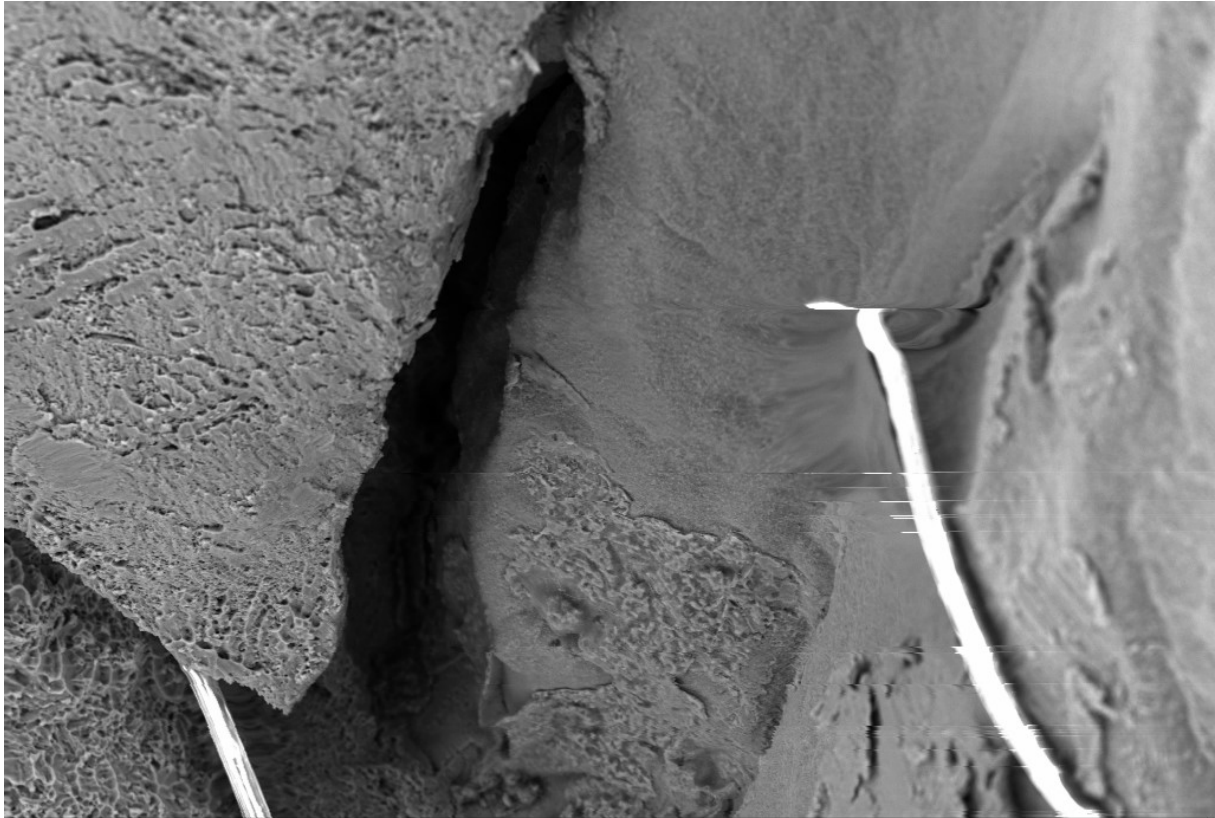
200  $\mu$ m  
H

EHT = 15.00 kV  
WD = 17.0 mm

Signal A = SE2  
Mag = 19 X

Date :4 Dec 2018

 **NTNU**  
Innovation and Creativity



20  $\mu$ m  
|-----|

EHT = 15.00 kV  
WD = 17.3 mm

Signal A = SE2  
Mag = 300 X

Date :4 Dec 2018

 **NTNU**  
Innovation and Creativity





# Calculations



### Permanent mold

#### AA 4047

Melting temperature of the liquid	C	Tm	582	Datasheet Matweb
Temperature of the pour	C	Tpour	650	Measured
Superheat	K	Delta Ts	68	Calculated
Density of the metal	kg/m3	pm	2660	Datasheet Matweb
Specific heat of the metal	J/kgK	cm	850	Borrow from AA 4043, Matweb
Latent heat of fusion	J/kgK	L	1	Not needed

#### Steel AISI H13

Initial temperature of the mold	C	T0	200	Measured
Thermal conductivity of the mold	W/mK	k	24	Datasheet Matweb
Density of the mold	kg/m3	p	7800	Datasheet Matweb
Specific heat of the mold	J/kgK	c	460	Datasheet Matweb

#### Solidification

Volume of the mold (unmachined)	V0	m3	0.000840	Measured
Volume of the mold (machined)	V1	m3	0.000760	Measured
Volume of the casting	V	m3	0.000080	Calculated
Contact surface area	A	m2	0.005666	Measured
<b>Solidification time</b>	<b>ts</b>	<b>s</b>	<b>0.29</b>	<b>Calculated</b>
<b>Mold constant permanent</b>	<b>B</b>	<b>s/m2</b>	<b>1459</b>	<b>Calculated</b>

### Sand mold

#### AA 4047

Melting temperature of the liquid	C	Tm	582	Datasheet Matweb
Temperature of the pour	C	Tpour	650	Measured
Superheat	K	Delta Ts	68	Calculated
Density of the metal	kg/m3	pm	2660	Datasheet Matweb
Specific heat of the metal	J/kgK	cm	850	Borrow from AA 4043, Matweb
Latent heat of fusion	J/kgK	L	1	Not needed

#### Sand

Initial temperature of the mold	C	T0	20	Measured
Thermal conductivity of the mold	W/mK	k	0.34	Datasheet Matweb
Density of the mold	kg/m3	p	1700	Datasheet Matweb
Specific heat of the mold	J/kgK	c	340	Datasheet Matweb

#### Solidification time

Volume of the mold (unmachined)	V0	m3	0.000840	Measured
Volume of the mold (machined)	V1	m3	0.000760	Measured
Volume of the casting	V	m3	0.000080	Calculated
Contact surface area	A	m2	0.005666	Measured
<b>Solidification time</b>	<b>ts</b>	<b>s</b>	<b>60</b>	<b>Calculated</b>
<b>Mold constant sand</b>	<b>B</b>	<b>s/m2</b>	<b>299109</b>	<b>Calculated</b>

### Riser

#### AA 4047

Melting temperature of the liquid	C	Tm	582	Datasheet Matweb
Temperature of the pour	C	Tpour	650	Measured
Superheat	K	Delta Ts	68	Calculated
Density of the metal	kg/m3	pm	2660	Datasheet Matweb
Specific heat of the metal	J/kgK	cm	850	Borrow from AA 4043, Matweb
Latent heat of fusion	J/kgK	L	1	Not needed

#### Fiber

Initial temperature of the mold	C	T0	20	Measured
Thermal conductivity of the mold	W/mK	k	2	Datasheet Matweb
Density of the mold	kg/m3	p	2500	Datasheet Matweb
Specific heat of the mold	J/kgK	c	840	Datasheet Matweb

#### Solidification time

Fiber bush height	H	m	0.04	Measured
Fiber bush outer diameter	Do	m	0.04	Measured
Fiber bush inner diameter	di	m	0.03	Measured
Volume of the casting	V	m3	0.000028	Calculated
Contact surface area	A	m2	0.003770	Calculated
<b>Solidification time</b>	<b>ts</b>	<b>s</b>	<b>0.79</b>	
<b>Mold constant fiber</b>	<b>B</b>	<b>s/m2</b>	<b>13995</b>	<b>Calculated</b>



Data



# Summary of the tensile test results for the WAAM specimens

15.05.2018 Geir Langelandsvik/Annbjørg Horgar

Length	90
--------	----

Results								
Specimen	d [mm]	E [Gpa]	$\sigma_y$ [MPa]	$\sigma_{TS}$ [MPa]	$\epsilon$ at offset yield [mm/mm]	$\epsilon$ at break [mm/mm]	EI [%]	Note
P6	4.01	21.095	129.2	225.4	0.00694	0.1167	10.5	
P7	4.01	16.762	127.7	214.4	0.00768	0.08424	7.6	
P8	4.02	23.511	118.8	155.4	0.00591	0.01199	1.1	Particles in fracture surface
P9	3.97	18.617	136.4	219	0.00749	0.05877	5.3	
P10	4	23.997	126.8	217	0.00648	0.07462	6.7	
P11	4.02	17.512	128.5	213.7	0.00742	0.10964	9.9	

Adjusted		P8 rejected						
Specimen	d [mm]	E [Gpa]	$\sigma_y$ [MPa]	$\sigma_{TS}$ [MPa]	$\epsilon$ at offset yield [mm/mm]	$\epsilon$ at break [mm/mm]	EI [%]	Comments
P6	4.01	21.095	129.2	225.4	0.00694	0.1167	10.5	
P7	4.01	16.762	127.7	214.4	0.00768	0.08424	7.6	
P9	3.97	18.617	136.4	219.0	0.00749	0.05877	5.3	
P10	4	23.997	126.8	217.0	0.00648	0.07462	6.7	
P11	4.02	17.512	128.5	213.7	0.00742	0.10964	9.9	

Specimens	E Av.	E STD	$\sigma_y$ Av.	$\sigma_y$ STD	$\sigma_{TS}$ Av.	$\sigma_{TS}$ STD	EI Av.	EI STD
P6-P11	19.6	2.6	129.7	3.4	217.9	4.2	7.99	1.95

# Summary of the Porosity for P14 and S3

18.12.2018 Annbjørg Horgar

Slice	Count	Total Area	Average Size	%Area	Circ.	Solidity	Feret	FeretX	FeretY	FeretAngle	MinFeret
P14-A_SCALE.jpg	18	0.01	5.36E-04	0.012	0.957	0.882	0.037	18.758	4.791	102.909	0.022
P14-A_SCALE.jpg	22	0.028	0.001	0.034	0.894	0.858	0.047	20.692	9.499	110.047	0.028
P14-B_SCALE.jpg	8	0.021	0.003	0.008	0.972	0.91	0.061	21.651	5.579	116.837	0.04
P14-B_SCALE.jpg	6	0.005	9.05E-04	0.003	0.902	0.841	0.051	24.287	10.579	89.303	0.027
Average				0.01425							
STD				0.01184							

S3-A_SCALE.jpg	122	0.261	0.002	0.26	0.902	0.867	0.055	14.679	4.947	105.993	0.034
S3-A_SCALE.jpg	102	0.401	0.004	0.35	0.884	0.871	0.071	14.87	11.337	106.859	0.044
S3-B_SCALE.jpg	169	85.007	0.503	0.375	0.923	0.898	0.872	249.298	50.115	113.358	0.545
S3-B_SCALE.jpg	123	83.982	0.683	0.388	0.928	0.928	0.912	238.566	127.743	113.16	0.58
Average				0.34325							
STD				0.04997							



# Summary of Porosity in WAAM sample

18.12.2018 Annbjørg Horgar

Based on LOM

Slice	Count	Total Area	Average Size	%Area	Circ.	Solidity	Feret	FeretX	FeretY	FeretAngle	MinFeret
xy BF 100X SB.tif	11	0.033	0.003	0.038	0.959	0.926	0.069	6.116	4.985	118.445	0.058
12.jpg	1431	5.508	0.004	0.341	0.972	0.894	0.091	25.286	21.394	121.418	0.059
yz BF 100X SB.tif	11	0.036	0.003	0.031	0.921	0.917	0.073	5.161	5.005	97.107	0.061
Average				0.13667							
STD				0.14451							

## Summary of the tensile test results for the WAAM specimens

15.05.2018 Geir Langelandsvik/Annbjørg Horgar

Length	80
--------	----

Specimen	d [mm]	E [GPa]	$\sigma_y$ [MPa]	$\sigma_{TS}$ [MPa]	$\epsilon$ at break	%El	Note
Y1	4.03	78.2	141.2	238.1	0.10481	8.4	
Y2	4.03	64.5	137.3	238.2	0.12569	10.1	
Y3	4	63.6	138.4	236.9	0.11139	8.9	Small inner pores
Y4	4.01	70.8	134.4	230.1	0.10895	8.7	
Y5	4.05	64.6	133.1	225.5	0.10428	8.3	Inner pores
X1	4.05	75.5	136	233.6	0.14818	11.9	
X2	4.01	76.5	132.2	230.1	0.15097	12.1	Fracture in distance from the middle. Small surface pore
X3	4.03	61.8	129.9	220	0.12937	10.3	Large inner pores
X4	4.03	69.8	132.2	229	0.12915	10.3	Surface pore
X5	4	73.3	132	229.2	0.15484	12.4	
X6	4.03	64.4	131.7	218.4	0.13143	10.5	Small inner pores
Z1	3.98	75.6	134.9	227.4	0.09809	7.8	Small inner pores
Z2	4	68.3	139.9	237.9	0.10857	8.7	
Z3	4.04	58.5	135.5	228.2	0.12421	9.9	Inner pores
Z4	4	82.6	129.7	228.9	0.10316	8.3	Inner pores
Z5	4	71.1	145.3	233.7	0.13112	10.5	Fracture in distance from the middle
Z6	4.05	61.5	133.1	220.3	0.12676	10.1	Large inner pore

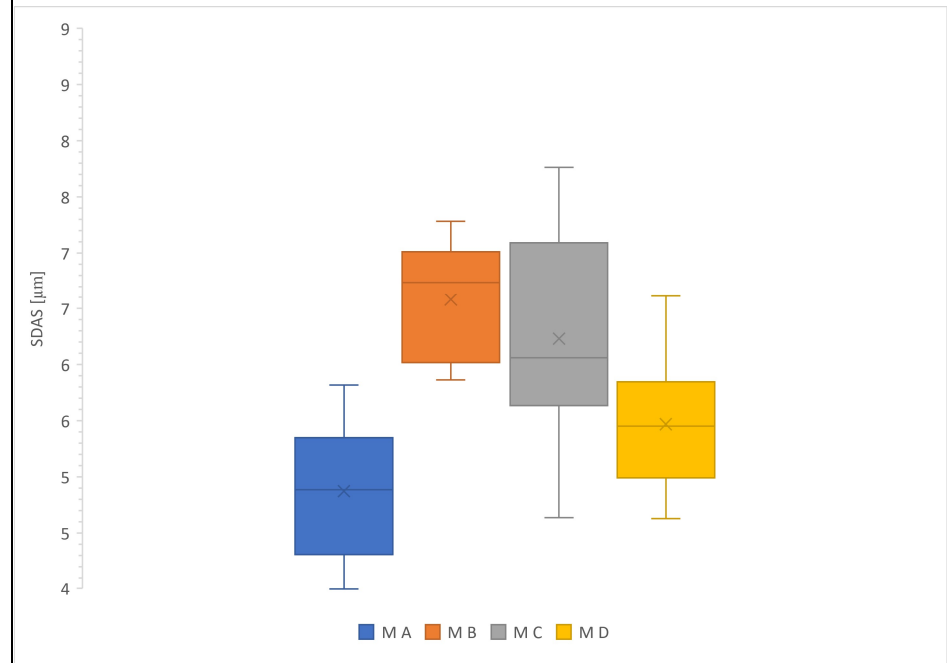
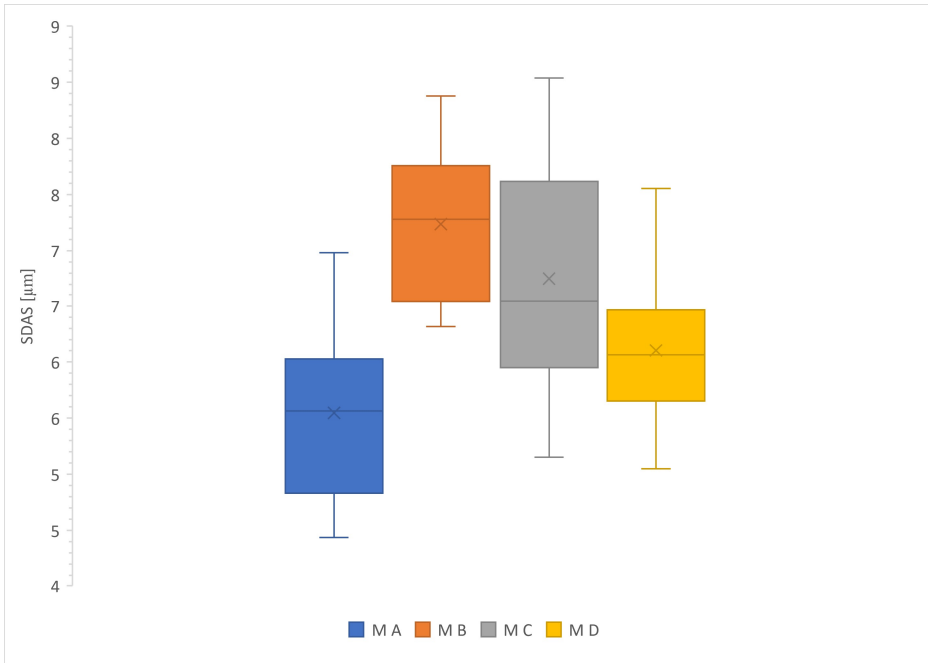
Specimens	E [Gpa]	E STD	$\sigma_y$ Av.	$\sigma_y$ STD	$\sigma_{TS}$ Av.	$\sigma_{TS}$ STD	%El Av.	%EL STD
Y1-Y5	68.3	5.6	136.9	2.9	233.8	5.1	8.88	0.62
X1-X6	70.2	5.5	132.3	1.8	226.7	5.5	11.25	0.87
Z1-Z6	69.6	8.1	136.4	5.0	229.4	6.1	9.23	1.01

# SDAS Measurement Data WAAM specimen M

18.12.2019 Annbjørg Horgar

Equation L/(N-1)			
MA	MB	MC	MD
5.7	7.2	6.3	6.1
4.9	8.1	7.4	7.6
4.6	6.4	6.1	6.8
4.4	7.5	5.5	6.2
5.3	6.3	8.5	6.3
6.0	6.6	8.2	5.0
5.9	8.4	6.4	6.0
7.0	7.4	6.6	5.9
6.1	7.6	7.2	5.8
5.4	6.9	5.2	5.3

Equation L/N			
MA	MB	MC	MD
5.3	6.7	5.9	5.4
4.4	7.3	6.9	6.6
4.2	6.0	5.8	6.3
4.0	7.0	5.0	5.6
4.8	5.9	7.8	5.7
5.4	6.2	7.7	4.6
5.0	7.2	5.9	5.5
5.8	6.8	6.2	5.1
5.1	6.9	6.5	5.0
4.8	6.0	4.6	4.8

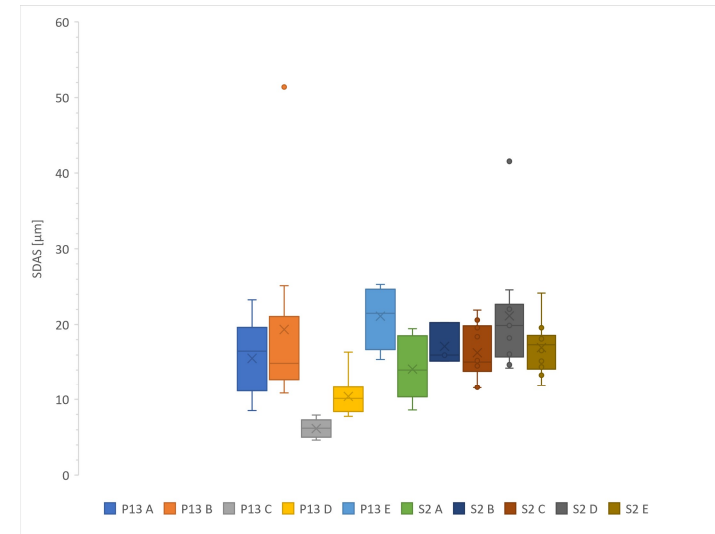
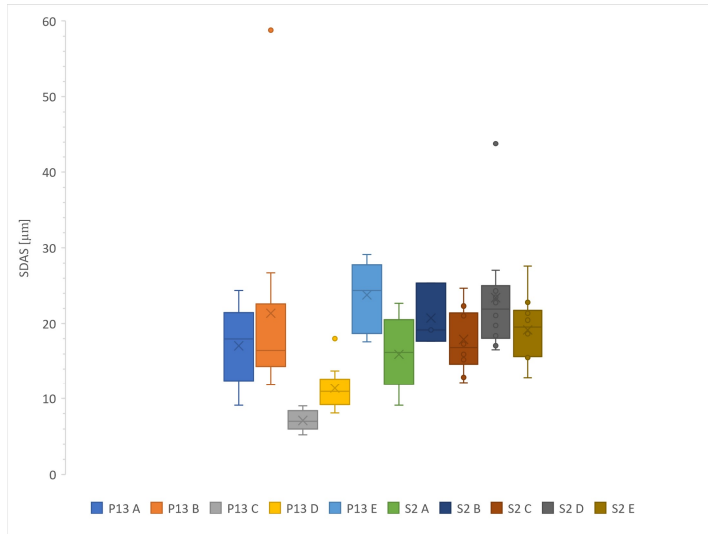


# SDAS Measurement Data Casting P13 and S2

18.12.2019 Annbjørg Hørgar

P13 A	P13 B	P13 C	P13 D	Equation L/(N-1)		S2 B	S2 C	S2 D	S2 E
				P13 E	S2 A				
17.9	58.8	6.4	9.5	22.7	16.4	17.7	21.1	21.1	15.7
9.1	21.2	5.2	8.4	23.1	16.1	25.3	15.9	23.5	16.0
22.0	17.6	9.1	9.7	17.6	9.1	19.2	15.2	43.8	12.9
21.1	14.5	7.6	12.1	18.7	22.7		12.9	18.4	18.7
18.0	15.0	5.5	11.6	26.5	20.3		21.0	17.1	21.4
10.6	13.7	8.3	13.7	27.6	21.1		24.7	27.1	27.6
24.4	26.7	8.7	8.1	29.1	14.7		17.3	24.3	22.8
13.2	15.4	6.1	10.3	18.7	9.5		22.3	16.5	20.7
21.3	19.1	7.8	18.0	28.1	12.7		12.2	22.8	15.5
13.0	11.8	6.3	12.3	25.7	16.7		16.4	19.8	20.5

P13 A	P13 B	P13 C	P13 D	Equation L/N		S2 B	S2 C	S2 D	S2 E
				P13 E	S2 A				
17.0	51.4	5.8	8.6	20.4	13.6	15.2	19.6	19.9	15.2
8.5	19.7	4.6	7.8	20.5	15.0	20.3	15.2	22.0	14.4
19.6	15.6	7.9	8.6	15.4	8.6	16.0	14.6	41.6	11.9
18.4	12.9	6.7	10.6	16.8	19.4		11.6	16.1	16.6
16.0	14.1	5.0	10.4	24.3	18.5		18.4	14.2	19.6
9.1	12.2	7.4	12.4	24.5	18.8		21.9	24.6	24.1
23.3	25.1	7.3	7.9	25.0	13.3		14.8	20.3	18.2
11.9	13.4	4.9	9.8	16.3	8.8		20.6	14.7	18.1
19.7	18.2	6.5	16.4	25.3	10.9		11.6	19.9	13.3
11.8	10.8	5.3	11.5	22.5	14.4		14.6	18.2	18.2

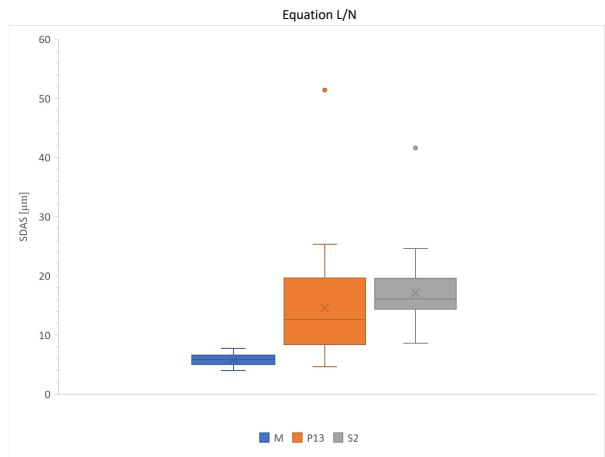
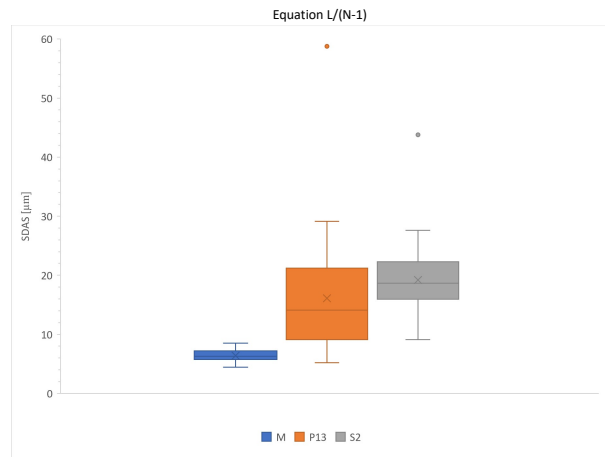




Collected SDAS Measurement Data for WAAM M and Castings P13 and S2

18.12.2019 Annbjørg Hørgor  
LOM images

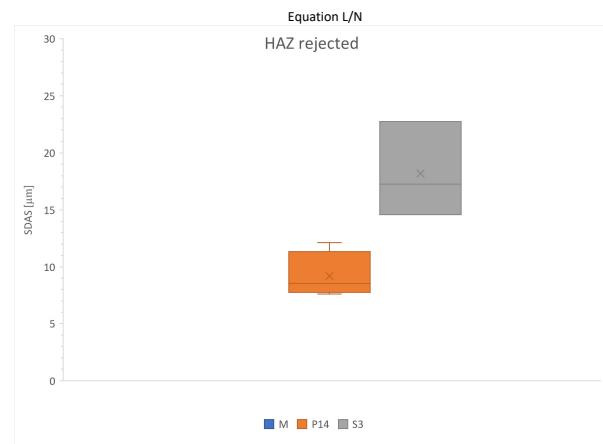
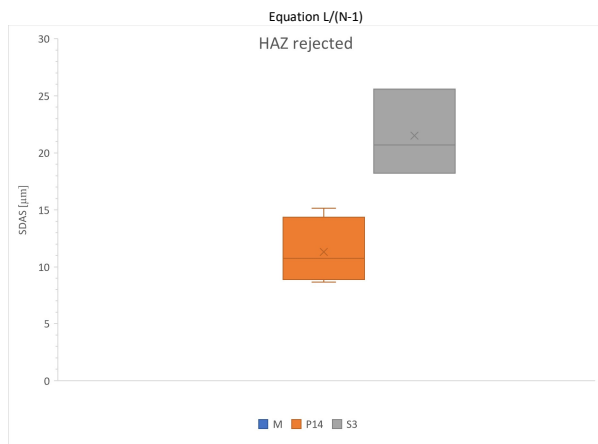
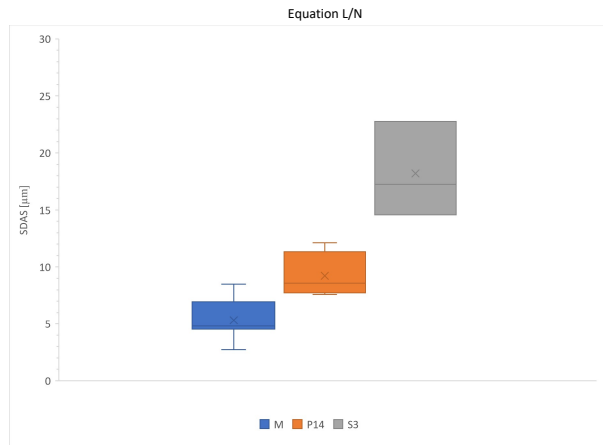
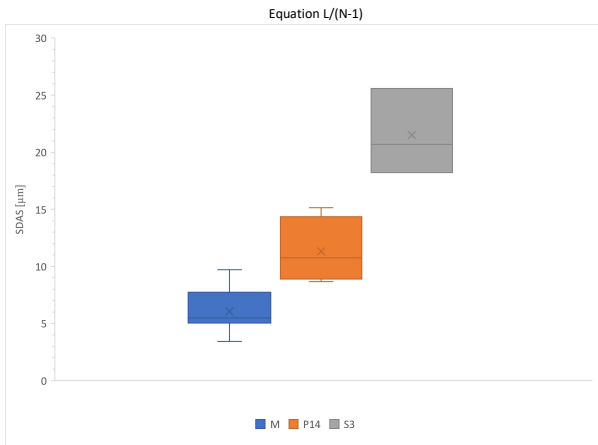
	Equation L/(N-1)			Equation L/N		
	M	P13	S2	M	P13	S2
Max.	8.54	58.77	43.79	7.76	51.43	41.60
Min.	4.44	5.20	9.11	3.99	4.63	8.60
Average	6.41	16.14	19.22	5.79	14.51	17.13
STD	1.02	9.10	5.75	0.95	8.10	5.29
	<b>M</b>	<b>P13</b>	<b>S2</b>	<b>M</b>	<b>P13</b>	<b>S2</b>
	5.7	17.9	16.4	5.3	17.0	13.6
	4.9	9.1	16.1	4.4	8.5	15.0
	4.6	22.0	9.1	4.2	19.6	8.6
	4.4	21.1	22.7	4.0	18.4	19.4
	5.3	18.0	20.3	4.8	16.0	18.5
	6.0	10.6	21.1	5.4	9.1	18.8
	5.9	24.4	14.7	5.0	23.3	13.3
	7.0	13.2	9.5	5.8	11.9	8.8
	6.1	21.3	12.7	5.1	19.7	10.9
	5.4	13.0	16.7	4.8	11.8	14.4
	7.2	58.8	17.7	6.7	51.4	15.2
	8.1	21.2	25.3	7.3	19.7	20.3
	6.4	17.6	19.2	6.0	15.6	16.0
	7.5	14.5	21.1	7.0	12.9	19.6
	6.3	15.0	15.9	5.9	14.1	15.2
	6.6	13.7	15.2	6.2	12.2	14.6
	8.4	26.7	12.9	7.2	25.1	11.6
	7.4	15.4	21.0	6.8	13.4	18.4
	7.6	19.1	24.7	6.9	18.2	21.9
	6.9	11.8	17.3	6.0	10.8	14.8
	6.3	6.4	22.3	5.9	5.8	20.6
	7.4	5.2	12.2	6.9	4.6	11.6
	6.1	9.1	16.4	5.8	7.9	14.6
	5.5	7.6	21.1	5.0	6.7	19.9
	8.5	5.5	23.5	7.8	5.0	22.0
	8.2	8.3	43.8	7.7	7.4	41.6
	6.4	8.7	18.4	5.9	7.3	16.1
	6.6	6.1	17.1	6.2	4.9	14.2
	7.2	7.8	27.1	6.5	6.5	24.6
	5.2	6.3	24.3	4.6	5.3	20.3
	6.1	9.5	16.5	5.4	8.6	14.7
	7.6	8.4	22.8	6.6	7.8	19.9
	6.8	9.7	19.8	6.3	8.6	18.2
	6.2	12.1	15.7	5.6	10.6	15.2
	6.3	11.6	16.0	5.7	10.4	14.4
	5.0	13.7	12.9	4.6	12.4	11.9
	6.0	8.1	18.7	5.5	7.9	16.6
	5.9	10.3	21.4	5.1	9.8	19.6
	5.8	18.0	27.6	5.0	16.4	24.1
	5.3	12.3	22.8	4.8	11.5	18.2
	22.7	20.7	20.4	20.4	18.1	18.1
	23.1	15.5	20.5	20.5	13.3	13.3
	17.6	20.5	15.4	15.4	18.2	18.2
	18.7		16.8	16.8		
	26.5		24.3	24.3		
	27.6		24.5	24.5		
	29.1		25.0	25.0		
	18.7		16.3	16.3		
	28.1		25.3	25.3		
	25.7		22.5	22.5		



Collected SDAS Measurement Data for WAAM M and Castings P13 and S2

18.12.2019 Annbjørg Hørgor  
SEM images

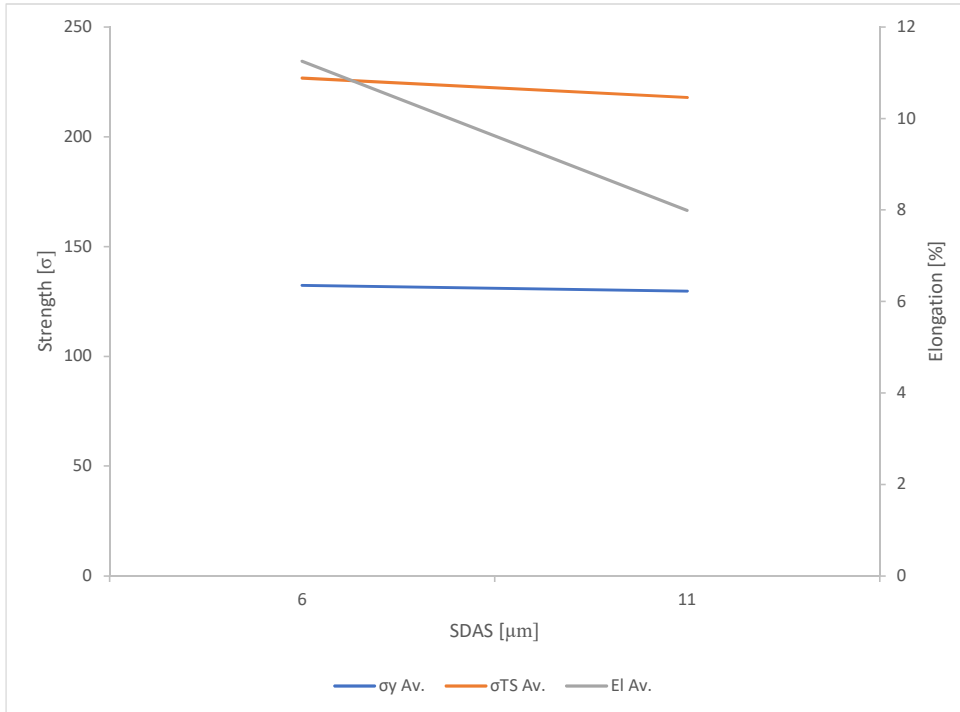
	M	L/(N-1) P14	S3	M	L/N P14	S3
Max.	9.71	15.15	25.60	8.50	12.12	22.75
Min.	3.42	8.67	18.22	2.74	7.59	14.58
Average	6.05	11.33	21.50	5.31	9.21	18.19
STD	1.90	2.51	3.07	1.73	1.75	3.41
SDAS	M	P14	S3	M	P14	S3
	5.5	12.0	25.6	4.8	9.0	22.8
	5.7	15.2	20.7	4.8	12.1	17.2
	5.2	8.7	18.2	4.5	7.6	14.6
	5.5	9.5		5.0	8.2	
	3.4			2.7		
	8.4			7.6		
	5.0			4.6		
	9.7			8.5		



# Relationship between WAAM and Casting

18.12.2018 Annbjørg Horgar

Specimens	E Av.	E STD	$\sigma_y$ Av.	$\sigma_y$ STD	$\sigma_{TS}$ Av.	$\sigma_{TS}$ STD	EI Av.	EI STD	SDAS
WAAM X1-X6	68.3	5.6	132	1.8	227	5.5	11	0.87	6
Casting P6-P11	59.3	8.7	130	3.4	218	4.2	8	1.95	11



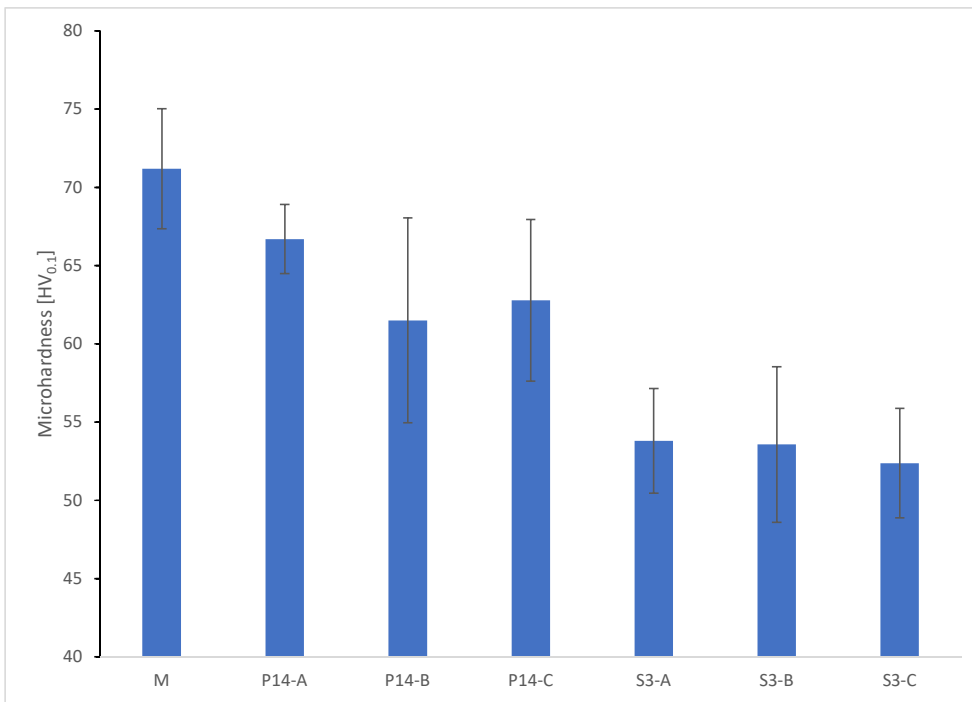


# Summary of Microhardness Measurement Data in WAAM specimen M and Castings P14 and S3 and the Relationship

18.12.2019 Annbjørg Horgar

	WAAM	Permant mold castings			Sand mold castings		
	M	P14-A	P14-B	P14-C	S3-A	S3-B	S3-C
Average	71.2	66.7	61.5	62.8	53.8	53.6	52.4
STD	3.841	2.208	6.548	5.164	3.347	4.978	3.498
Maximum	80.9	73.0	76.0	74.0	59.0	64.0	60.0
Minimum	61.0	63.0	50.0	54.0	48.0	42.0	44.0
SDAS	6		11			21	

Microhardness



Relationship between Microhardness and SDAS

